UNIVERSITY OF CALIFORNIA

Santa Barbara

Scalable Nanopatterning to Engineer Light-Matter Interactions and Strain in III-Nitride Light Emitting Materials

A dissertation submitted in partial satisfaction of the

requirements for the degree Doctor of Philosophy

in Chemical Engineering

by

Lesley W.Y. Chan

Committee in charge:

Professor Michael J. Gordon, Chair

Professor Steven P. DenBaars

Professor Daniel E. Morse

Professor Todd M. Squires

Professor Matthew E. Helgeson

June 2020

The dissertation of Lesley W.Y. Chan is approved.

_____

Daniel E. Morse

_____

Steven P. DenBaars

_____

Todd M. Squires

_____

Matthew E. Helgeson

_____

Michael J. Gordon, Committee Chair

March 2020

Scalable Nanopatterning to Engineer Light-Matter Interactions and Strain in III-Nitride Light Emitting Materials

by

Lesley W.Y. Chan

To my parents, Ming and Vicki.

Acknowledgements

My career at UCSB actually started before grad school, during a research internship in the summer of 2014. I worked in Mike Gordon's group, my mentor was Federico Lora Gonzalez, and we worked closely with Dan Morse. I learned so much that summer, and I will always be grateful for the mentorship I received from the three of them. It was this experience that solidified my decision to pursue a Ph.D., and I am immensely lucky that Mike welcomed me back into his lab as a graduate student. Mike is the most supportive advisor and a remarkable scientist, and I will always be grateful for everything he taught me. Mike, thank you for believing in me. I can safely say that I would not be where I am today without you. I would also like to thank my committee members for their guidance throughout my time at UCSB, namely, Dan Morse (of course), Steve DenBaars, Matt Helgeson, and Todd Squires.

Joining the Gordon group was one of the better decisions I made in grad school. I am grateful for Katie Mackie, Rich Hermann, Alex Heilman, Louis Jones, and Andrew Pebley, who welcomed me into the group when I first started. Pavel Shapturenka, Sheng-Ping Liang, and Ryan Ley were monumental in my growth as a scientist, and working closely with them was an invaluable experience. I will always look back fondly on Gordon group Mammoth trips, office shenanigans, and nights downtown. Our group definitely had the most fun. I would also like to acknowledge the awesome undergraduates and interns who I had the pleasure of working with

throughout these years, specifically Oscar Wu, Alex Berry, Aaron Chan, and Therese Karmstrand.

SSLEEC and the nitrides community provided me with many resources and opportunities. I would like to thank Tal Margalith for his mentorship, both in research meetings and with career advice, and the microLED team.

Perhaps the highlight of grad school was all of the friends (both people and dogs) who have impacted me. I would like to acknowledge friends in my cohort, specifically, Patrick Corona (and Harshita Polishetty), Julia Fisher, Alex Zhang, Mike Burroughs, and Chithra Asokan. Thanks for dragging me through our first year classes. I am also grateful for the dinner crew – Elizabeth Hiroyasu, Justin Yoo, Chris Uraine, Rachel Torres, and Momo – for our epic feasts every week. I am also extremely grateful for Cheyenne Lynsky, Simone Tommaso Suran Brunelli, Elayne Thomas, Brian Markman, Monica Volk, David Hwang, and Erik Dayvie, for our many camping trips and Modern Times hangouts.

Chris Pynn gets his own section because not only is he one of my best friends, but he is also an amazing mentor. Thanks for teaching me almost everything I know about LEDs and being there when I needed help figuring out life.

Grad school would have been exponentially more difficult without the loving support of my friends back home. I would like to thank Johnny Jung, Sarah Kang, Alaric Qin, Paulina Rue, Alex Mao, Kevin Andres, Sarah Tran, Ryan Su, Jasper Wu, Karina Hwang, Heesoo Kim, Hana Jang, Christine Lee, Jade Macabulos, and Dorothy

Le. You all gave me so many things to look forward to after busy weeks in lab, from catch-up phone calls, travelling together, weekend visits in Santa Barbara, or just meeting up back home.

I am extremely grateful for my family, who have given me everything. I would like to especially thank my brother, my favorite person in the whole world. Thank you for always being there.

Finally, I would like to thank my boyfriend, Tuan Nguyen. I have been so lucky to have him by side throughout this five year journey. Tuan is the most supportive and patient partner, and I am so grateful for his never-ending love and encouragement. You have helped me become a better scientist and an overall better person, and there is no one else in the world I would rather have conquered grad school with.

Curriculum Vitæ

Lesley W.Y. Chan

EDUCATION

University of California – Santa Barbara, Santa Barbara, CA March 2020
Ph.D., Chemical Engineering, NSF Graduate Fellow

University of Southern California, Los Angeles, CA May 2015
B.S., Chemical Engineering

PUBLICATIONS

L. Chan, P. Shapturenka, C.D. Pynn, T. Margalith, S.P. DenBaars, M.J. Gordon, "Lift-off of semipolar blue and green III-nitride LEDs grown on free-standing GaN," Submitted.

L. Chan, T. Karmstrand, P. Shapturenka, A. Chan, D. Hwang, T. Margalith, S.P. DenBaars, M.J. Gordon, "Scalable fabrication and chemical lift-off of III-nitride nanoLEDs," In Preparation.

R. Ley, **L. Chan**, P. Shapturenka, M. Wong, S.P. DenBaars, M.J. Gordon, "Strain relaxation of InGaN/GaN multi-quantum well light emitters via nanopatterning," *Opt. Express.* **27**, 30081 (2019).

L. Chan, D.E. Morse, M.J. Gordon, "Moth eye-inspired anti-reflective surfaces for improved IR optical systems and visible LEDs," *Bioinspir. Biomim.* **13**, 041001 (2018). (Invited Review)

L. Chan, Decuir Jr., E.A., Fu, R., Morse, D.E., and Gordon, M.J., "Biomimetic nanostructures in ZnS and ZnSe provide broadband anti-reflectivity", *J. Opt*. **19**, 114007 (2017). (Invited Article)

C.D. Pynn, **L. Chan**, F. Lora Gonzalez, A. Berry, D. Hwang, H. Wu, T. Margalith, D.E. Morse, S.P. DenBaars, and M.J. Gordon, "Enhanced light extraction from free-standing InGaN/GaN light emitters using bio-inspired backside surface structuring," *Opt. Express*. **27**, 15778 (2017).

L. Chan, A. Ghoshal, E.A. DeCuir Jr., Y.P. Chen, D.E. Morse, M.J. Gordon, "Fabrication and optical behavior of graded-index, moth-eye antireflective structures in CdTe*," J. Vac. Sci. Technol. B* **35**, 011201 (2017).

F. Lora Gonzalez, **L. Chan**, A. Berry, D.E. Morse, M.J. Gordon, "A simple colloidal lithography method to fabricate large-area moth-eye anti-reflective structures on Si, Ge, and GaAs for IR applications," *J. Vac. Sci. Technol. B.* **32**, 051213 (2014).

L. Chan, S.M. Lee, D.S. Kang, W. Li, H. Hunter, J.S. Yoon, "Broadband antireflection and absorption enhancement of ultrathin silicon solar microcells enabled with density-graded surface nanostructures," *Appl. Phys. Lett*. **104**, 223905 (2014).

S.M. Lee, R. Biswas, W. Li, D.S. Kang, **L. Chan**, J.S. Yoon, "Printable nanostructured silicon solar cells for high performance, large area flexible photovoltaics." *ACS Nano* **8**, 10507–10516 (2014).

PATENTS

T. Margalith, M. Wong, L. **Chan,** S.P. DenBaars, Patent Pending, UC Case No. 2019-393-2, "Micro-LEDs with ultra-low leakage current."

L. Chan, C.D. Pynn, D. Hwang, P. Shapturenka, M.J. Gordon, S.P. DenBaars, and T. Margalith, US Provisional Patent, filed Nov. 7th, 2018, UC Case No. 2019-391, "Method to create and release nanoscale light emitting diodes from their growth substrates."

L. Chan, T. Karmstrand, D. Hwang, P. Shapturenka, M.J. Gordon, S.P. DenBaars7, and Margalith, T., US Provisional Patent, filed Nov. 7th, 2018, UC Case No. 2019-392, "Control of photoelectrochemical etch parameters for minimization of interfacial roughness of III-nitride LEDs and other light emitting device structures."

CONFERENCES

L. Chan, C.D. Pynn, P. Shapturenka, T. Margalith, S.P. DenBaars, M.J. Gordon, "Solution Processable RGB III-Nitride Light Emitters Enabled by Large Area Photoelectrochemical Lift-Off and Colloidal Lithography," presented at the 13th International Conference on Nitride Semiconductors, Jul. 2019.

L. Chan, C.D. Pynn, P. Shapturenka, T. Margalith, S.P. DenBaars, M.J. Gordon, "Fabrication, Chemical Lift-Off and Optical Characterization of Nanoscale III-Nitride Light Emitters," presented at the American Vacuum Society – 65th Annual International Symposium, Oct. 2018.

Abstract

Scalable Nanopatterning to Engineer Light-Matter Interactions and Strain in III-Nitride Light Emitting Materials

by

Lesley W.Y. Chan

This dissertation work focuses on the development and application of a tunable, scalable, and robust patterning methodology, based on colloidal lithography and plasma etching, to create graded-index, moth eye (ME)-like surface features and nanostructures to control reflection at IR and III-nitride material interfaces and realize novel, nanoscale light emitters. Silica colloidal mask particles were deposited on various substrates using Langmuir-Blodgett dip coating, followed by mask reduction, and mask pattern transfer into the underlying substrate using a combination of plasma and/or wet-chemical etching techniques. The resulting ME patterned surfaces and nanostructures were characterized and simulated using various experimental (SEM, AFM, photo/cathode/electro-luminescence, FTIR) and theoretical methods (finite difference time domain (FDTD) and Monte Carlo-based ray tracing), respectively, as well as incorporated into simple photonic and luminescent devices.

Hexagonal arrays of nanoscale moth eye features, i.e., conical frusta with tunable size, pitch, and shape, were realized in IR optical materials (CdTe, ZnS, and ZnSe) by isotropic etching of various size silica colloid masks before pattern transfer into the underlying substrate. Large single-side transmission enhancements (9-15% on CdTe thin films and 18% on bulk CdTe) were obtained over the short, mid, and far IR wavelength ranges (λ = 6-20 μm) by simply adjusting colloidal mask size (310-2530 nm). Substantial increases in broadband transmission were also achieved for ZnS and ZnSe across the 2–20 μm range (23% and 26% single-side transmission improvement and 92% and 88% absolute double-side transmission, respectively), in excellent agreement with FDTD optical simulations.

Moth eye surface structures were also implemented on the light outcoupling surface of GaN/InGaN light emitters to enhance light extraction efficiency. Features with aspect ratios of 3:1 were produced using silica masks (d = 170–2530 nm) and Cl_2/N_2-based plasma etching on devices grown on semipolar GaN substrates. InGaN/GaN MQW structures were optically pumped at 266 nm and light extraction enhancement was quantified using angle-resolved photoluminescence. A 4.8-fold overall enhancement in light extraction (9-fold at normal incidence) relative to a flat device was achieved using a feature pitch of 2530 nm. FDTD and ray tracing calculations of light extraction enhancement were in excellent agreement with experimentally measured results.

Finally, nanoscale light-emitting diodes (nanoLEDs) with active and sacrificial multi-quantum well (MQW) layers were fabricated and released into solution using a combination of colloidal lithography and photoelectrochemical (PEC) etching of sacrificial MQW layers. Wafer-scale fabrication processes for both c-plane and semipolar nanoLEDs were developed. The PEC etch was optimized to minimize undercut roughness, and thus limit the damage to the active MQW layers. X-ray diffraction was employed to assess strain relaxation due to nanopatterning, which showed ~15% strain relaxation for 500 nm nanoLEDs. Overall, this work shows that colloidal lithography, combined with chemical release, is a viable route to produce solution processable, high efficiency nanoscale light emitters.

Table of Contents

List of Figures

Chapter 2

Chapter 3

Chapter 4

Chapter 5

Chapter 6

Chapter 7

Chapter 8

Chapter 9

Chapter 1

Introduction

1.1 Nanofabrication for applications in optoelectronics

Nanofabrication refers to the practice of nanoscale pattern transfer using a combination of nanoscale lithography and conventional thin film deposition or etch techniques. Over the years, numerous nanopatterning methods have been developed, including electron-beam lithography, interference lithography, extreme ultraviolet lithography, nanoimprint lithography, and colloidal lithography, enabling improvement and development of novel optoelectronics that leverage sub-wavelength nanostructures. Such subwavelength features allow for the control or enhancement of different optical properties. For instance, nanofabrication has enabled a wealth of different forms of periodically patterned surfaces for various optoelectronic device applications, such as diffraction gratings, photonic crystals to enhance light extraction from light-emitting diodes (LEDs)[1–3], anti-reflective nanostructured surfaces[4–8], color filters[9,10], and selective-area growth templates[11–15].

For many of these applications, large areas must be patterned at low cost for commercial feasibility. Furthermore, some applications involve substrates that may be curved or irregular, so the patterning method must be compatible with nonplanar surfaces. As such, it is important to develop and adapt nanopatterning methods that are scalable, reproducible, and easy. Some of the aforementioned nanopatterning methods do not necessarily meet these needs. For example, electron-beam lithography uses an electron beam to create a pattern in a resist layer and is not scalable because it is a serial, direct write method. It is therefore too expensive and time consuming to

be used in large-scale, high-throughput applications. Extreme UV lithography is an optical lithography, but irregularities in surface topography (deviation from planar) lead to poor pattern transfer. The work presented in this thesis is focused on addressing these needs, and is based on the development of a scalable, colloid-based nanopatterning method to enhance light detection and extraction by minimizing reflective losses in venues such as infrared (IR) detectors and visible LEDs, as well as to create novel light emitting devices.

1.2 Thesis scope and project goals

The focus of this dissertation is on the recent development and adaptation of a scalable colloid-based nanopatterning platform for applications in IR anti-reflective surfaces and III-nitride visible LEDs. The work presented in this thesis addresses the following project goals:

- Develop an easy, scalable, defect-tolerant, and substrate-agnostic nanopatterning method that mimics the graded refractive index behavior of the moth eye (ME) to deliver broadband and angle-independent, anti-reflective behavior to surfaces in the λ = 2-50+ μm IR spectral range.
- Understand and predict optical behavior of ME anti-reflective surfaces and their influence on optoelectronic device performance using quantitative comparison of experiment with theoretical calculations based on the transfer matrix method (TMM), finite difference time domain (FDTD), and ray tracing.

- Adapt the colloidal nanofabrication method to III-nitrides to enhance light extraction from LEDs and develop an active nanoscale light-emitter platform (e.g., nanorods embedded with an active multi-quantum well layer), such that devices can be optically pumped in solution or electrically pumped on foreign and/or flexible substrates.

In addressing these goals, this thesis will first discuss the optical physics that govern light-matter interactions with planar and structured surfaces, with feature sizes much smaller than, on the order of, and infinitely large compared to, the wavelength of interest (Chapter 2). Next, a detailed description of the colloidal lithography and plasma etching protocol developed in this work, is presented (Chapter 3). After, experimental and optical simulation results of ME-inspired anti-reflection coatings in IR relevant materials, such as CdTe (Chapter 4), ZnS, and ZnSe (Chapter 5), are discussed in detail, followed by results from adapting the colloidal nanopatterning method to enhance light extraction from III-nitride LEDs, with accompanying mixed-level simulation results (Chapter 6). These simulations combine FDTD methods to calculate electro-magnetic wave propagation through nanostructured surfaces and Monte-Carlo ray tracing techniques to model light propagation in an LED chip, as a means to understand and predict the influence of outcoupling surface structures on overall light extraction enhancement and directionality. Finally, novel LED architectures enabled by the aforementioned nanopatterning approach are presented. Specifically, a nanoscale LED platform, where individual devices are

fabricated, released from rigid growth substrates into solution, and characterized, for devices grown on both c-plane (Chapter 7) and semipolar (Chapter 8) GaN/InGaN, are presented. In closing, the outlook and next directions of the work, will be discussed, including future routes Langmuir-Blodgett assembly of nanoscale LEDs, 2-D strain relaxed growth templates for long-wavelength emission, and flexible, large-area poly(3,4-ethylenedioxythiophene) polystyrene sulfonate (PEDOT:PSS) on Polydimethylsiloxane (PDMS) contacts for nanorod LEDs.

1.3 References

1. Lai, F.-I. & Yang, J.-F. Enhancement of light output power of GaN-based light-emitting diodes with photonic quasi-crystal patterned on p-GaN surface and n-side sidewall roughing. *Nanoscale Res. Lett.* **8**, 244 (2013).

2. Ng, W. N., Leung, C. H., Lai, P. T. & Choi, H. W. Nanostructuring GaN using microsphere lithography. *J. Vac. Sci. Technol. B Microelectron. Nanom. Struct.* **26**, 76–79 (2008).

3. Fu, W. Y., Wong, K. K. Y. & Choi, H. W. Close-packed hemiellipsoid arrays: A photonic band gap structure patterned by nanosphere lithography. *Appl. Phys. Lett.* **95**, (2009).

4. Chattopadhyay, S. *et al.* Anti-reflecting and photonic nanostructures. *Mater. Sci. Eng. R* **69**, 1–35 (2010).

5. Huang, Y.-F. *et al.* Improved broadband and quasi-omnidirectional anti-reflection properties with biomimetic silicon nanostructures. *Nat. Nanotechnol.* **2**, 770–774 (2007).

6. Diedenhofen, S. L. *et al.* Broad-band and omnidirectional antireflection coatings based on semiconductor nanorods. *Adv. Mater.* **21**, 973–978 (2009).

7. Pynn, C. D. *et al.* Enhanced light extraction from free-standing InGaN/GaN light emitters using bio-inspired backside surface structuring. *Opt. Express* **25**, 15778

(2017).

8. Gonzalez, F. L. & Gordon, M. J. Bio-inspired, sub-wavelength surface structures for ultra-broadband, omni-directional anti-reflection in the mid and far IR. *Opt. Express* **22**, 12808 (2014).

9. Song, M. *et al.* Colors with plasmonic nanostructures: A full-spectrum review. *Appl. Phys. Rev.* **6**, (2019).

10. Gildas, F. & Dan, Y. Review of nanostructure color filters. *J. Nanophotonics* **13**, 1 (2019).

11. Hersee, S. D., Sun, X. & Wang, X. The controlled growth of GaN nanowires. *Nano Lett.* **6**, 1808–1811 (2006).

12. Li, S. & Waag, A. GaN based nanorods for solid state lighting. *J. Appl. Phys.* **111**, (2012).

13. Hartmann, J. *et al.* Growth mechanisms of GaN microrods for 3D core-shell LEDs: The influence of silane flow. *Phys. Status Solidi Appl. Mater. Sci.* **212**, 2830–2836 (2015).

14. Yeh, T. W. *et al.* Vertical nonpolar growth templates for light emitting diodes formed with GaN nanosheets. *Appl. Phys. Lett.* **100**, (2012).

15. Yeh, T. W. *et al.* InGaN/GaN multiple quantum wells grown on nonpolar facets of vertical GaN nanorod arrays. *Nano Lett.* **12**, 3257–3262 (2012).

Chapter 2

Physics of optical reflection and bio-inspired antireflective surfaces

Adapted from the *Bioinspiration and Biomimetics* Article:

Chan, L., Morse, D.E., Gordon, M.J. “Moth eye-inspired anti-reflective surfaces for improved IR optical systems and visible LEDs,” *Bioinspir. Biomim.* **13**, 041001 (2018). (Invited Review)

2.1 Introduction: Bio-inspired anti-reflection

A wide variety of remarkable photonic structures has been discovered in nature, providing unique competitive advantages to many species of plants and animals. These evolutionary advancements manifest as bright colors, iridescence, color change, or anti-reflection that aid in communication, crypsis, defense, augmented photosynthesis, and vision[1–8]. For example, male peacocks and many species of butterflies have iridescent and brilliantly colored feathers or wings[9,10], squid and other cephalopods can dynamically tune skin color and reflectivity[11,12], fireflies and many marine organisms emit remarkably bright light[13–16], and several species of moths and butterflies have sub-wavelength, anti-reflective structures on their eyes[17,18] and wings[19,20], providing better night vision and transparency, respectively. All of these organisms have one thing in common: they manipulate light using micro- or nano-scale features or material heterogeneity with critical dimensions that are on the order of, or smaller than, optical wavelengths.

The eye of the moth (Figure 2.1) is covered in hexagonally close-packed, sub-wavelength tissue protuberances that create a structurally-based, graded refractive index (GRIN) profile, rendering the air-eye tissue interface highly transparent (T > 99%). These anti-reflective structures allow the moth to see in low light situations and camouflage itself from predators by reducing glint from the eye. Moth-eye (ME) protuberances are made from chitin and are hypothesized to be created during the larval stage of development through formation and modification of the cuticulin eye

layer[21]. The cuticulin layer is defined as the dense outermost layer of the epicuticle and has been found to cover a majority of the surface of insects. It is formed by secretions during the insect's molting or larval stage and is important because it is involved in the formation of surface patterns.

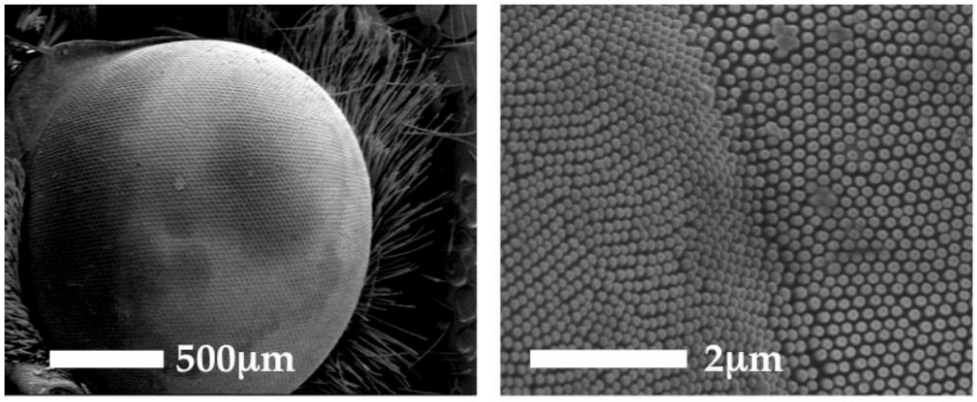

Figure 2.1: SEM images of the eye of the common gray moth (likely *Anavitrinella pampinaria*), showing sub-wavelength tissue protuberances and microscale lens-like structures.

Optoelectronics, photodetectors, light-emitting diodes (LEDs), photovoltaics, etc. can suffer from high optical losses due to reflections that occur at material interfaces where there is large refractive index mismatch, and therefore can benefit from implementation of anti-reflective coatings. Traditional interference-based anti-reflection coatings (ARCs) can help reduce surface reflections at specific wavelengths, but bandwidths and angular response are typically poor[22,23]. Multilayer ARCs help solve these issues, but are expensive to implement, time consuming to manufacture, and substrate dependent[24]. This chapter and those to follow present an alternate approach to reduce surface reflections using ME-inspired nanostructured surfaces

that create a GRIN, making the interface essentially disappear by eliminating Fresnel reflection[25]. Bio-inspired patterning technologies and applications of the ME effect will be demonstrated in various semiconductor platforms to render material interfaces anti-reflective, thus enhancing the performance of optics, detectors and imagers, and solid-state lighting. Discussion topics to follow include an overview of the optical physics of structured interfaces and GRIN materials, with specific application of ME-inspired nanostructures to anti-reflection in the infrared (IR).

2.2 Light-matter interactions: planar surfaces vs. structured surfaces

Electromagnetic (EM) radiation, or light, governed by Maxwell's equations, incident on an interface can undergo various processes where the incoming photons are transmitted, reflected, or absorbed. The reflected (E_R) and transmitted (E_T) electric fields across an unstructured (smooth) interface between materials with complex refractive indices ($\tilde{n}_1$ and $\tilde{n}_2$) are described by the Fresnel relations[26]. The angle and polarization dependent Fresnel equations are:

$$R_{TE} = r_{TE}^2 = \left|\frac{E_r}{E_I}\right|^2 = \left|\frac{\tilde{n}_1 \cos\theta - \tilde{n}_2 cos\theta_t}{\tilde{n}_1 \cos\theta + \tilde{n}_2 cos\theta_t}\right|^2 \quad (2.1)$$

$$R_{TM} = r_{TM}^2 = \left|\frac{E_r}{E_I}\right|^2 = \left|\frac{\tilde{n}_1 \cos\theta_t - \tilde{n}_2 cos\theta}{\tilde{n}_1 \cos\theta_t + \tilde{n}_2 cos\theta}\right|^2 \quad (2.2)$$

$$T_{TE} = t_{TE}^2 = \left|\frac{E_t}{E_I}\right|^2 = \frac{\tilde{n}_2 cos\theta_t}{\tilde{n}_1 \cos\theta}\left|\frac{2\tilde{n}_1 cos\theta}{\tilde{n}_1 \cos\theta + \tilde{n}_2 cos\theta_t}\right|^2 \quad (2.3)$$

$$T_{TM} = t_{TM}^2 = \left|\frac{E_t}{E_I}\right|^2 = \frac{\tilde{n}_2 cos\theta_t}{\tilde{n}_1 \cos\theta}\left|\frac{2\tilde{n}_1 cos\theta}{\tilde{n}_1 \cos\theta_t + \tilde{n}_2 cos\theta}\right|^2 \quad (2.4)$$

where θ is the angle of incidence from normal and θ_t is the transmitted angle. Here, r and t are the Fresnel coefficients and can have complex values. TE and TM describe the transverse electric and transverse magnetic modes, and correspond to S and P polarization, respectively. R and T correspond to the reflection and transmission, respectively. The relationship between incident and transmitted angle, as depicted in Fig. 2.2, is governed by Snell's law:

$$\tilde{n}_1 sin\theta = \tilde{n}_2 sin\theta_t \tag{2.5}$$

In addition to reflection and transmission, these equations predict other interesting optical phenomena such as total internal reflection (TIR), Brewster's effect (polarization-specific reflection), and the Goos-Hänchen shift (spatial displacement of a beam undergoing TIR)[27]. If the change in refractive index $\tilde{n}_1 \rightarrow \tilde{n}_2$ at the interface is abrupt and large, reflection losses can be significant, especially at normal incidence. The overall R and T for a system involving different layers with many, unstructured interfaces, as well as absorption within each layer, and interference can be easily computed using the Fresnel relations and a transfer matrix formalism[26].

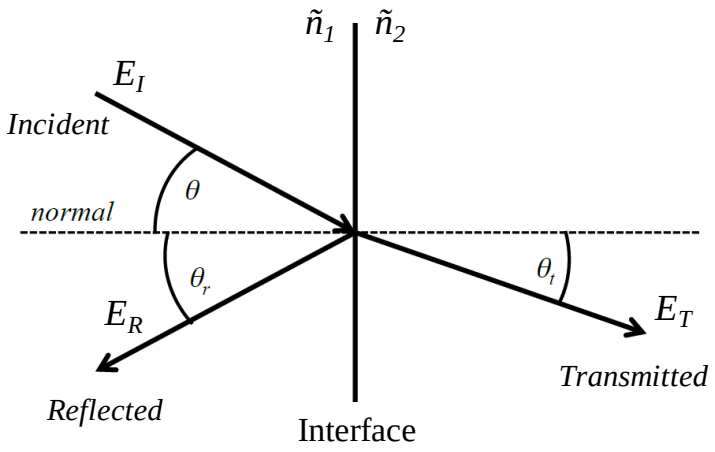

Figure 2.2: Transmission and reflection of electromagnetic waves at a material interface. $\tilde{n}_1$ and $\tilde{n}_2$ are the complex refractive indices of two different materials. θ, θ_r, and θ_t are the incident, reflected, and transmitted angles, respectively. E is the electric field in each region. Reprinted with permission from IOP Publishing.

When surfaces have structure (e.g., roughness, topographic relief, heterogeneity), however, solving Maxwell's equations to predict the behavior of EM fields can be more difficult, especially when surface structures are periodic and/or of the same order of magnitude as the wavelength. Such interactions can be loosely grouped into three regimes, depending on whether the wavelength is essentially infinite, on the order of, or smaller than the characteristic dimension (d) of the interfacial structure, as represented in Figure 2.3. In the ray optics regime ($d >> \lambda$), light matter interactions are well described by the aforementioned Fresnel relations. However, as structure size decreases, interference and diffraction become important for periodic structures, often leading to significant and directional scattering, structural color, iridescence, or photonic crystal behavior[28–30]. Nonzero diffraction orders disappear when $d < \lambda/n_2$ at

normal incidence. In this regime, irregular surface features (roughness) can also lead to diffuse or Lambertian scattering. Finally, when d << λ, periodic structures can be described with effective medium theory, where the structured layer behaves as a homogeneous material with a 'bulk-like' (effective) refractive index that varies with position. ME nanostructures fall into this last regime, presenting a spatially-varying or GRIN interface profile.

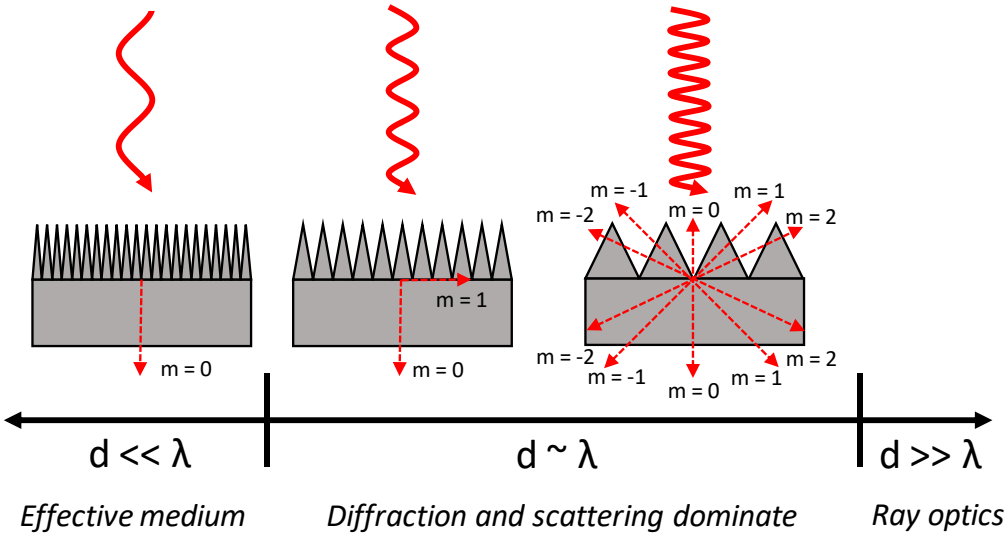

Figure 2.3: Schematic of different optical regimes, depending on whether the wavelength λ is smaller than, on the order of, or essentially infinite compared to some characteristic length scale (d) of the surface structure (feature size, periodicity, etc.). Different diffraction orders are denoted by m. Reprinted with permission from IOP Publishing.

2.3 Conventional vs. moth-eye anti-reflection coatings

Large refractive index mismatches at material interfaces are commonly encountered in many optoelectronic venues (e.g., lens systems, solar cells, LEDs, photodetectors,

imagers), leading to large reflective losses that limit capability, performance, and efficiency (e.g., optical throughput, sensitivity, field of view, wavelength range, power conversion efficiency). The traditional (and commercial) paradigm to mitigate Fresnel losses relies on destructive interference from multiple reflections at interfaces between dissimilar dielectric thin films (typically λ/4 thick), as shown in Figure 2.4(a). These interference-based ARCs are extremely effective in reducing surface reflections at specific wavelengths (e.g., R < 0.01%), but bandwidth and angular response are typically poor[22]. Multilayer ARCs can achieve broadband response and larger acceptance angle, but they are time-consuming to manufacture, expensive, substrate-dependent, and can often delaminate due to thermal expansion differences and heating from standing waves within the coating[23,24]. Finally, interference-based ARCs are very challenging in the IR because there is a limited suite of IR transparent materials useful for coatings, and wavelength ranges are very broad. An idealized multilayer ARC with approximate graded index is also shown in Figure 2.4(b)[31]. While this structure would theoretically result in low reflection, it is extremely difficult to make, as many layers with very specific refractive indices are required.

The moth uses a completely different approach to anti-reflection on its eye surface, namely the GRIN effect (Figure 2.4(c)). The surface of the moth's eye is covered with sub-wavelength, cone-like tissue protuberances that suppress reflection, helping the moth see in low light situations and reduce glare for camouflage against predators[17,18,32,33]. The protuberances introduce a (geometric) graded refractive index

profile from n = 1 (air) to n = 1.4 (eye tissue) that eliminates Fresnel reflection and diffraction (i.e., due to in-plane disorder). Because the refractive index gradient is smooth, Δn between consecutive layers approaches zero, so there is no reflection[25]. Similar nanostructures can be recreated in any material to achieve broadband and omni-directional anti-reflection over an arbitrary wavelength range, so long as the feature is designed appropriately. These ME-inspired arrays have several advantages over traditional ARCs: (i) they are mechanically and thermally robust, since they are part of the substrate; (ii) they are not susceptible to standing wave heating because they are not based on interference; (iii) they create inherently broadband and omni-directional anti-reflectivity; and (iv) they are applicable to any wavelength range, provided the feature geometry is properly designed (i.e., characteristic dimensions << λ).

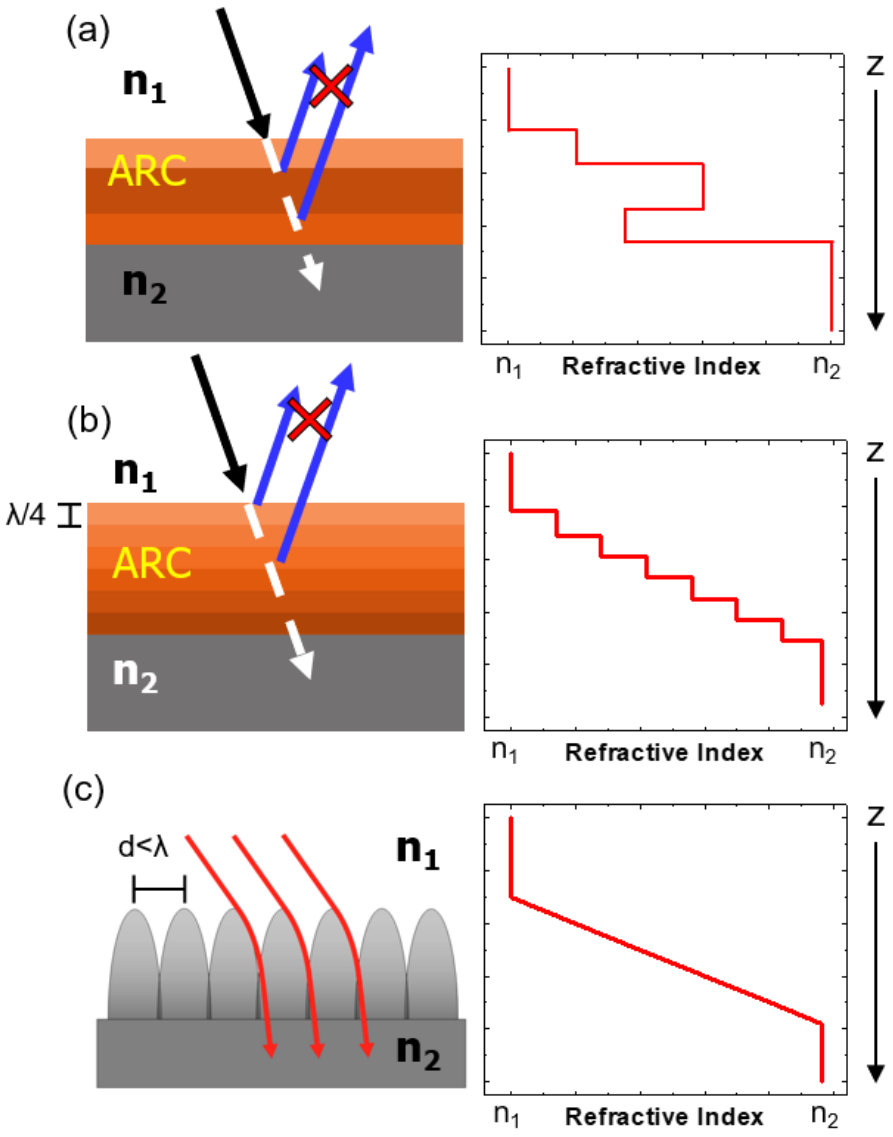

Figure 2.4: (a) Traditional multilayer dielectric thin-film antireflection coating (ARC), (b) idealized multilayer ARC that approximates a graded index, and (c) ME nanostructured surface, along with their qualitative refractive index profiles as a function of depth through the materials. Reprinted with permission from IOP Publishing.

2.4 Optical simulation of nanostructured surfaces

The optical behavior of ME nanostructures can be predicted in the infinite wavelength limit (i.e., ME characteristic dimensions, d << λ) using the transfer matrix method

(TMM) formalism, mentioned previously. The TMM analyzes the propagation of a wave through a stack of thin film layers by self-consistently solving for the transmission (T) and reflection (R) of the wave at every interface using the Fresnel relations; each interface is described by a T/R transfer matrix, which when multiplied by other T/R matrices of the system, yields the overall T and R for the entire stack[34]. One drawback of the TMM, however, is that it does not accurately predict light-matter interactions when $d \sim \lambda$ due to the additional contributions of diffuse scattering and diffraction. For these length scales, rigorous solution of Maxwell's equations must be undertaken with methods such as finite difference time domain (FDTD, e.g., Lumerical[35]) or finite element method (FEM, e.g., COMSOL Multi-Physics[36]) simulations.

FDTD is a rigorous numerical modeling method that solves the time-dependent Maxwell's equations in complex geometries[35,37], and is a powerful tool for predicting optical behavior of structured surfaces. The method involves representing the time-dependent Maxwell's equations as finite difference equations, which are solved on a discrete spatial and temporal grid. Appropriate source, boundary conditions, material parameters (tabulated n and k data), and meshing are selected. The electric and magnetic field vector components are solved within a grid cell (Yee cell[38]), defined by the meshing, at a given instant in time. This process is repeated until the desired electromagnetic field behavior is fully evolved in an established computational domain[37].

While light-matter interactions are perfectly described by Maxwell's equations, there are limitations to the FDTD method because it takes a lot of computational power to accurately predict light propagation through complex geometries. For geometries that span multiple orders of magnitude of length-scales, where structures that are much larger than, on the order of, and/or smaller than the wavelength of light coexist (such as a nanostructured LED), alternative computational methods need to be implemented. In handling light-matter interactions with structures with dimensions that are much larger than the wavelength, geometric optics provides a convenient approximation. Raytracing (e.g. LightTools[39]), a Monte-Carlo based method that uses the Fresnel relations along with Snell's law to describe light interactions where ray optics dominate, can be used to predict light propagation through complex structures.

The general ray tracing calculation approach involves generation of a large number of "rays" at a source, where the wavevector and spectral parameters are defined by the user. Material optical properties, such as the refractive index and absorption coefficient, and geometry are also defined. Each ray of light follows the rules of geometric optics, where the angle and intensity of reflected and transmitted rays obey the Fresnel relations and Snell's law. The simulation ends when all rays are either collected by a receiver or absorbed in the material. In an actual ray tracing calculation, there are many possible variations on how LightTools handles what occurs when a ray hits an interface. For instance, the ray can be split (one ray splits into two rays, where one is reflected and one is transmitted) where the relative

intensities of the reflected and transmitted rays are related to the Fresnel coefficients. Another option could be to not split the ray, but the probability of whether the ray is reflected or transmitted depends on the weight of the Fresnel coefficients. Once each generated ray is absorbed in the material (terminated) or collected by a receiver, the calculation is finished. Quantities of interest, such as light extraction efficiency, can then be calculated by examining where rays terminate, how many are absorbed at each surface, how many are terminated because they fall below a threshold, how many are collected by a receiver, etc. For example, total light extraction efficiency is simply the ratio of the number of rays that propagate out of the model (collected by a far-field receiver) to the total number of rays generated.

2.5 Conventional nanopatterning methods

Researchers have used various methods to pattern ME-inspired nanostructures, such as photo (interference & holographic), e-beam, nanoimprint, and soft lithographies. Electron-beam lithography is a mask-less patterning method that uses an electron beam to directly draw patterns in a stenciling "resist" layer of a polymer mask[40,41]. The solubility of the resist changes with electron beam exposure, enabling selective removal of the resist. E-beam lithography is useful for patterning sub-10 nm features with high image fidelity and reproducibility, but this method is slow and extremely expensive, since it is a serial writing processes, making it unsuitable for high-throughput applications. Interference lithography, which is based on the interference

of laser beams to produce periodic patterns in photoresist, has been used to produce sub-micron features; this method has been shown to pattern large areas, making it scalable for large scale applications[42]. As an example, Hobbs and Macleod have fabricated both hole arrays and ME structuring in a variety of materials such as Si, CdZnTe, ZnS, ZnSe, etc., for applications in the IR using interference-based photolithography and dry etching, as shown in Figure 2.5[43–45]. They demonstrated excellent anti-reflective properties over the short-wave (SWIR) to long-wave (LWIR) IR range. However, second order interference patterns related to reflections and standing waves from reflective substrates are an issue. Also, because pattern geometry (feature size, pitch) and the illuminated area are governed by interference, there is a limited operating window. Nanoimprint lithography, which has potential for high-throughput applications, involves using a nanostructured stamp to mechanically deform a resist layer[46,47]. However, there are problems with mold fabrication and release, originating from high surface area contact with soft stamps. Furthermore, the stamp is produced using a nanostructured master mold, which often relies on interference or electron-beam lithography to make the original pattern. Given the aforementioned issues, an alternative method to create ME-inspired nanostructures that is easy, robust, and scalable is highly desirable. Colloidal lithography with plasma etching solves all of these problems, and will be discussed in detail in the following chapter. In the next section, a thorough demonstration of the method, based on results from literature, will be presented.

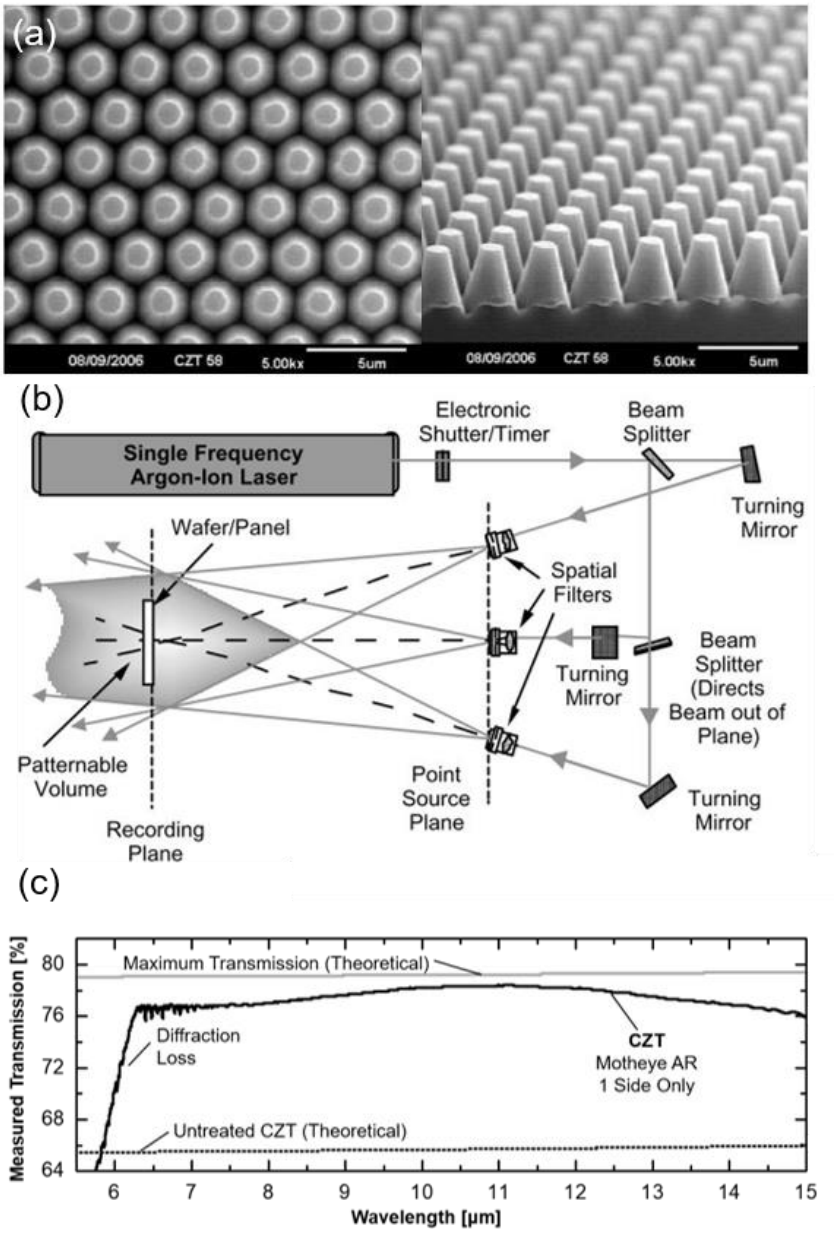

Figure 2.5: (a) SEM images of CdZnTe ME nanostructures fabricated using interference-based photolithography and dry etching. (b) Schematic of multiple-beam interference lithography set-up used in this study. (c) Measured transmission of ME surface on one side of a CdZnTe window compared to theory for an ideal, untreated (flat) CdZnTe substrate and theoretical maximum transmission of single-side ARC. Panels (a) and (c) reprinted from [43] and panel (b) reprinted from [45] with permission from SPIE Publications.

2.6 Demonstration of ME-ARCs in literature

ME nanostructures designed to operate in the visible spectrum have been studied extensively, for applications in solar cells, anti-glare, etc.[48–52]. However, broadband AR surfaces in the IR are critically important - and was previously more difficult to achieve than for applications in the visible - because of the high refractive indices and large bandwidths (microns) involved. For instance, thermal imagers are typically made of high refractive index semiconductors (n > 2.7) such as CdTe or HgCdTe. To minimize reflective losses and improve image fidelity and field of view, ARCs are required at the CdTe-air interface. However, optics used in thermal imaging must be compatible with the full MWIR spectral range (~3-5 μm), so a broadband ARC is necessary. Interference-based coatings cannot satisfy this need due to their narrow bandwidth limitations discussed earlier. ME nanostructures, on the other hand, provide exceptionally broadband anti-reflection, and the size tunability of ME nanostructures fabricated using colloidal lithography and etching makes them excellent for anti-reflection applications in the IR.

ME features for broadband anti-reflection in the SWIR to LWIR were fabricated in a variety of semiconductor materials (Si, Ge, GaAs) by Lora Gonzalez *et al.* using a simple and scalable colloidal lithography and single-step plasma etching platform[53]. In this work, colloid mask sizes of 380 nm and 540 nm were used to fabricate different ME features on both the front and backsides of Si and Ge, resulting in significant peak transmission (T_{max} = 86% vs. 53%, and 91% vs. 45%) enhancement for double-side ME

structured substrates compared to flat surfaces over the λ = 4-20+ μm region, as shown in Figure 2.6. The TMM was used with an effective medium approximation (EMA) to calculate and understand the theoretical behavior of different ME geometries[54,55].

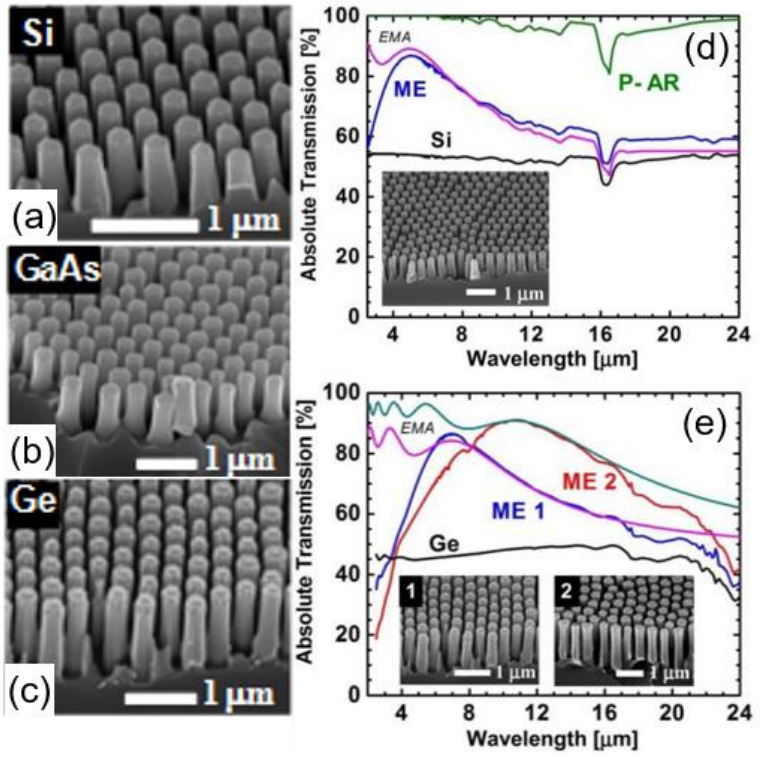

Figure 2.6: (a) SEM images of ME nanostructures fabricated using colloidal lithography and plasma etching on Si, GaAs, and Ge (all substrates were undoped). Double-side (DS) ME structured substrates were fabricated, demonstrating peak absolute transmission of ~86% and up to ~91% for (d) DS-Si and (e) DS-Ge, respectively. Measured transmission spectra for both ME structured materials were in good agreement with effective medium approximation calculations in the infinite wavelength limit[53]. Reprinted from [53], with the permission of the American Vacuum Society.

Kothary *et al.* demonstrated enhanced anti-reflection in the MWIR using Si MEs[56]. Silica microspheres from 100-1000 nm were used as the mask, and coating of 4 in.

wafers was achieved (Figure 2.7(a)), highlighting the scalability of colloidal lithography and plasma etching. A Cl_2-based etch was used for pattern transfer, resulting in ME features with aspect ratios ranging from 3.3-12.9 (Figure 2.7(b)). Peak transmission >90% (Figure 2.7(c)) was obtained for smoothly tapered ME features created with 200-300 nm mask particles. The authors attributed low transmission for 1 μm diameter structures to diffractive loses below $\lambda \sim 4.4$ μm, as predicted from the relationship $d/\lambda < 1/(n_s + n_m)$, where d is the period of the grating, and n_s and n_m are the refractive indices of the substrate and surrounding medium, respectively[57]. Colloidal lithography and dry etching were also used by Xu and coworkers to produce nanostructures in Si for anti-reflection from the visible to SWIR wavelength ranges (Figure 2.7(d-f))[58]. Polystyrene (PS) nanospheres (d = 100 nm, 300 nm, 1.1 μm) were used as a mask with SF_4/CHF_3 dry etching. Structures with a 1.1 μm pitch showed $R < 8\%$ for $\lambda = 900$ to 2400 nm and $R_{min} < 5\%$ at $\lambda \sim 1600$ nm. These authors also found that the low reflection range scaled with structure pitch. For instance, ME structured surfaces with periods of 200 and 300 nm exhibited low reflectance at wavelength ranges that were slightly blue-shifted compared to that for the 1.1 μm period structures.

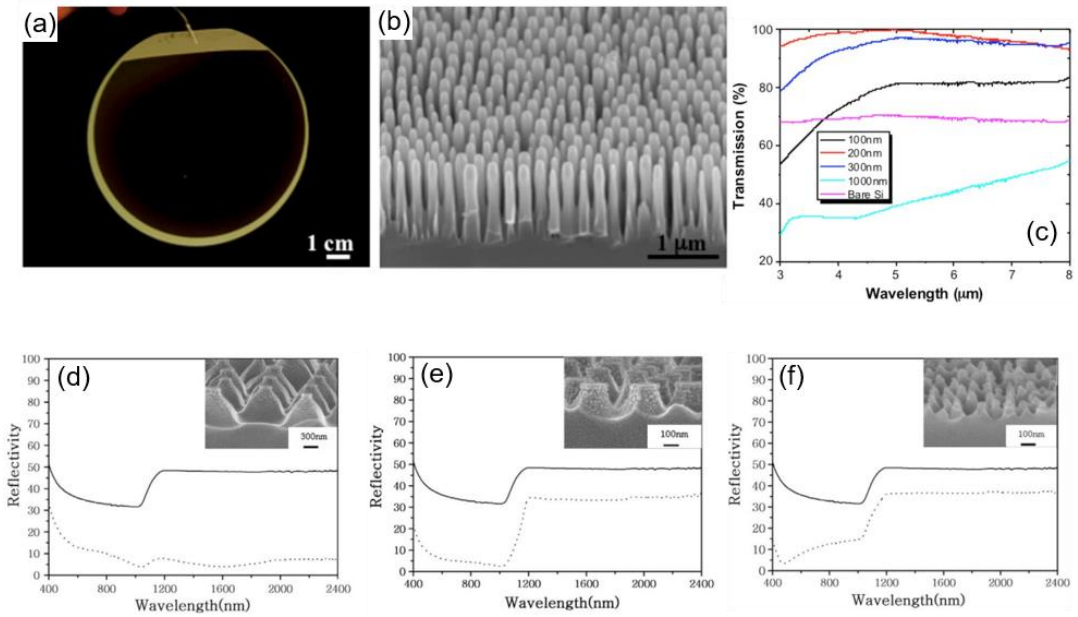

Figure 2.7: ME structured Si surfaces fabricated with colloidal masks and Cl_2-based dry etching. (a) Photograph of 4 in Si wafer after ME structuring using 200 nm colloidal mask. (b) SEM image of ME structuring in (a). (c) Transmission of double-side ME structured wafers fabricated with different diameter silica masks (100-1000 nm) compared to a bare Si sample[56]. (d-f) Reflectivity of nanostructured Si (dotted) fabricated with PS spherical masks with diameters (d) 1.1 μm, (e) 300 nm, and (f) 100 nm, compared to the reflectivity of smooth Si (solid). Insets show SEM images of corresponding ME structures[58]. Panels (a-c) reprinted from [56] with permission from the American Vacuum Society and panels (d-f) reprinted from [58], with permission from Elsevier.

An additional and potentially useful advantage of ME structured AR surfaces is that they often can be superhydrophobic, with the contact angle of water on the surface exceeding 150°. Such surfaces are excellent for applications in self-cleaning ARCs. For instance, Wang *et al.* fabricated ME-structured Si using a two-step colloidal lithograph and plasma etching process to create a corrugated nanocone array, and examined both the visible-to-NIR reflectance and water contact angle (Figure 2.8(a))[59]. Large polystyrene (PS) microspheres (1.1 μm) were first deposited and etched in

$SF_6/CHF_3/O_2$ to form blunt cones, followed by deposition of smaller PS colloids (d = 550 and 220 nm) and a second etch step. Total reflectance of the large nanocone array was <10% over the range of λ = 400-1000 nm, and the smaller secondary structuring resulted in even lower R. The authors fluorinated the ME surfaces with a fluoroalkylsilane, and demonstrated that superhydrophobicity could be obtained, i.e., contact angles for bare Si, a planar nanocone array, and a corrugated nanocone array were 109°, 146°, and 164°, respectively (Figure 2.8(b-d)).

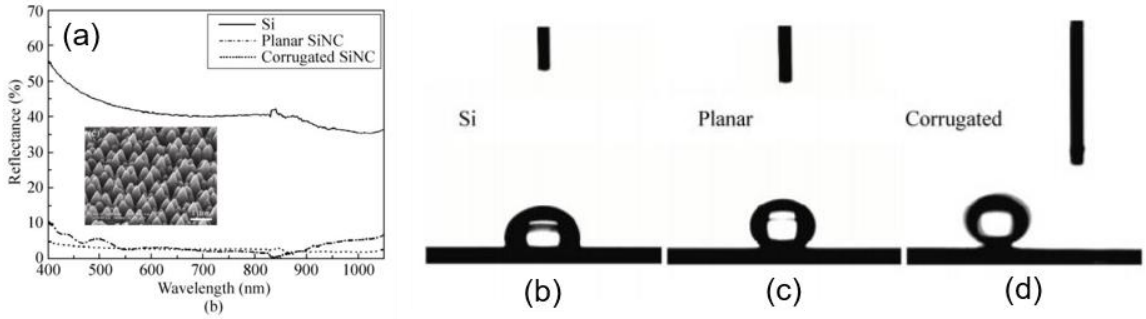

Figure 2.8: (a) Reflectance spectra of bare Si (solid), planar Si nanocones (dash-dot), and corrugated Si nanocones (dash). Contact angle images for fluorinated (b) bare Si, (c) planar Si nanocones, and (d) corrugated Si nanocones[59]. Reprinted from [59] with permission from Springer.

In similar experiments, Ji *et al.* and Li *et al.* etched ME-inspired nanostructures into silica to study how structure geometry affected both optical and self-cleaning properties[60,61]. Both works used PS nanospheres as the etch mask, with and without mask size reduction in an O_2 plasma. In the work by Ji, nanopillar geometry ranging from nanocylinders to nanocones was controlled by adjusting the mask size, plasma chemistry during pattern transfer, and post-cleaning processes (Figure 2.9(a-e)).

Pointed cones and bullet-like structures showed the lowest reflectance in the IR, while truncated cones showed the lowest reflectance in the visible. In general, as feature height increased, both the R_{min} and R_{max} tended to red-shift, and higher aspect ratio structures resulted in lower reflectance, as expected for GRIN features (Figure 2.9(f,g). In contrast, Li controlled nanostructure shape by adjusting the vertical etch time and taking advantage of mask shrinking during pattern transfer (Figure 2.9(h-k)). R and T measurements (Figure 2.9(l,m)) showed that paraboloid-contoured arrays had the best anti-reflective properties ($R < 5\%$) over the λ = 1-2.5 μm range.

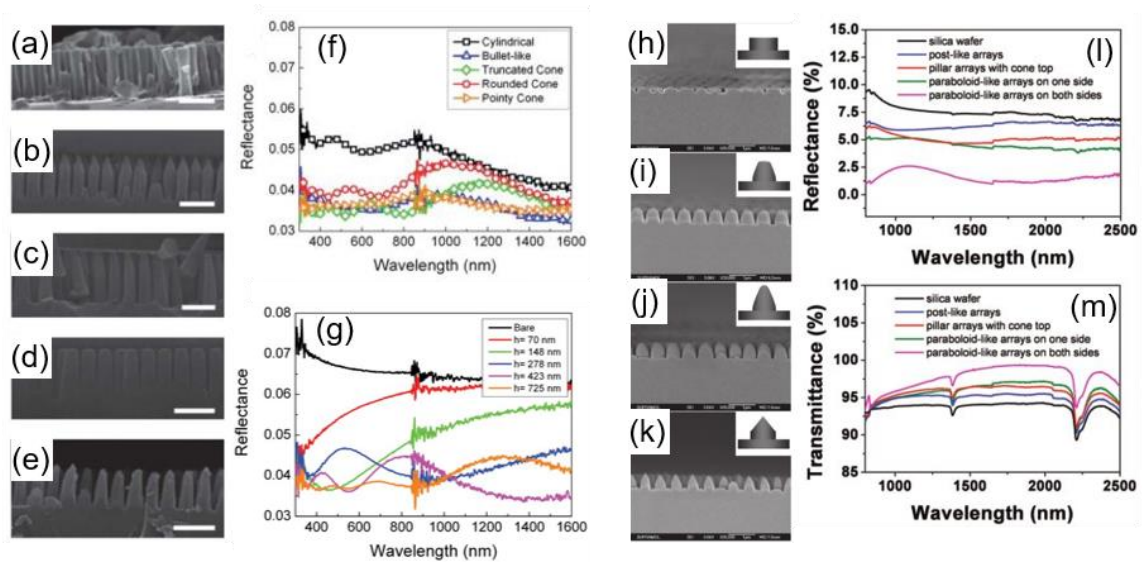

Figure 2.9: (a-e) SEM images of SiO_2 nanostructures fabricated via colloidal lithography with PS colloidal masks, a size reduction etch, vertical etching, and cleaning, resulting in nanostructures with (a) cylindrical, (b) bullet-like, (c) truncated, (d) rounded cone, and (e) pointed cone profiles. (f) Measured shape-dependent reflectance spectra for the various structures in (a-e). (g) Measured reflectance of ME nanostructured substrates with various heights[60]. (h-k) Cross-sectional SEM images of SiO_2 nanostructures and schematic illustrations of the profiles (insets) of (h) post-like, (i) truncated cone-shaped, (j) paraboloid-like, and (k) cone top nanostructures, for which the various profiles resulted from different etch times. (l) Shape-dependent reflectance and (m) transmittance spectra for nanostructured SiO_2 compared to bare SiO_2 wafer[61]. Panels (a-g) reprinted from [60] with permission from the Royal Society of Chemistry and panels (h-m) reprinted from [61] with permission from the American Chemical Society.

The ME applications discussed thus far apply to situations in which light propagates from a low refractive index medium (usually air) into an optical material or device element with higher refractive index (e.g., lens, solar cell, IR detector or imager); in such cases, the ME effect allows more light transmission into the device. However, the ME effect can also be used in 'reverse', for situations when light generated in a high refractive index medium must be extracted into lower refractive

index surroundings - the perfect example being LEDs or solid-state lasers. LEDs can also benefit from ME-inspired nanostructures which can help enhance light extraction and improve external quantum efficiency (EQE, or plug-to-photon efficiency). The large refractive index contrast between a GaN device (n ~2.45) and its surroundings (air or silicone encapsulant) results in a narrow light escape cone, with critical angles from 24° (air) to 38° (silicone) from normal, above which, the majority of light is trapped by TIR[62]. As a result, roughening the air-material interface is necessary for efficient light extraction. Photoelectrochemical (PEC) etching, which produces random, micron-scale hexagonal pyramids[63] on the nitrogen-face of c-plane GaN, has traditionally been used to solve this problem. However, the PEC technique often has poor reproducibility and the corrosive etchant can damage essential device components, such as metal contacts and mounting adhesives. Furthermore, it has only been demonstrated to work on c-plane GaN and does not work on semipolar or nonpolar GaN orientations[64,65], the latter having inherently higher internal quantum efficiency (IQE) and higher emission of polarized light.

Researchers have created bio-mimetic nanostructures on fully packaged GaN/InGaN LEDs for enhanced light extraction, as described in Figure 2.10[66], where a fire fly-like lens structure was created on the encapsulant-air interface. The fabrication process consisted of first performing colloidal lithography with PS spheres as a mask, and dry etching of SiO_2 to act as a mold. Here, the feature width was adjusted using an isotropic O_2 etch to shrink the mask, and the feature height was

adjusted by anisotropically etching into the SiO_2 layer. A 100 μm thick Polydimethylsiloxane (PDMS) layer was spin-coated on the SiO_2 template and cured for high fidelity pattern transfer. The nanostructured PDMS thin film was then bonded to a thicker PDMS backbone and deformed to create a lens-like shape, in which a UV-curable resin was cast and cured, forming the final nanostructured lens. The resulting nanostructured lenses (with feature heights either 80, 100, 120, or 140 nm; all widths = 150 nm; all pitches = 250 nm) were optically characterized in transmission at λ = 488, 560, and 633 nm. Of these, lenses fabricated with 120 nm tall nanostructures had the highest transmission (T = 98.3% at λ = 560 nm) compared to a smooth-surface lens (T = 95.4%). The relatively modest enhancement observed, however, is likely due to the fact that there are still large reflective losses at the LED-encapsulant interface.

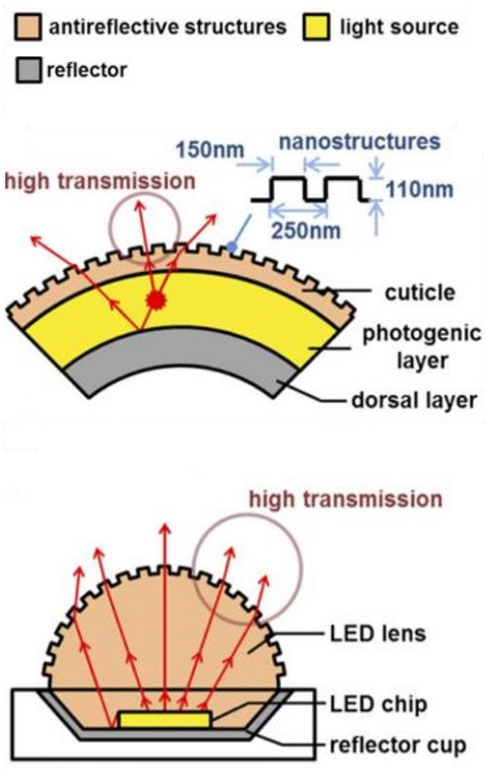

Figure 2.10: Schematic of bioluminescent firefly lantern, comprising a dorsal layer, a photogenic layer where light is generated, and a nanostructured cuticle layer that assists in light extraction (top), and schematic of a firefly-inspired, packaged LED structure comprised of a back-side reflector, the LED chip where light is generated, and a nanostructured encapsulating lens (bottom)[66]. Reprinted from [66] with permission from the National Academy of Sciences.

ME-like features have also been fabricated directly into GaN/InGaN LED structures themselves with colloidal lithography. Ng and coworkers etched nanopillars in the epitaxially-grown device side of a GaN/InGaN LED grown on sapphire using silica colloids (d = 500 nm) as a mask, with BCl_3/Cl_2-based plasma etching (Figure 2.11(a-c))[67]. In this case, the thin p-GaN cap layer was roughened to a depth of only ~250 nm to prevent plasma etch damage to the active multi-quantum well (MQW) region below.

Light extraction enhancement was characterized by measuring MQW photoluminescence (PL); roughened devices showed a 2X increase in emission compared to a flat device, and PL was blue shifted, indicating partial strain relaxation of the InGaN MQWs upon nanopatterning[68]. Photonic bandgap (PBG) structures composed of close-packed hemi-ellipsoid arrays were also created by Fu and coworkers[69]. In this work, 192 nm SiO_2 mask particles were deposited on a GaN device surface and etched using $Cl_2/Ar/CHF_3$. CHF_3 was added to promote simultaneous etching of the silica mask, resulting in lower aspect ratio, more rounded structures. The PL of the PBG structure was 3X greater than for a flat device (Figure 2.11(d)), which the authors attribute to PBG suppression of laterally propagating, guided modes as well as a surface texturing (effective medium) effect. Hsieh *et al.* also demonstrated an electrically pumped device with top-side roughening (~70nm deep into the p-GaN cap) using colloidal lithography and $SiCl_4/Cl_2/Ar$ etching (Figure 2.11(e))[70]. Electroluminescence (EL) at a forward-bias of 20 mA for the structured device was seen to be 37% higher, and blue-shifted, compared to a flat device (Figure 2.11(f)).

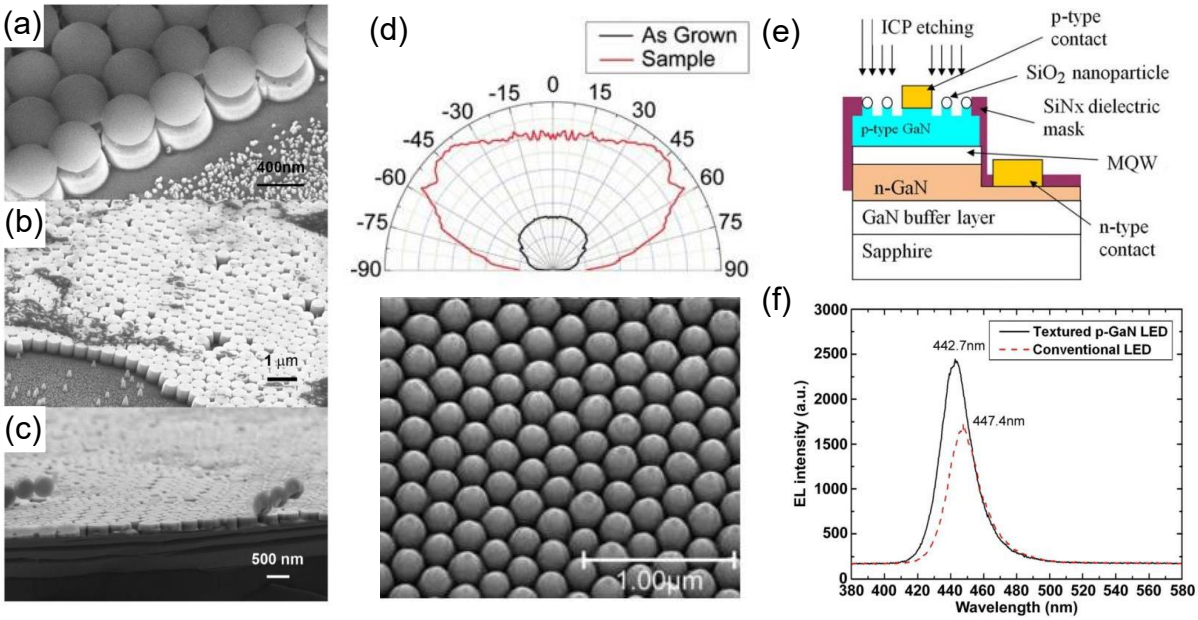

Figure 2.11: (a-c) SEM images of various stages of nanostructure fabrication after (a) plasma etching, (b) mask removal, and (c) cleaning[67]. (d) (top) Angle-resolved photoluminescence of as grown (flat) and hemi-ellipsoid nanostructured devices, and (bottom) top-down SEM image of sample structuring[69]. (e) Schematic of nanosphere lithography implemented in the p-GaN topside of a GaN/InGaN LED grown on sapphire. (f) EL spectra of nanostructured p-GaN LED and conventional flat LED showing increase in intensity and blue-shifted emission for the textured LED[70]. Panels (a-c) reprinted from [67] with permission from the American Vacuum Society, panel (d) reprinted from [69] with permission from the American Institute of Physics, and panels (e,f) reprinted from [70] with permission from IEEE.

While the aforementioned results demonstrate significant enhancement in light extraction efficiency, there are several issues with roughening the topside of electrically pumped devices. First, it is difficult to deposit good metal contacts on nano- or micro-structured surfaces, and current spreading is a problem when p-side contacts are distant from the patterned surface. Etching into or close to MQW regions also introduces non-radiative defects that decrease light output. Finally, to avoid etching into the MQW, the patterning must be very shallow, limiting the aspect ratio and

geometry of ME features, resulting in limited control of light-matter interactions. An alternative approach that incorporates surface roughening on the back-side outcoupling surface in semipolar free-standing GaN/InGaN LEDs, addressing issues in previously discussed nano- and microstructured surfaces for enhancing light extraction from LEDs, is presented in Chapter 6.

2.7 Summary

ME-inspired nanostructures are of particular interest for their ability to suppress reflection, which, when incorporated into critical optical and device interfaces, can minimize reflective losses, increase optical throughput, and increase efficiency and performance. In this chapter, the basic theory of light-matter interactions at different structure lengths scales, depending on whether structure characteristic dimensions are much larger than, on the order of, or much smaller than the wavelengths involved, was reviewed. ME-inspired nanostructures, because of their structurally-based graded refractive index behavior, can be applied to multiple optical situations and material platforms. In particular, ME surfaces can provide broadband anti-reflectivity, large field of view, and different spectral application ranges, through simple tuning of ME feature pitch, aspect ratio, and shape. The few application examples described in this chapter demonstrate that much can be learned from the mechanisms by which biological systems have evolved to manipulate light, and that many optical system and device venues can profit from biomimicry. Exciting new

frontiers include fabrication of nanoscale light emitters, multi-functional surfaces (AR, waveguiding, self-cleaning, etc.), and hybrid biotic/abiotic systems for medical and other technologies. To achieve this, many nanofabrication approaches exist, but a scalable, geometry tunable, reproducible, and easy approach is desired. The following chapter will present a colloid-based nanopatterning method that addresses all the aforementioned concerns.

2.8 References

1. Yu, K., Fan, T., Lou, S. & Zhang, D. Biomimetic optical materials: Integration of nature's design for manipulation of light. *Prog. Mater. Sci.* **58**, 825–873 (2013).

2. Bhushan, B. Biomimetics: lessons from nature–an overview. *Philos. Trans. R. Soc. A* **367**, 1445–1486 (2009).

3. Bar-Cohen, Y. *Biomimetics: Biologically Inspired Technologies*. (CRC Press/Taylor & Francis Group, 2006).

4. Sarikaya, M. Biomimetics: Materials fabrication through biology. *Proc. Natl. Acad. Sci.* **96**, 14183–14185 (1999).

5. Vincent, J. F. V. Biomimetics — a review. *Proc. Inst. Mech. Eng.* **223**, 919–939 (2009).

6. Vincent, J. F. V. Defense and Attack Strategies and Mechanisms in Biology. in *Biomimetics: Biologically Inspired Technologies* 341–363 (CRC Press/Taylor & Francis Group, 2006). doi:10.1201/9781420037715.ch13

7. Cronin, T. W., Johnsen, S., Marshall, N. J. & Warrant, E. J. *Visual Ecology*. (Princeton University Press, 2014). doi:10.1017/CBO9781107415324.004

8. Johnsen, S. *The Optics of Life: a Biologist's Guide to Light in Nature*. (Princeton University Press, 2011).

9. Gorb, S. N. Functional Surfaces in Biology: Mechanisms and Applications. in *Biomimetics: Biologically Inspired Technologies* 381–397 (CRC Press/Taylor & Francis Group, 2006). doi:10.1007/978-1-4020-6695-5

10. Parker, A. R. & Townley, H. E. Biomimetics of photonic nanostructures. *Nat. Nanotechnol.* **2**, 347–353 (2007).

11. Levenson, R., Bracken, C., Bush, N. & Morse, D. E. Cyclable Condensation and Hierarchical Assembly of Metastable Reflectin Proteins, the Drivers of Tunable Biophotonics. *J. Biol. Chem.* **291**, 4058–4068 (2016).

12. DeMartini, D. G., Izumi, M., Weaver, A. T., Pandolfi, E. & Morse, D. E. Structures, Organization, and Function of Reflectin Proteins in Dynamically Tunable Reflective Cells. *J. Biol. Chem.* **290**, 15238–49 (2015).

13. Ghiradella, H. Fine structure of the tracheoles of the lantern of a photurid firefly. *J. Morphol.* **153**, 187–203 (1977).

14. Beams, H. W. & Anderson, E. Light and Electron Microscope Studies on the Light Organ of the Firefly (Photinus pyralis). *Biol. Bull.* **109**, 375–393 (1955).

15. Seliger, H. H. & McElroy, W. D. Spectral emission and quantum yield of firefly bioluminescence. *Arch. Biochem. Biophys.* **88**, 136–141 (1960).

16. Ando, Y. *et al.* Firefly bioluminescence quantum yield and colour change by pH-sensitive green emission. *Nat. Photonics* **2**, 44–47 (2007).

17. Bernhard, C. G. & Miller, W. H. A Corneal Nipple Pattern in Insect Compound Eyes. *Acta Physiol. Scand.* **56**, 385–386 (1962).

18. Stavenga, D. G., Foletti, S., Palasantzas, G. & Arikawa, K. Light on the moth-eye corneal nipple array of butterflies. *Proc. R. Soc. B Biol. Sci.* **273**, 661–667 (2006).

19. Shevtsova, E., Hansson, C., Janzen, D. H. & Kjærandsen, J. Stable structural color patterns displayed on transparent insect wings. *Proc. Natl. Acad. Sci.* **108**, 668–673 (2011).

20. Siddique, R. H., Gomard, G. & Hölscher, H. The role of random nanostructures for the omnidirectional anti-reflection properties of the glasswing butterfly. *Nat. Commun.* **6**, 6909 (2015).

21. Locke, M. The structure and formation of the cuticulin layer in the epicuticle of an insect, Calpodes ethlius (Lepidoptera, Hesperiidae). *J. Morphol.* **118**, 461–494 (1966).

22. Raut, H. K., Ganesh, V. A., Nair, A. S. & Ramakrishna, S. Anti-reflective coatings: A critical, in-depth review. *Energy Environ. Sci.* **4**, 3779–3804 (2011).

23. Kaminski, P. M., Lisco, F. & Walls, J. M. Multilayer Broadband Anti-Reflective

Coatings for Bulk Heterojunction Polymer Solar Cells. *IEEE J. Photovoltaics* **4**, 452–456 (2014).

24. Schubert, M. F. *et al.* Design of multilayer antreflection coatings made from co-sputtered and low-refractive-index materials by genetic algorithm. *Opt. Express* **16**, 5290–5298 (2008).

25. Diedenhofen, S. L. *et al.* Broad-band and omnidirectional antireflection coatings based on semiconductor nanorods. *Adv. Mater.* **21**, 973–978 (2009).

26. Born, M. & Wolf, E. *Principles of optics : electromagnetic theory of propagation, interference and diffraction of light*. (Cambridge University Press, 1999).

27. Lvovsky, A. I. Fresnel Equations. in *Encyclopedia of Optical and Photonic Engineering* (eds. Hoffman, C. & Driggers, R.) 1–6 (CRC Press, 2013). doi:10.1081/E-EOE-120047133

28. Larouche, S. & Smith, D. R. Reconciliation of generalized refraction with diffraction theory. *Opt. Lett.* **37**, 2391–2393 (2012).

29. Moharam, M. G. & Young, L. Criterion for Bragg and Raman-Nath diffraction regimes. *Appl. Opt.* **17**, 1757–1759 (1978).

30. Moharam, M. G., Gaylord, T. K. & Magnusson, R. Criteria for Bragg regime diffraction by phase gratings. *Opt. Commun.* **32**, 14–18 (1980).

31. Dobrowolski, J. A., Poitras, D., Ma, P., Vakil, H. & Acree, M. Toward perfect antireflection coatings: numerical investigation. *Appl. Opt.* **41**, 3075 (2002).

32. Wilson, S. J. & Hutley, M. C. The Optical Properties of 'Moth Eye' Antireflection Surfaces. *Opt. Acta Int. J. Opt.* **29**, 993–1009 (1982).

33. Clapham, P. B. & Hutley, M. C. Reduction of Lens Reflexion by the "Moth Eye" Principle. *Nature* **244**, 281–282 (1973).

34. Katsidis, C. C. & Siapkas, D. I. General transfer-matrix method for optical multilayer systems with coherent, partially coherent, and incoherent interference. *Appl. Opt.* **41**, 3978–3987 (2002).

35. Lumerical Solutions Inc. FDTD Solutions. http://www.lumerical.com/tcad-products/fdtd/ (2017).

36. COMSOL Inc. COMSOL Multiphysics® Modeling Software. https://www.comsol.com/ (2017).

37. Sullivan, D. M. *Electromagnetic Simulation Using the FDTD Method*. (John Wiley & Sons, 2013).

38. Yee, K. S. Numerical Solution of Initial Boundary Value Problems Involving Maxwell's Equations in Isotropic Media. *IEEE Trans. Antennas Propogation* **AP-14**, 302–307 (1966).

39. Synopsis. LightTools. https://www.synopsys.com/optical-solutions/lightto (2020).

40. Tseng, A. A., Chen, K., Chen, C. D. & Ma, K. J. Electron Beam Lithography in Nanoscale Fabrication: Recent Development. *IEEE Trans. Electron. Packag. Manuf.* **26**, 141–149 (2003).

41. Altissimo, M. E-beam lithography for micro-/nanofabrication. *Biomicrofluidics* **4**, 026503 (2010).

42. Lu, C. & Lipson, R. H. Interference lithography: a powerful tool for fabricating periodic structures. *Laser Photon. Rev.* **4**, 568–580 (2009).

43. MacLeod, B. D. & Hobbs, D. S. Long life, high performance anti-reflection treatment for HgCdTe infrared focal plane arrays. in *SPIE Defense and Security Symposium* **6940**, 1–16 (2008).

44. Hobbs, D. S. & MacLeod, B. D. Design, fabrication, and measured performance of anti-reflecting surface textures in infrared transmitting materials. in *Proceedings of SPIE* **5786**, 349–364 (2005).

45. Hobbs, D. S., McLeod, B. D., Kelsey, A. F., Leclerc, M. A. & Sabatino III, E. Automated-interference-lithography-based systems for generation of sub-micron feature size patterns. in *Proceedings Volume 3879, Micromachine Technology for Diffractive and Holographic Optics* **3879**, (1999).

46. Guo, L. J. Nanoimprint Lithography: Methods and Material Requirements. *Adv. Mater.* **19**, 495–513 (2007).

47. Schift, H. Nanoimprint lithography: An old story in modern times? A review. *J. Vac. Sci. Technol. B* **26**, 458–480 (2008).

48. Tan, G. *et al.* Broadband antireflection film with moth-eye-like structure for flexible display applications. *Optica* **4**, 678–683 (2017).

49. Yamada, N., Kim, O. N., Tokimitsu, T., Nakai, Y. & Masuda, H. Optimization of anti-reflection moth-eye structures for use in crystalline silicon solar cells. *Prog. Photovoltaics Res. Appl.* **19**, 134–140 (2011).

50. Boden, S. A. & Bagnall, D. M. Optimization of moth-eye antireflection schemes for silicon solar cells. *Prog. Photovoltaics Res. Appl.* **18**, 195–203 (2010).

51. Forberich, K. *et al.* Performance improvement of organic solar cells with moth eye anti-reflection coating. *Thin Solid Films* **516**, 7167–7170 (2008).

52. Leem, J. W. *et al.* Efficiency Enhancement of Organic Solar Cells Using Hydrophobic Antireflective Inverted Moth-Eye Nanopatterned PDMS Films. *Adv. Energy Mater.* **4**, 1301315 (2014).

53. Lora Gonzalez, F., Chan, L., Berry, A., Morse, D. E. & Gordon, M. J. Simple colloidal lithography method to fabricate large-area moth-eye antireflective structures on Si, Ge, and GaAs for IR applications. *J. Vac. Sci. Technol. B* **32**, 051213 (2014).

54. Bruggeman, D. A. G. Berechnung verschiedener physikalischer Konstanten von heterogenen Substanzen. I. Dielektrizitätskonstanten und Leitfähigkeiten der Mischkörper aus isotropen Substanzen. *Ann. Phys.* **24**, 636–664 (1935).

55. Niklasson, G. A., Granqvist, C. G. & Hunderi, O. Effective medium models for the optical properties of inhomogeneous materials. *Appl. Opt.* **20**, 26–30 (1981).

56. Kothary, P., Phillips, B. M., Leo, S.-Y. & Jiang, P. Bioinspired broadband midwavelength infrared antireflection coatings on silicon. *J. Vac. Sci. Technol. B* **34**, 041807 (2016).

57. Raguin, D. H. & Morris, G. M. Antireflection structured surfaces for the infrared spectral region. *Appl. Opt.* **32**, 1154–1167 (1993).

58. Xu, H. *et al.* Broadband antireflective Si nanopillar arrays produced by nanosphere lithography. *Microelectron. Eng.* **86**, 850–852 (2009).

59. Wang, Y. *et al.* Biomimetic corrugated silicon nanocone arrays for self-cleaning antireflection coatings. *Nano Res.* **3**, 520–527 (2010).

60. Ji, S., Park, J. & Lim, H. Improved antireflection properties of moth eye mimicking nanopillars on transparent glass: flat antireflection and color tuning. *Nanoscale* **4**, 4603–4610 (2012).

61. Li, Y. *et al.* Bioinspired Silica Surfaces with Near-Infrared Improved Transmittance and Superhydrophobicity by Colloidal Lithography. *Langmuir* **26**, 9842–9847 (2010).

62. Denbaars, S. P. *et al.* Development of gallium-nitride-based light-emitting diodes (LEDs) and laser diodes for energy-efficient lighting and displays. *Acta Mater.* **61**, 945–951 (2013).

63. Fujii, T. *et al.* Increase in the extraction efficiency of GaN-based light-emitting diodes via surface roughening. *Appl. Phys. Lett.* **84**, 855–857 (2004).

64. Zhong, H. *et al.* Enhancing the Light Extraction Efficiency of Blue Semipolar ($10\bar{1}\bar{1}$) Nitride-Based Light Emitting Diodes through Surface Patterning. *Jpn. J. Appl. Phys.* **48**, 030201 (2009).

65. Jung, S., Song, K.-R., Lee, S.-N. & Kim, H. Wet chemical etching of semipolar GaN planes to obtain brighter and cost-competitive light emitters. *Adv. Mater.* **25**, 4470–4476 (2013).

66. Kim, J.-J. *et al.* Biologically inspired LED lens from cuticular nanostructures of firefly lantern. *Proc. Natl. Acad. Sci.* **109**, 18674–18678 (2012).

67. Ng, W. N., Leung, C. H., Lai, P. T. & Choi, H. W. Nanostructuring GaN using microsphere lithography. *J. Vac. Sci. Technol. B Microelectron. Nanom. Struct.* **26**, 76–79 (2008).

68. Wang, Q., Bai, J., Gong, Y. P. & Wang, T. Influence of strain relaxation on the optical properties of InGaN/GaN multiple quantum well nanorods. *J. Phys. D. Appl. Phys.* **44**, 395102 (2011).

69. Fu, W. Y., Wong, K. K. Y. & Choi, H. W. Close-packed hemiellipsoid arrays: A photonic band gap structure patterned by nanosphere lithography. *Appl. Phys. Lett.* **95**, (2009).

70. Hsieh, M.-Y. *et al.* Improvement of external extraction efficiency in GaN-based LEDs by SiO2 nanosphere lithography. *IEEE Electron Device Lett.* **29**, 658–660 (2008).

Chapter 3

Experimental Methods: Colloidal Nanopatterning and Plasma Etching

Adapted from Article (To be Submitted):

Chan, L., and Gordon, M.J. “Geometric Tunability of Colloidal Nanopatterning and Plasma Etching,” (In preparation)

3.1 Colloidal lithography

A nanofabrication method to create nano- and micro-structured surfaces that is easy, robust, and scalable is highly desirable. Colloidal lithography, based on self-assembly and dip-coating of a colloidal crystal monolayer onto a substrate, followed by dry etching, can fulfill this need[1–4]. This method, as summarized in Figure 3.1, has been used to produce nano-cone and wire arrays in Si for anti-reflective surfaces for solar cells, vertical field effect transistors, and nanoimprint master molds[5–7]. Briefly, the process involves deposition of a self-assembled colloidal nanosphere or microsphere monolayer with pattern transfer using reactive-ion etching (RIE). Precise control of the final feature geometry (diameter, height, and pitch) from nm to μm length scales can be achieved by simply changing the colloid size, introducing a mask size-reduction etch, and modifying vertical etching parameters for pattern transfer[8,9]. Methods to drive self-assembly of functionalized colloids are many, including spin-coating[10,11], convective deposition[12,13], and Langmuir-Blodgett (LB) assembly[14–16]. Of these, LB deposition is of particular interest due to its reproducibility across multiple colloid length scales, ability to deposit close-packed patterns on curved or irregular surfaces, and scaling to large area applications.

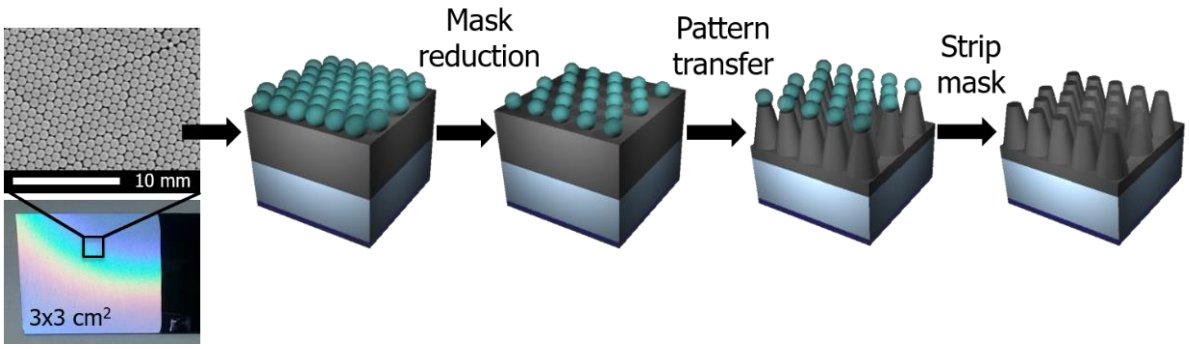

Figure 3.1: Schematic of colloidal lithography and pattern transfer process. A close-packed monolayer of colloidal nanospheres is deposited on the substrate. Mask size reduction and pattern transfer are both done using plasma etching, and the mask is stripped with either wet or dry etching. Reprinted from [24] with permission from the American Vacuum Society.

3.1.1 Langmuir-Blodgett dip-coating

The LB method[17,18], named for Irving Langmuir and Katherine Blodgett, who discovered that single monolayers of polymer films can be transferred to solid substrates, has been used extensively to deposit films for various applications, such as functional coatings, biological membranes, and thin-film electronics[14,19,20]. The deposition technique allows reproducible wafer-scale deposition of colloidal films onto many types of substrates, including substrates with curved or irregular surfaces. The technique has been adapted in this work for deposition of plasma etch masks for fabrication of ME-inspired anti-reflective surfaces and nanoscale light emitters[21–24]. The procedure is summarized in Figure 3.2(a). Deposition of hexagonally close-packed monolayer of silica colloids was completed by (i) functionalizing silica particles to render them hydrophobic, (ii) suspending functionalized colloids on an air-water

interface, (iii) compressing the surface using moving barriers to cause particles to self-assemble, and (iv) transferring particles onto a solid substrate via vertical dip coating while the surface pressure is kept constant.

In the work presented in this thesis, silica colloids with diameters ranging from 0.17-6 μm (Bangs Laboratories) were rendered hydrophobic via functionalization with allyltrimethoxysilane (ATMS) in acidic ethanol (pH = 5.5, acetic acid, 10% H_2O, and 10–20 mM ATMS). Functionalized colloids were dried in a vacuum oven (70°C, 12 h) and dispersed in 1:3 ethanol:chloroform prior to deposition. The deposition was carried out using an LB trough, that consists of a hydrophobic trough (PTFE) (3), hydrophilic barriers (polyoxymethylene, or Delrin) (2), a dipping mechanism (5), and a surface pressure sensor (4). A schematic of a LB trough is shown in Figure 3.2(b).

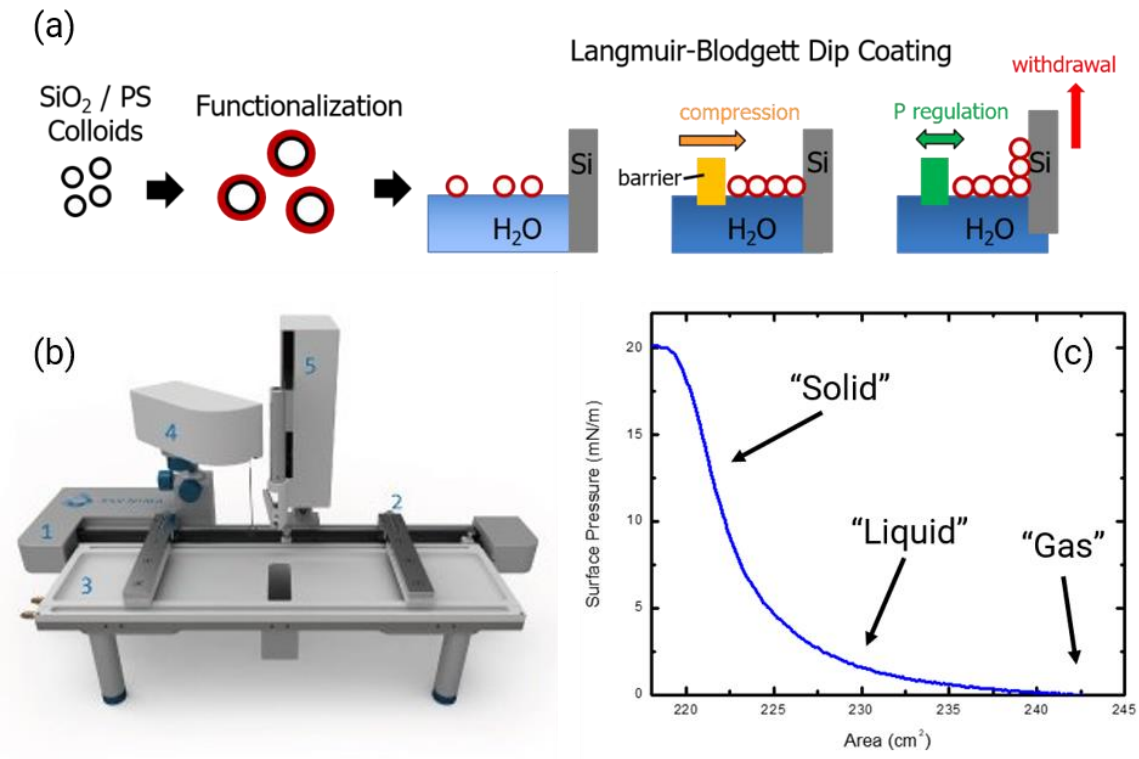

Figure 3.2: (a) Schematic of Langmuir-Blodgett deposition method. (b) Schematic of Langmuir-Blodgett trough consisting of (1) frame, (2) barriers, (3) trough top, (4) surface pressure sensor unit, and (5) dipping mechanism (Biolin Scientific, KSV Nima). (c) A typical surface pressure vs. area isotherm of silica colloids on a water subphase measured in a Langmuir-Blodgett trough. The "solid" region indicates close-packed monolayer formation.

Colloidal suspensions were deposited, drop-wise, onto the water subphase in the LB trough, where chloroform acts as a spreading agent and subsequently evaporates. Barriers compressed the interfacial film, while surface pressure was monitored with a Wilhelmy plate. The Wilhelmy plate was made of very thin platinum and downward forces acting on the plate consisted of gravity and surface tension, while upward forces consisted primarily of buoyancy due to displaced water. For a rectangular plate with dimensions l, w, and t for length, width, and thickness, respectively, and ρ_p for

plate density, immersed to a depth of h in a subphase with liquid density ρ_l, the net downward force can be found using the following equation:

$$F = \rho_p glwt + 2\gamma(tw)(cos\theta) - \rho_l gtwh \quad (3.1)$$

Here, γ is the surface tension of the liquid, g is the gravitational constant, and θ is the contact angle of the liquid on the plate. Surface pressure (Π) can be determined when the net downward force on the plate is known using the following equation:

$$\Pi = -\Delta\gamma = -\left[\frac{F}{2(t+w)}\right] = -\frac{\Delta F}{2w} \quad (3.2)$$

The overall degree of packing of the colloidal film is determined by measuring the surface pressure versus area isotherm. The isotherm is recorded while the film is compressed at a constant barrier translation rate with continuous measurement of γ using the Wilhelmy plate method. A typical surface pressure versus area isotherm is shown in Figure 3.2(c). The isotherm shows three distinct regions – the "gas," "liquid," and "solid" phases, which are determined by the physical and chemical properties of the film, but in the context of this work, relate to the degree of colloidal packing. The "solid" phase indicates the formation of a close-packed monolayer, and thus dip coating is done in this region. Colloidal deposition is carried out while the surface pressure is regulated, which involves a vertical dip-coat (pulling the substrate upward

out of the water) at a constant rate, while surface pressure is kept constant by adjusting the barrier position as colloids adhere to the surface of the solid substrate. Upon drying, a hexagonally close-packed monolayer of colloids is left on the substrate and is used as an etch mask for subsequent pattern transfer into the substrate via plasma etching.

3.1.2 Plasma etching

RIE and/or plasma etching is a standard microfabrication process that uses a reactive plasma to remove material, either chemically or physically due to high ion energy bombardment. RIE is advantageous over wet etching processes due to the anisotropy of the etch, which is critical for high fidelity pattern transfer. Generally, etch gases are flowed into a low pressure chamber, where a plasma discharge is maintained. High energy ions bombard the surface of the material, reacting or physically sputtering away material from the surface. Traditional reactive-ion etching tools generate a plasma in a parallel plate configuration. Inductively-coupled plasma (ICP) RIE also is commonly used, where plasma is generated with an RF powered magnetic field. In this configuration, higher plasma densities can be achieved, but etch profiles tend to be more isotropic. The plasma etching conditions (gas composition, pressure, power, bias) depend on the material being etched. In this work, CdTe, ZnS, and ZnSe were etched in $CH_4/H_2/Ar$ chemistry in a parallel plate RIE, while GaN/InGaN and SiO_2 where etched in Cl_2/N_2 and CF_4/Ar chemistries, respectively, in an ICP-RIE (Panasonic E640).

Optimized plasma etching conditions for the aforementioned materials are summarized in Tables 3.1 and 3.2.

	Gas Flow (sccm)	**Pressure**	**RF Forward Power**	**Bias Power**
CdTe Etch	$CH_4/H_2/Ar$ (3/24/3)	45 mTorr	500 V	Proportional to fwd
ZnS/ZnSe Etch	$CH_4/H_2/Ar$ (4/32/0)	40 mTorr	600 V	Proportional to fwd
O_2 Clean	O_2 (20)	50 mTorr	200 V	Proportional to fwd

Table 3.1: Standard plasma etching conditions for pattern transfer in CdTe, ZnS, and ZnSe, which was done in a parallel plate RIE (Materials Research Corporation RIE-51) with stage kept at 50°C. Cycles of etching (CdTe: 10 min, ZnS/ZnSe: 25 min) and O_2 (5 min) cleaning were done until the desired etch depth was achieved.

	Gas Flow (sccm)	**Pressure**	**RF Forward Power**	**Bias Power**
SiO_2 Mask Reduction	CF_4/Ar (40/10)	4.0 Pa	900 W	0 W
GaN Etch	Cl_2/N_2 (22.5/7.5)	0.2 Pa	500 W	300 W

Table 3.2: Standard plasma etching conditions for mask reduction and pattern transfer in GaN, which were done in an ICP-RIE (Panasonic E640).

3.1.3 Scalability and geometric tunability

Colloidal lithography combined with plasma etching is a scalable, reproducible, and geometry tunable nanofabrication approach to make nanostructured surfaces. The scalability of the approach is primarily determined by the colloid deposition step,

which can easily be performed on the wafer scale and on curved or even irregular surfaces. The nanostructure geometry using colloidal nanopatterning can be modified in a number of ways. The pitch, as shown in Figure 3.3(a-c) can be adjusted by using different colloid mask sizes. Length scales ranging from 170 nm up to 6 μm in diameter, have been demonstrated using this approach. The aspect ratio, or overall shape, of the nanostructures can also be modified, as shown in Figure 3.3(d), by modifying plasma etching conditions, such as etch gas composition, pressure, power, bias, etc.

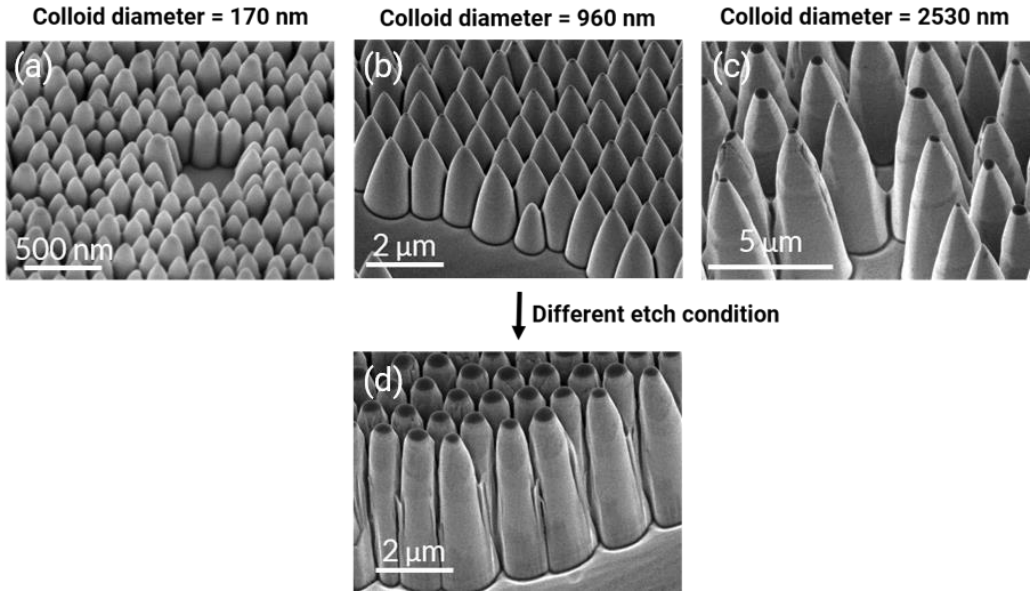

Figure 3.3: SEM images of (a-c) nanostructures fabricated with varying silica colloid diameters but same plasma etching conditions, resulting in features that have the same aspect ratio but varying pitch. (d) Nanostructures fabricated with 960 nm diameter colloidal masks, with a different etch condition from (b), resulting in higher aspect ratio features. Panels (a-c) reprinted from [23] with permission from OSA Publishing.

The nanostructure spacing can also be adjusted by introducing a mask size reduction etch, as shown in Figure 3.4. This was done with an ICP-RIE etch with no substrate bias, resulting in a relatively isotropic etch of the colloid itself. Plasma etching parameters were optimize such that the mask size reduction etching had high selectivity for the mask and not the substrate.

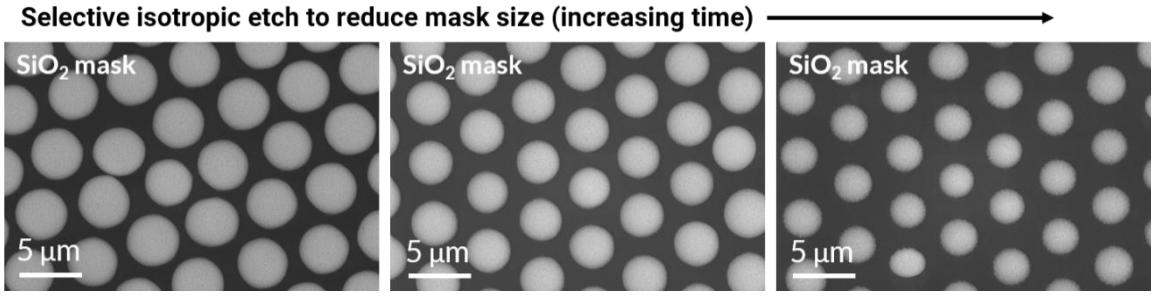

Figure 3.4: SEM images of SiO_2 colloids (original diameter ~ 6 μm) with isotropic etching using ICP-RIE in CF_4/Ar. As the etch time increased the mask diameter decreased.

The colloidal lithography and plasma etching approach has also been demonstrated on irregular surfaces, where silica nanospheres were deposited on micro-structured surfaces using the LB method and pattern transferred using plasma etching. Two examples are shown in Figure 3.5. In Figure 3.5(a), GaN micro-lens structures were fabricated using photolithography, photoresist reflow, and dry-etching. The LB method was used to deposit 310 nm diameter silica colloids on top and pattern transfer was done using plasma etching. Figure 3.5(b) shows results from a two-step colloidal patterning process, where large 6 μm pitch structures were first

fabricated using colloidal lithography and smaller 310 nm pitch structures were fabricated by a second LB deposition and pattern transfer process on top.

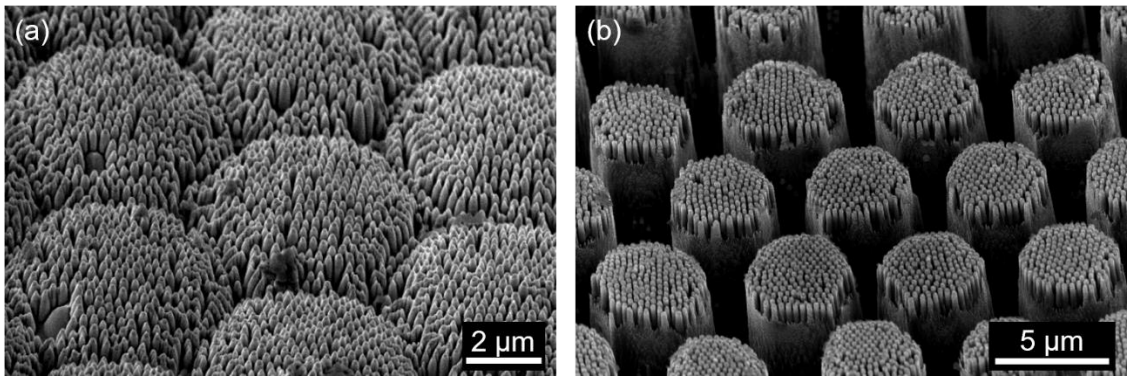

Figure 3.5: SEM images of nanostructures on (a) a GaN microlens array that was patterned using photolithography, photoresist reflow, and dry etching, and (b) a Si array on large 6 μm pitch structures fabricated using colloidal lithography.

Finally, chemical processing has also been implemented for added geometric tunability in the III-nitride material system. SEM images of structures that were fabricated using colloidal lithography and plasma-based mask size reduction and pattern transfer into a GaN/InGaN LED, are presented in Figure 3.6. A heated (~65°C - 75°C) KOH wet etch was done for 3 min to strip plasma damaged side-wall material after pattern transfer. This was done for three reasons: (1) to recover luminescence from the device, by removing plasma damaged or amorphous material deposited during the high power dry etching step, that kill luminescence by acting as defect states or traps, (2) to further reduce the nanorod diameter and, (3) to straighten the nanorod sidewalls, where wet etching terminates on the exposed m-plane[25,26]. The removal of plasma-damaged material introduced during the pattern transfer step is

essential for micro- and nanostructured LEDs, which suffer from sidewall recombination due to the large perimeter to area ratio[27], which will be discussed in more detail in Chapter 7.

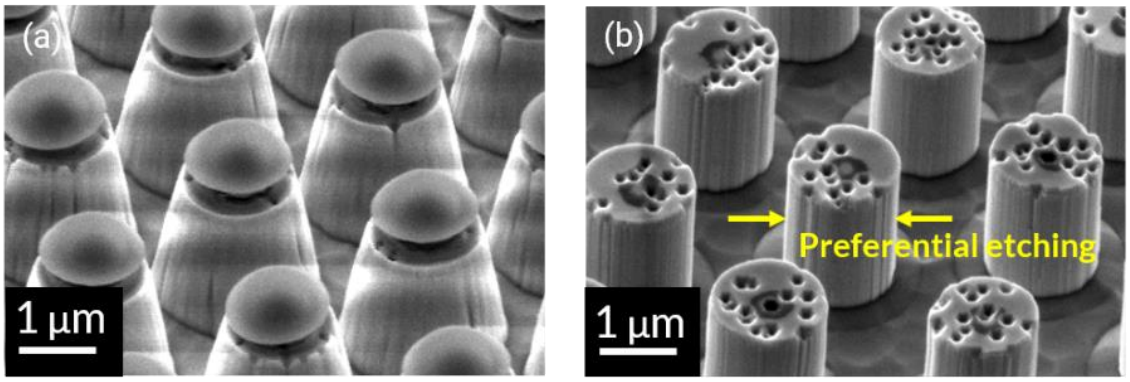

Figure 3.6: (a) SEM images of GaN/InGaN structures after colloid deposition of SiO_2 microspheres (d = 2530 nm), isotropic mask size reduction, and pattern transfer, where SiO_2 masks remain. (b) Structures after HF etching to strip the SiO_2 and a 3 min heated KOH wet etch (~70°C), where etching terminates on the m-plane, resulting in vertical sidewalls.

3.2 Summary

Colloidal lithography combined with plasma etching is a versatile patterning approach for fabrication of nano- and micro-scale surface structures. LB deposition of colloidal monolayers allows for wafer-scale assembly of nanosphere etch masks on solid surfaces, and is effective even on curved and irregular surfaces. Plasma etching has been shown to be a scalable pattern transfer technique, and can be used to tune structure geometry. Implementing an isotropic mask size reduction etch and chemical treatments adds further tunability, the latter of which also is essential for recovery of

light emission performance from micro- and nanostructured light emitting devices. The method discussed in this chapter has enabled the development of ME-inspired anti-reflective surfaces for IR applications, structured outcoupling surfaces for enhanced light extraction from LEDs, and nanoscale light emitters for next generation display applications, which will all be presented in greater detail in the following chapters of this thesis.

3.3 References

1. Hanarp, P., Sutherland, D. S., Gold, J. & Kasemo, B. Control of nanoparticle film structure for colloidal lithography. *Colloids Surfaces A Physicochem. Eng. Asp.* **214**, 23–36 (2003).

2. Zhang, G. & Wang, D. Colloidal Lithography-The Art of Nanochemical Patterning. *Chem. - An Asian J.* **4**, 236–245 (2009).

3. Burmeister, F. *et al.* From Mesoscopic to Nanoscopic Surface Strutures: Lithography with Colloid Monolayers. *Adv. Mater.* **10**, 495–497 (1998).

4. Fredriksson, H. *et al.* Hole-mask colloidal lithography. *Adv. Mater.* **19**, 4297–4302 (2007).

5. Hsu, C. M., Connor, S. T., Tang, M. X. & Cui, Y. Wafer-scale silicon nanopillars and nanocones by Langmuir-Blodgett assembly and etching. *Appl. Phys. Lett.* **93**, 133109 (2008).

6. Zhu, J. *et al.* Optical Absorption Enhancement in Amorphous Silicon Nanowire and Nanocone Arrays. *Nano Lett.* **9**, 279–282 (2009).

7. Zhu, J., Yu, Z., Fan, S. & Cui, Y. Nanostructured photon management for high performance solar cells. in *Materials Science and Engineering R: Reports* **70**, 330–340 (2010).

8. Lora Gonzalez, F., Chan, L., Berry, A., Morse, D. E. & Gordon, M. J. Simple colloidal lithography method to fabricate large-area moth-eye antireflective structures on Si, Ge, and GaAs for IR applications. *J. Vac. Sci. Technol. B* **32**, 051213 (2014).

9. Gonzalez, F. L. & Gordon, M. J. Bio-inspired, sub-wavelength surface structures for ultra-broadband, omni-directional anti-reflection in the mid and far IR. *Opt. Express* **22**, 12808 (2014).

10. Jiang, P., Prasad, T., McFarland, M. J. & Colvin, V. L. Two-dimensional nonclose-packed colloidal crystals formed by spincoating. *Appl. Phys. Lett.* **89**, 011908 (2008).

11. Jiang, P. & McFarland, M. J. Large-scale fabrication of wafer-size colloidal crystals, macroporous polymers and nanocomposites by spin-coating. *J. Am. Chem. Soc.* **126**, 13778–13786 (2004).

12. Kim, M. H., Im, S. H. & Park, O. O. Rapid fabrication of two- and three-dimensional colloidal crystal films via confined convective assembly. *Adv. Funct. Mater.* **15**, 1329–1335 (2005).

13. Kumnorkaew, P. & Gilchrist, J. F. Effect of nanoparticle concentration on the convective deposition of binary suspensions. *Langmuir* **25**, 6070–6075 (2009).

14. Roberts, G. G. An applied science perspective of Langmuir-Blodgett films. *Adv. Phys.* **34**, 475–512 (1985).

15. Szekeres, M. *et al.* Ordering and optical properties of monolayers and multilayers of silica spheres deposited by the Langmuir–Blodgett method. *J. Mater. Chem.* **12**, 3268–3274 (2002).

16. Reculusa, S. & Ravaine, S. Synthesis of colloidal crystals of controllable thickness through the Langmuir-Blodgett technique. *Chem. Mater.* **15**, 598–605 (2003).

17. Langmuir, I. The Constitution and Fundamental Properties of Solids and Liquids. *J. Am. Chem. Soc.* **39**, 1848–1906 (1917).

18. Blodgett, K. B. Films Built by Depositing Successive Monomolecular Layers on a Solid Surface. *J. Am. Chem. Soc.* **57**, 1007–1022 (1935).

19. Chen, X. *et al.* Langmuir-blodgett patterning: A bottom-up way to build mesostructures over large areas. *Acc. Chem. Res.* **40**, 393–401 (2007).

20. Cote, L. J., Kim, F. & Huang, J. Langmuir-blodgett assembly of graphite oxide single layers. *J. Am. Chem. Soc.* **131**, 1043–1049 (2009).

21. Chan, L., Decuir Jr, E. A., Fu, R., Morse, D. E. & Gordon, M. J. Biomimetic nanostructures in ZnS and ZnSe provide broadband anti-reflectivity. *J. Opt.* **19**, 114007 (2017).

22. Ley, R. *et al.* Strain relaxation of InGaN/GaN multi-quantum well light emitters via nanopatterning. *Opt. Express* **27**, 30081–30089 (2019).

23. Pynn, C. D. *et al.* Enhanced light extraction from free-standing InGaN/GaN light emitters using bio-inspired backside surface structuring. *Opt. Express* **25**, 15778 (2017).

24. Chan, L. *et al.* Fabrication and optical behavior of graded-index, moth-eye antireflective structures in CdTe. *J. Vac. Sci. Technol. B* **35**, 011201 (2017).

25. Li, Q. *et al.* Optical performance of top-down fabricated InGaN/GaN nanorod light emitting diode arrays. *Opt. Express* **19**, 25528 (2011).

26. Park, H., Baik, K. H., Kim, J., Ren, F. & Pearton, S. J. A facile method for highly uniform GaN-based nanorod light-emitting diodes with InGaN/GaN multi-quantum-wells. *Opt. Express* **21**, 12908–13 (2013).

27. Wong, M. S. *et al.* Size-independent peak efficiency of III-nitride micro-light-emitting-diodes using chemical treatment and sidewall passivation. *Appl. Phys. Express* **12**, (2019).

28. Wong, M. S. *et al.* High efficiency of III-nitride micro-light-emitting diodes by sidewall passivation using atomic layer deposition. *Opt. Express* **26**, 21324 (2018).

29. Choi, W. H. *et al.* Sidewall passivation for InGaN/GaN nanopillar light emitting diodes. *J. Appl. Phys.* **116**, (2014).

30. Chen, L.-Y. *et al.* High performance InGaN/GaN nanorod light emitting diode arrays fabricated by nanosphere lithography and chemical mechanical polishing processes. *Opt. Express* **18**, 7664–7669 (2010).

31. Chen, L.-Y. *et al.* Investigation of the strain induced optical transition energy shift of the GaN nanorod light emitting diode arrays. *Opt. Express* **19**, A900–A907 (2011).

Chapter 4

Fabrication and optical behavior of graded-index, moth-eye anti-reflective structures in CdTe

Adapted from the *Journal of Vacuum Science and Technology B* Article:

Chan, L., Ghoshal, A., DeCruir Jr., E.A., Chen, Y.P., Morse, D.E., Gordon, M.J., *J. Vac. Sci. Technol. B* **35**, 011201 (2017).

4.1 Chapter overview

A simple and scalable method, based on dip-coat colloidal lithography, mask reduction, and plasma-based pattern transfer, is presented to create graded-index, moth eye-inspired anti-reflective features on II-VI semiconductors. Hexagonal arrays of isolated conical frusta with tunable geometry (top diameter = 200-1300 nm, pitch = 310-2530 nm, and height = 790-7100 nm) were realized by isotropic etching of various size silica colloid masks before pattern transfer into the underlying substrate. Substantial increases in single-side direct and total infrared (IR) transmission across the 4-20 μm range (9-15% for CdTe thin films and 18% for bulk CdTe) were achieved, in excellent agreement with transfer matrix (TMM) calculations and finite-difference time-domain (FDTD) optical simulations. The fabrication method presented can be used to enhance efficiency in multiple IR application areas including photovoltaics, optical system components, detectors, and focal plane array imagers.

4.2 Introduction

CdTe is a versatile II-VI semiconductor material with applications ranging from photovoltaics[1–3] and IR sensing and imaging[4,5] to all manner of optical components (e.g., windows, lenses, prisms, etc.) used in electro-optical infrared (EO/IR) and laser systems[6–8]. The transmission range of CdTe is exceptionally broad (λ=0.85-30 μm)[8], but due to its relatively high refractive index (n~2.65 at 10 μm), large refection (Fresnel) losses[9,10] typically occur at air-CdTe interfaces. As a result, high performance anti-

reflection coatings (ARCs) are often required for CdTe device structures, substrates, and components. Interference-based ARCs have traditionally been used to solve this problem; unfortunately, single-layer coatings have narrow bandwidths and poor angular response, and multi-layer coatings are expensive, time consuming to manufacture, and substrate specific, leading to high cost and limited scalability[11,12]. CdTe surfaces have also been rendered anti-reflective (AR) by coating the interface of interest with nanostructures (e.g., via glancing angle deposition - GLAD[13]) and by etching moth eye-like features directly into the surface[14–16] (e.g., via optical/e-beam lithography + dry etching) to create a sub-wavelength, graded refractive index profile[17]. The latter is particularly appealing because the moth-eye (ME) approach allows large field of view (i.e., AR at non-normal incidence), large bandwidth, and theoretically can be tuned to any wavelength range of interest[18,19]. Herein, we present a simple and scalable fabrication method to realize ME structures in CdTe and other II-VI materials that combines colloidal lithography with plasma-based mask reduction and pattern transfer steps. Hexagonal ME arrays with various feature sizes (310-2500 nm diameter with aspect ratios up to 5:1) were created in bulk CdTe and MBE-grown CdTe thin films. Significant enhancement in IR transmission (average = 9-15% from 4 to 20 μm; maximum = 22% from 16 to 20 μm) was observed for MEs relative to flat surfaces. Optical behavior was simulated using the transfer matrix method (TMM) and finite-difference time-domain (FDTD) techniques, which were seen to accurately model both peak transmission and etaloning in thin films. The largest ME features

(2530 nm mask) also exhibited considerable diffuse forward scattering behavior in the small wavelength limit ($\lambda < 6$ μm).

4.3 Experimental methods

Moth eye nanostructures were fabricated on 1 mm thick bulk CdTe substrates (ISP Optics) and CdTe thin films (14.9 μm of MBE-grown CdTe on Si(211) with 860 nm of backside SiO_2) using colloidal lithography and plasma etching, as described in Fig. 4.1(a). Silica colloids (d = 310, 690, and 2530 nm) were functionalized with allyltrimethoxysilane (ATMS, Sigma-Aldrich, >98%) in acidic ethanol (pH = 5.5, acetic acid, 10% H_2O, and 10–20 mM ATMS), cured in a vacuum oven (70°C, 12 h), and dispersed in 1:3 ethanol:chloroform. Silica colloids were suspended on a H_2O subphase in a Langmuir Blodgett (LB) trough, compressed, and dip-coated on the substrate of interest at constant surface pressure to form hexagonally close-packed monolayers. After deposition, size reduction was performed on the silica mask using an isotropic reactive ion etch (Panasonic E460 ICP-RIE) with 40/10 sccm of CF_4/Ar at 30 mTorr, 900 W ICP power, and no sample bias. The size reduction step was followed by pattern transfer using an anisotropic plasma etch with 3/24/3 sccm of CH_4/H_2/Ar at 45 mTorr and 500 V bias in a parallel plate RIE (Materials Research Corporation RIE-51) with 50°C chuck. An O_2 plasma clean was done after every five minutes of CH_4/H_2/Ar etching to remove polymer layers deposited during etching. The remaining silica mask was removed using the same CF_4/Ar dry etch described previously, leaving behind

hexagonally close-packed conical frusta. As shown in Fig. 4.2(a), isolated ME features could not be obtained without mask reduction due to insufficient space between the silica spheres and slow silica etch rate in $CH_4/H_2/Ar$. SEM images of the final ME nanostructures using mask reduction are shown in Figs. 4.2(b)-(d). Direct (straight through, ~0.004π sr about the sample normal) and total (sample mounted on an Au-coated integrating sphere with ~1.92π sr capture from sample back side) transmission of samples from λ = 2-20 μm were measured using a Bruker Equinox-55 FTIR with LN_2-cooled HgCdTe (MCT) detector.

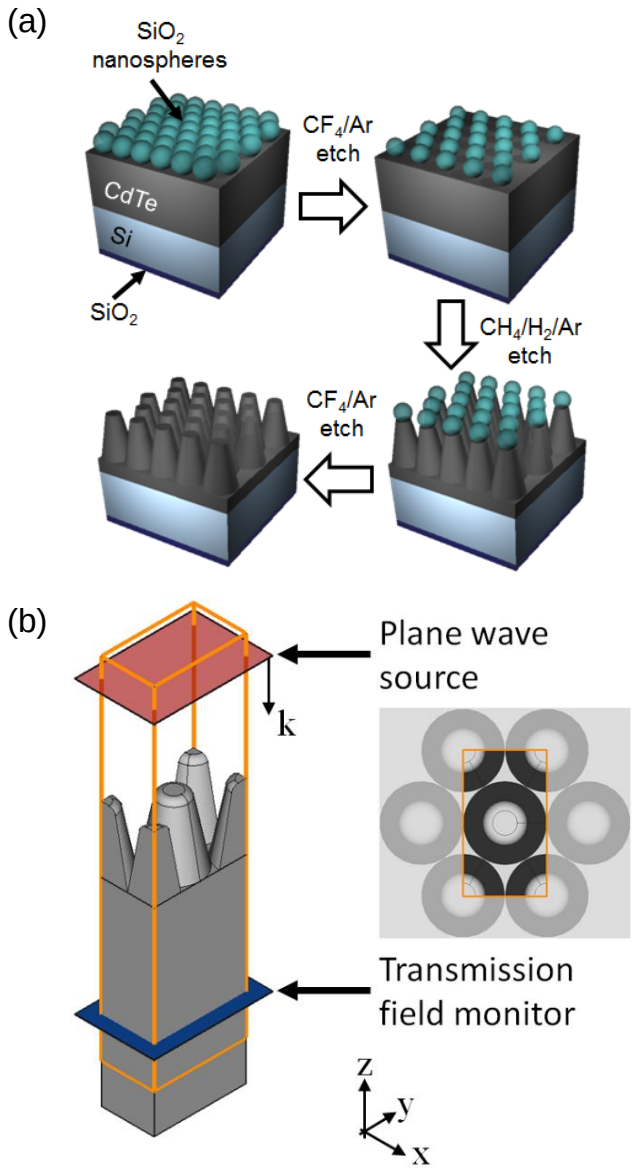

Figure 4.1: (a) Process flow to create moth eye nanostructures in CdTe using colloidal lithography, mask reduction, and plasma etching. Sample shown is 14.9 μm thick MBE-grown CdTe on 500 μm thick Si substrate with 860 nm of backside SiO_2. (b) FDTD model and simulation domain for moth eye structured substrates. Reprinted with permission from the American Vacuum Society.

The electromagnetic behavior of ME nanostructures was analyzed using the TMM[20] (programmed in-house with MATLAB) and FDTD simulations (Lumerical[21]).

For the TMM calculations, ME features were divided into 500 'thin film' layers parallel to the substrate surface with the effective refractive index of each layer calculated using the Bruggeman approximation[22,23] and volume-based fill fraction of ME features at each layer height. Absolute squares of the Fresnel reflection and transmission coefficients were used to model interfaces of thick (substrate) layers[24]. The simulation domain for FDTD calculations consisted of hexagonally close-packed frusta with rounded edges in the x-y plane, as detailed in Fig. 4.1(b); ±z boundaries were perfectly matched (absorbing) layers with periodic boundaries in the x- and y-directions. For bulk CdTe, a semi-infinite CdTe layer in the -z direction was used; whereas, for CdTe on Si, the entire CdTe layer was included in the simulation, with the underlying Si layer extending to infinity in the -z direction. A plane wave source (λ = 1-20 μm) with wavevector *k* in the -z direction (red rectangle) was set close to the upper boundary. The transmitted field was recorded with a field monitor (blue rectangle) below the ME features. These data were used to calculate far-field transmission (normalized to excitation source power) using Lumerical's built-in far-field calculation module. Simulations for both x- and y-polarized excitations were done and averaged. Since calculations with a thick substrate were computationally prohibitive, calculations were performed for ME structures on a semi-infinite substrate. Material properties of Si and CdTe were based on Lumerical-generated fits to literature data[10,25] that (i) ignore the Si phonon absorption at ~ 16 μm and (ii) require inclusion of a finite, but very small, absorption (i.e., $\varepsilon'' \sim 10^{-9}$) so as to fit the real part of the CdTe refractive

index in the short-wavelength range. Geometric parameters of the simulated ME features were set to reproduce the actual structures as determined by SEM. To compare experimental results with FDTD calculations (i.e., ME structures on a finite CdTe or Si substrate vs. semi-infinite substrate, respectively), experimental transmission data were scaled by the transmission of a substrate-air interface to provide a first order approximation of removing the bottom (unstructured) substrate interface.

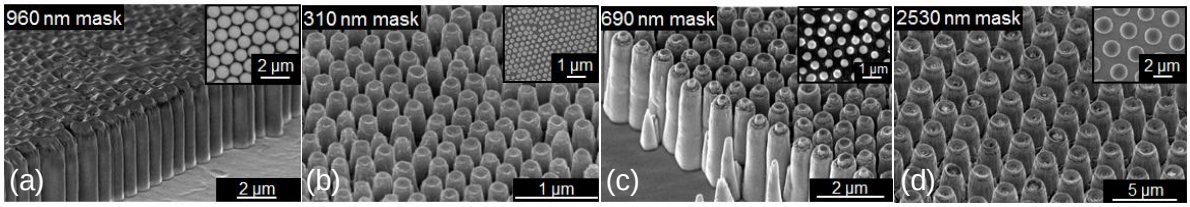

Figure 4.2: SEM images of ME nanostructures fabricated with (a) 960 nm mask and no mask size reduction etch, and with (b) 310 nm, (c) 690 nm, and (d) 2530 nm masks produced by mask reduction. Insets: SEM images of silica masks on the CdTe used for pattern transfer. Reprinted with permission from the American Vacuum Society.

4.4 Results and discussion

ME structures on 1 mm thick bulk CdTe were fabricated with a mask diameter of 690 nm and an etch depth of 3.4 μm using the mask size reduction + pattern transfer process (Figs. 4.1(a) and 4.2). Figure 4.3 summarizes the measured direct (straight through) and total (~1.92π sr collection from sample back side) transmission, with TMM and FDTD predictions for comparison. Several cases for the TMM are shown: (i) flat, unstructured CdTe (dashed black); (ii) single-side ME with frustum top radius of

5 nm (dashed grey), i.e., a nearly perfect cone; and (iii) single-side ME having the actual (frustum) geometry determined by SEM (dashed red). FDTD results are for the actual ME geometry. As can be seen, there is a significant increase (up to 18% near 6 μm) in both direct and total transmission with ME structures compared to a flat surface in the λ = 4-10 μm range. Both TMM and FDTD spectra for the actual structure show considerable etaloning, due to interference that arises from refractive index jumps at the frustum top (air-CdTe) and base (i.e., frusta do not cover 100% of the CdTe substrate, even if hexagonally closed packed). The former is indeed verified by the TMM-calculated perfect conical case (dashed grey); no fringes are seen because the refractive index transition at the cone apex is gradual. The absence of fringes in the measured data is hypothesized to originate from an analogous effect: refractive index transitions are smoothed by micro-structuring (roughness) of the frustum top and imperfect pattern transfer at the frustum base (absence of flat areas between frusta). The difference between the direct and total transmission measured in the 2-4 μm range is attributed to high-angle scattering by irregularities in the ME structure and other scattering structures formed as a by-product of the etching process[26].

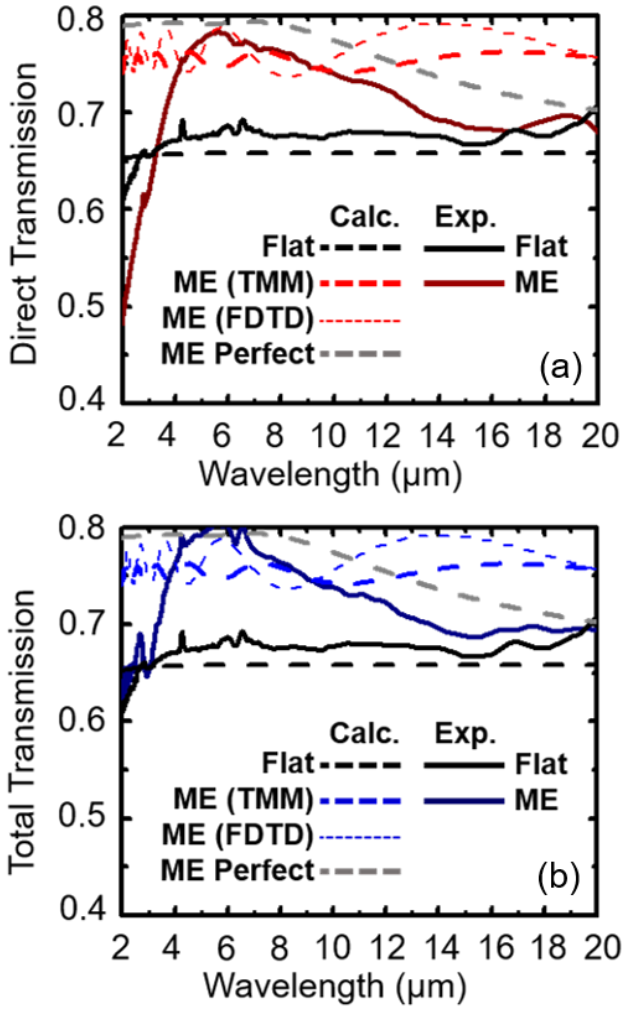

Figure 4.3: Experimentally measured (solid), TMM-calculated (dashed), and FDTD-calculated (fine dash), direct (a) and total transmission (b) of a 1 mm thick bulk CdTe substrate with (red, blue) and without (black) ME structuring on one side, as well as TMM-calculated perfect ME structuring (grey). ME features were fabricated using a 690 nm initial silica mask. See Results section for details. Reprinted with permission from the American Vacuum Society.

To demonstrate application of the aforementioned ME fabrication technique to focal plane array substrates, pattern transfer and optical measurements were carried out on 14.9 μm thick, MBE-grown CdTe films on Si (211) substrates. ME structures were fabricated using mask diameters of 310 nm, 690 nm, and 2530 nm, with corresponding

etch depths of 0.79 μm, 3.4 μm, and 7.07 μm, respectively. Figure 4.4 summarizes the measured and FDTD-calculated transmission spectra for ME-structured CdTe films and flat CdTe films on Si substrates. As described above, the measured data for both the unstructured and structured CdTe films were scaled by the transmission of a Si-air interface, both to approximately remove the effect of reflections at the Si-air interface and to evaluate ME efficacy. For clarity, only FDTD results are shown, as they appropriately capture both the long wavelength limit and near-field (diffractive) effects at higher angles. Note that reduction in the measured transmission at ~16 μm was due to phonon absorption in Si, which was not accounted for in the simulations. Thus, other than the Si phonon absorption, we find that the measured transmission data closely follow the expected transmission based on FDTD simulations in the λ = 4-20 μm range for the 310 nm and 690 nm masked samples, and λ = 6-20 μm range for the 2530 nm masked samples. For features in the short wavelength range (2-4 μm for the 310 nm and 690 nm ME samples, 2-6 μm for the 2530 nm ME samples), the calculated transmission for flat samples (dashed black) is slightly lower than experimental values (solid black) in the 2-3 μm range in all cases. We attribute this slight reduction to the small, but artificially introduced, ε'' loss discussed in the Methods section above.

Examining panels (a)-(c), one observes that the onset of direct transmission falloff occurs at increasing wavelength as the ME pitch becomes larger. We attribute this effect to three factors: (i) high-angle forward scattering due to defects in the ME

structures, (ii) backscattering due to the same defects, and (iii) diffraction. Specifically, the increase in total transmission for the 310 nm structures (panel (d)) is due to forward scattering by defects, as diffraction does not play a role. In addition to (i), the 690 nm ME structures (panel (e)) also diffract light at higher orders at λ = 2-3 μm. Backscattering is likely the reason that the measured transmission is less than the calculated total. In contrast, the 2530 nm ME structures show a significant drop in transmission in the 2-6 μm range, a large portion of which was recovered in the total transmission measurements; FDTD calculations show this to be due to the many diffracted orders in the 2-6 μm range.

All spectra in Figure 4.4, both measured and calculated, have interference fringes from etaloning due to Fabry-Perot cavity effects in the thin CdTe layer. For a perfect, anti-reflecting graded refractive index structure, we can expect no interference fringes. It is no doubt that the aforementioned abrupt refractive index changes at the frustum top and bottom are at play, but the abrupt index change at the CdTe-Si interface must also be considered. Therefore, we can expect that interference at these three interfaces causes the interference patterns observed. It was indeed confirmed via FDTD simulations (not shown) that interference fringes did disappear when refractive index transitions were smooth, either at the top of the ME structure (pointed cone), or at the bottom of the ME layer (square packing of square pyramids) when the CdTe-Si interface was effectively removed.

Interference fringes (i.e., caused by etaloning from the abrupt CdTe-Si interface, as

the aforementioned transmission model shows) makes interpreting the efficacy of ME structures challenging. We overcome this issue by calculating the average transmission in the λ = 6-20 μm range for the 310 nm and 690 nm ME structures, and in the 10-20 μm range for the 2530 nm ME structures. Using such a metric, the 310 nm, 690 nm, and 2530 nm ME structures increase the average direct transmission by 9%, 14%, and 15%, respectively. The maximum increase for the 310 nm, 690 nm, and 2530 nm ME structures was 14%, 19%, and 22% in direct transmission, respectively. For CdTe optics and bulk substrate devices, thin film interfaces with 'inherently' and unavoidable abrupt refractive changes are absent, and the expected transmission enhancement (~ 18%+) will be similar to that shown in Fig. 4.3.

Previous studies of similar ME structures displayed a strong advantage in transmission for a large range of angles of incidence. For example, Lora *et. al.* created ME structures in Si that showed significant advantage in transmission over an unstructured Si surface at angles of incidence up to 60°[18]. The measured transmission up to 30° for the ME structured surface was within 2% of the calculated theoretical maximum transmission for single-side anti-reflective Si. Furthermore, the omni-directional transmission enhancement was largely wavelength independent. As the structures presented here were fabricated using similar processes in CdTe, we expect that the angular behavior is also similarly advantageous.

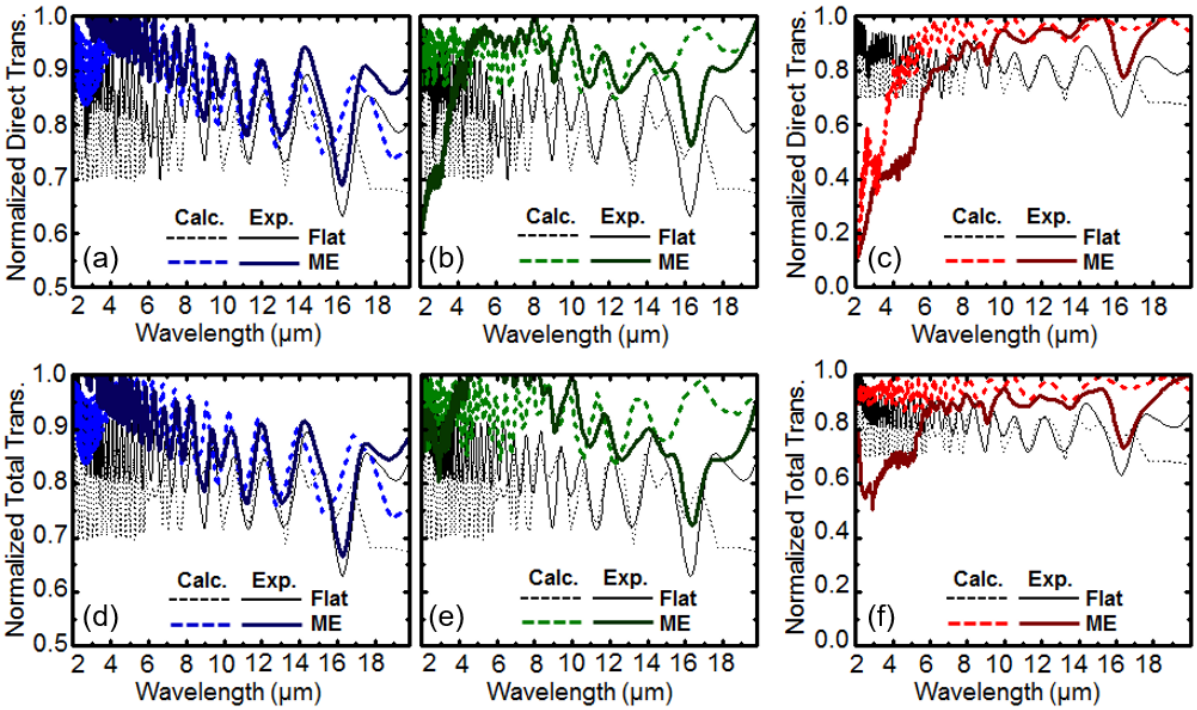

Figure 4.4: Experimentally measured (solid) and calculated (dashed) direct (a, b, c) and total (d, e, f) transmission of CdTe/Si samples with and without ME structuring. ME features were fabricated with initial mask diameters of 310 nm (a, d, blue), 690 nm (b, e, green), and 2530 nm (c, f, red). Reprinted with permission from the American Vacuum Society.

4.5 Summary

This chapter described a simple and scalable method for suppressing reflections at air-II-VI semiconductor interfaces, based on colloidal lithography, mask reduction, and plasma pattern transfer. Mask reduction before pattern transfer was introduced to enable high fidelity pattern transfer into a CdTe substrate, as well as tuning of the moth eye feature size and aspect ratio. Substantial single-side transmission enhancements (9-15% on CdTe thin films and 18% on bulk CdTe) were obtained over the short, mid, and far IR wavelength ranges (λ = 6-20 μm) by simply adjusting colloidal

mask size (310-2530 nm). TMM and FDTD simulations were used to validate experimental results, providing a basis for comparison through normalization to a theoretical maximum transmission. The fabrication method and ME structures presented herein could be implemented in various II-VI application areas to enhance efficiency of photovoltaics by reducing optical losses, improving transmission of EO/IR optical components, and increasing signal-to-noise ratio and image contrast in IR detectors and focal plane imagers.

4.6 References

1. Chopra, K. L., Paulson, P. D. & Dutta, V. Thin-film solar cells: an overview. *Prog. Photovoltaics Res. Appl.* **12**, 69–92 (2004).

2. Dobson, K. D., Visoly-Fisher, I., Hodes, G. & Cahen, D. Stability of CdTe/CdS thin-film solar cells. *Sol. Energy Mater. Sol. Cells* **62**, 295–325 (2000).

3. Fan, Z. *et al.* Three-dimensional nanopillar-array photovoltaics on low-cost and flexible substrates. *Nat. Mater.* **8**, 648–653 (2009).

4. Rogalski, A. Infrared detectors: Status and trends. *Progress in Quantum Electronics* **27**, 59–210 (2003).

5. Rogalski, A. HgCdTe infrared detector material: history, status and outlook. *Reports Prog. Phys.* **68**, 2267–2336 (2005).

6. Deutsch, T. F. Absorption coefficient of infrared laser window materials. *J. Phys. Chem. Solids* **34**, 2091–2104 (1973).

7. Harris, D. C. Durable 3–5 μm transmitting infrared window materials. *Infrared Phys. Technol.* **39**, 185–201 (1998).

8. Bell, R. O. Review of optical application of CdTe. *Rev. Phys. Appliquée* **12**, 391–399 (1977).

9. Marple, D. T. F. Refractive index of ZnSe, ZnTe, and CdTe. *J. Appl. Phys.* **35**, 539–542 (1964).

10. DeBell, A. G. *et al.* Cryogenic refractive indices and temperature coefficients of cadmium telluride from 6 μm to 22 μm. *Appl. Opt.* **18**, 3114–3115 (1979).

11. Raut, H. K., Ganesh, V. A., Nair, A. S. & Ramakrishna, S. Anti-reflective coatings: A critical, in-depth review. *Energy Environ. Sci.* **4**, 3779–3804 (2011).

12. Kaminski, P. M., Lisco, F. & Walls, J. M. Multilayer Broadband Anti-Reflective Coatings for Bulk Heterojunction Polymer Solar Cells. *IEEE J. Photovoltaics* **4**, 452–456 (2014).

13. Sood, A. K. *et al.* Development of Nanostructured Antireflection Coatings for EO/IR Sensor and Solar Cell Applications. *Mater. Sci. Appl.* **03**, 633–639 (2012).

14. Huang, Y.-F. *et al.* Improved broadband and quasi-omnidirectional anti-reflection properties with biomimetic silicon nanostructures. *Nat. Nanotechnol.* **2**, 770–774 (2007).

15. Wilson, S. J. & Hutley, M. C. The Optical Properties of 'Moth Eye' Antireflection Surfaces. *Opt. Acta Int. J. Opt.* **29**, 993–1009 (1982).

16. Chattopadhyay, S. *et al.* Anti-reflecting and photonic nanostructures. *Mater. Sci. Eng. R* **69**, 1–35 (2010).

17. MacLeod, B. D. & Hobbs, D. S. Long life, high performance anti-reflection treatment for HgCdTe infrared focal plane arrays. in *SPIE Defense and Security Symposium* **6940**, 1–16 (2008).

18. Gonzalez, F. L. & Gordon, M. J. Bio-inspired, sub-wavelength surface structures for ultra-broadband, omni-directional anti-reflection in the mid and far IR. *Opt. Express* **22**, 12808 (2014).

19. Lora Gonzalez, F., Chan, L., Berry, A., Morse, D. E. & Gordon, M. J. Simple colloidal lithography method to fabricate large-area moth-eye antireflective structures on Si, Ge, and GaAs for IR applications. *J. Vac. Sci. Technol. B* **32**, 051213 (2014).

20. Born, M. & Wolf, E. *Principles of optics : electromagnetic theory of propagation, interference and diffraction of light*. (Cambridge University Press, 1999).

21. Lumerical Solutions Inc. FDTD Solutions. http://www.lumerical.com/tcad-products/fdtd/ (2017).

22. Bruggeman, D. A. G. Berechnung verschiedener physikalischer Konstanten von heterogenen Substanzen. I. Dielektrizitätskonstanten und Leitfähigkeiten der Mischkörper aus isotropen Substanzen. *Ann. Phys.* **24**, 636–664 (1935).

23. Niklasson, G. A., Granqvist, C. G. & Hunderi, O. Effective medium models for the optical properties of inhomogeneous materials. *Appl. Opt.* **20**, 26–30 (1981).

24. Katsidis, C. C. & Siapkas, D. I. General transfer-matrix method for optical multilayer systems with coherent, partially coherent, and incoherent interference. *Appl. Opt.* **41**, 3978–3987 (2002).

25. Palik, E. D. *Handbook of optical constants of solids*. (Academic Press, 1998).

26. Gonzalez, F. L., Morse, D. E. & Gordon, M. J. Importance of diffuse scattering phenomena in moth-eye arrays for broadband infrared applications. *Opt. Lett.* **39**, 13–16 (2014).

Chapter 5

Biomimetic nanostructures in ZnS and ZnSe provide broadband anti-reflectivity

Adapted from the *Journal of Optics* Article:

Chan, L., Decuir Jr., E.A., Fu, R., Morse, D.E., and Gordon, M.J., *J. Opt*. **19**, 114007 (2017). (Invited Article)

5.1 Chapter overview

Graded-index, moth eye-inspired anti-reflective features were fabricated in ZnS and ZnSe via nanosphere lithography using a Langmuir Blodgett dip-coating method with plasma-based mask reduction and pattern transfer. Arrays of hexagonally close-packed conical frusta (top diameter = 300 nm, pitch = 690 nm, height = 2800 nm) were realized by isotropic etching (size-reduction) of the colloidal mask with CF_4/Ar, followed by pattern transfer into the substrate using CH_4/H_2 plasma etching. Substantial increases in broadband transmission were achieved across the 2-20 μm range, yielding 23% and 26% single-side transmission improvement, and 92% and 88% absolute double-side transmission for ZnS and ZnSe, respectively, in excellent agreement with finite difference time domain (FDTD) optical simulations. The fabrication method presented can be used to enhance efficiency for multiple IR applications by minimizing reflective losses, while offering the further advantages of scalability and low cost.

5.2 Introduction

ZnS (band gap = 3.54 eV, 350 nm) and ZnSe (band gap = 2.70 eV, 460 nm) are versatile II-VI semiconductor materials with many applications, including windows, lenses, filters and other optical components for the visible and IR[1]; light harvesters[2,3]; lighting phosphors[4]; and LEDs and lasers when appropriately doped[5–10]. Their wide bandgaps provide excellent transmission in the visible and IR (0.35-12 μm for ZnS; 0.45-20 μm

for ZnSe[11,12]), but their high refractive indices (n_{ZnS} = 2.2, n_{ZnSe} = 2.4 at λ=10 μm[13–16]) often lead to large Fresnel (reflection) losses that can decrease optical device performance in many venues[17–20]. As a result, high performance anti-reflection coatings (ARCs) are often required for ZnS/ZnSe device structures, substrates, and components. Interference-based ARCs have traditionally been used to solve this problem; unfortunately, however, single-layer coatings tend to have narrow bandwidths and poor angular response, and multi-layer coatings are expensive, time consuming to manufacture and substrate specific, leading to high cost and limited scalability[21,22]. ZnS/ZnSe surfaces have also been rendered anti-reflective by etching sub-wavelength scale features directly into the surface (e.g., via optical/e-beam/interference based lithography + dry etching) to create a graded refractive index (GRIN) profile[23,24]. This approach, also known as the moth eye (ME) method[25–27], is particularly appealing because it allows large field of view (i.e., AR at non-normal incidence), large bandwidth, and can theoretically be implemented in any material that can be selectively etched[28,29]. Previous studies showed successful fabrication of ME structures in CdTe for IR focal plane array applications using a nanosphere lithography method with a mask reduction step before pattern transfer[30]. Using a similar approach here, we have successfully etched ME structures in both ZnS and ZnSe with a height of 2800 nm, top diameter of 100-200 nm, and pitch of 690 nm. Substantial increases in single-side (23% and 26% improvement for ZnS and ZnSe, respectively) and double-side (92% and 88% absolute transmission for ZnS and ZnSe,

respectively) total IR transmission across the λ=2-20 μm range were achieved, in excellent agreement with finite difference time domain (FDTD) simulations. Below λ=2 μm, where ME feature size was on the order of the wavelength, it was seen that diffractive effects became increasingly more important, leading to a large fall off in transmission - due in large part to diffuse forward scattering.

5.3 Experimental methods

Moth eye nanostructures were fabricated on 1 mm thick bulk ZnS and ZnSe substrates (ISP Optics) using colloidal lithography and plasma etching. Silica colloids (d = 690 nm) were functionalized with allyltrimethoxysilane (ATMS, Sigma-Aldrich, >98%) in acidic ethanol (pH = 5.5, acetic acid, 10% H_2O, and 10–20 mM ATMS), cured in a vacuum oven (70°C, 12 h), and dispersed in 1:3 ethanol:chloroform. These were then suspended on a H_2O subphase in a Langmuir Blodgett trough, compressed, and dip-coated on the substrate of interest at constant surface pressure to form hexagonally close-packed monolayers. After deposition, size reduction was performed on the silica mask using an isotropic reactive ion etch (Panasonic E460 ICP-RIE) with 40/10 sccm of CF_4/Ar at 30 mTorr, 900 W ICP power, and no sample bias. The size reduction step was followed by pattern transfer using an anisotropic plasma etch with 4/32 sccm of CH_4/H_2 at 40 mTorr and 600 V bias in a parallel plate RIE (Materials Research Corporation RIE-51) with 50°C chuck. Cleaning with O_2 plasma was done after every 25 min of CH_4/H_2 etching to remove polymer layers deposited during etching. The remaining silica mask was

removed using the same CF_4/Ar dry etch described previously, leaving behind hexagonally close-packed conical frusta on the substrate. SEM images of the final ME nanostructures are shown in Fig. 5.1. For double-side ME substrates, the aforementioned process was repeated on the backside, and no discernible damage to the frontside ME was observed. UV-vis transmission (λ = 0.3-2 μm) was measured using a Shimadzu UV3600 UV-Vis-NIR spectrometer; direct (~0.004π sr about the sample normal) and total (~1.92π sr capture from the sample back side) IR transmission of samples from λ = 2-20 μm was measured using a Bruker Equinox-55 FTIR with LN_2-cooled HgCdTe (MCT) detector and Au-coated integrating sphere.

The electromagnetic behavior of ME nanostructures was analyzed using FDTD simulations with Lumerical[31]. The simulation domain for FDTD calculations consisted of hexagonally close-packed frusta with rounded edges in the x-y plane, as depicted in Fig. 5.2(a); ±z boundaries were perfectly matched (absorbing) layers with periodic boundaries in the x- and y-directions, and the bulk substrate was modeled as 1 mm thick. Geometric parameters of the simulated ME features were set to reproduce the actual structures as determined by SEM. A plane wave source (λ = 1-20 μm) with wavevector *k* in the -z direction (blue rectangle) was set close to the upper boundary. The transmitted field was recorded with a field monitor (green rectangle) below the hexagonally close-packed frusta and bulk substrate stack, and diffractive effects at different wavelengths were evaluated using Lumerical's internal far-field intensity mapping routine. Material properties of ZnS and ZnSe were based on Lumerical-

generated fits to literature data[15,16,32] that (i) do not accurately capture the phonon absorption present above 13 μm for ZnS and 16 μm for ZnSe, and (ii) require inclusion of a finite, but small, absorption (i.e., imaginary component of dielectric constant ε" ~ 10^{-3} for ZnS and ε" ~ 10^{-4} for ZnSe), so as to fit the real parts of the respective refractive indices.

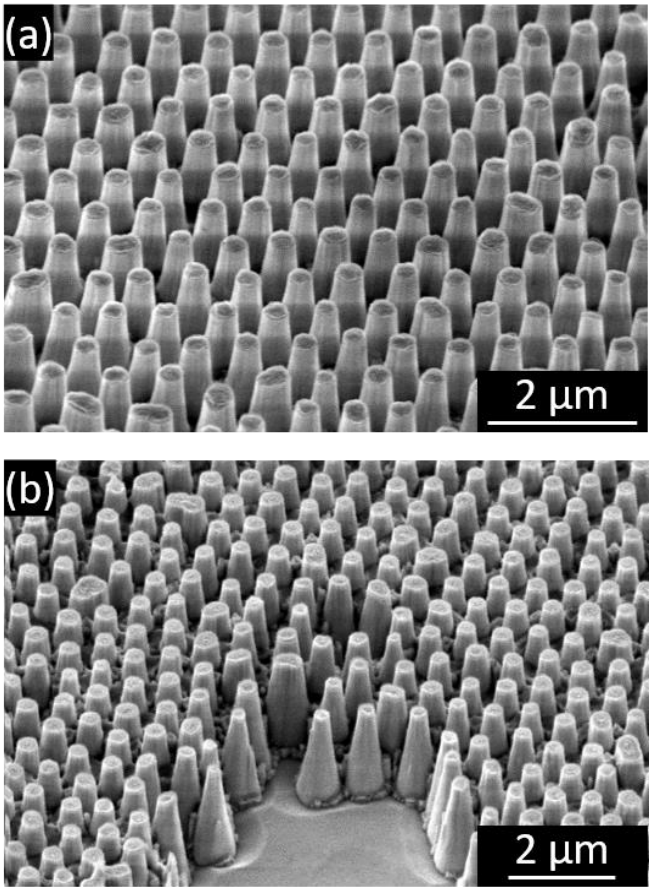

Figure 5.1: SEM images of ME nanostructures fabricated with 690 nm mask in (a) ZnS and (b) ZnSe. Reprinted with permission from IOP Publishing.

5.4 Results and discussion

ME structures on 1 mm thick bulk ZnS and ZnSe were fabricated with a mask diameter of 690 nm and an etch depth of 2.8 μm using the mask size reduction + pattern transfer process. Fig. 5.2 summarizes the measured total transmission, with comparison to FDTD predictions for the actual ME geometry. As can be seen, there is significant improvement (up to 23% and 26% near 4 μm for ZnS and ZnSe, respectively) in total transmission for ME structures compared to a flat surface in the λ = 2-20 μm range. FDTD predictions for the actual structures show considerable etaloning that is not present in the experimental data due to interference that arises from refractive index jumps at the frustum top (air-material) and base (i.e., frusta do not cover 100% of the substrate, even if hexagonally closed packed). This absence of etaloning in the experimental data is hypothesized to result from nanoscale roughness on and between frusta, as well as imperfect pattern transfer at the frusta bases, largely abolishing any 'parallel' surfaces that would otherwise lead to interference.

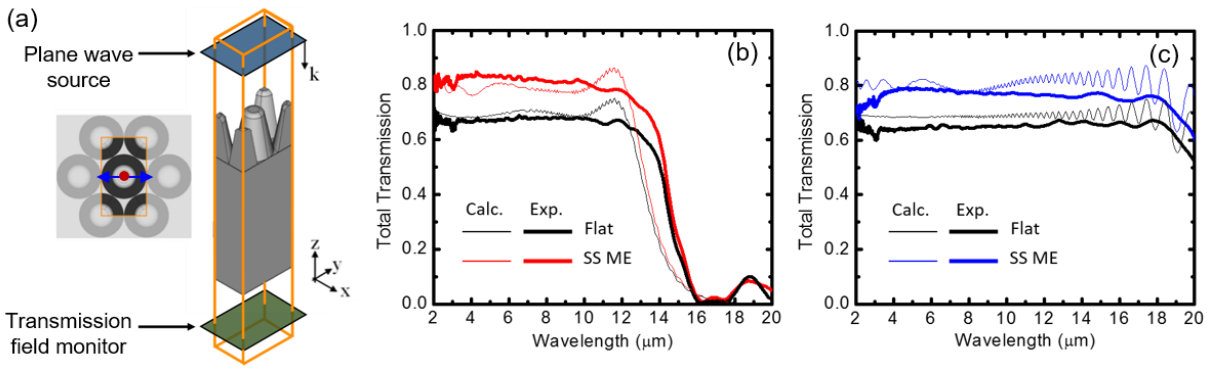

Figure 5.2: (a) FDTD model and simulation domain for moth eye structured substrates with plane wave source (blue) and transmission field monitor (green). Top down view shows unit cell with source in -z direction and polarization direction (blue arrows). Experimentally measured (thick) and FDTD-calculated (fine) total transmission of 1 mm thick bulk (b) ZnS and (c) ZnSe substrates with (color) and without (black) ME structuring on one side. ME features were fabricated using a 690 nm initial silica mask. See Results section for details. Reprinted with permission from IOP Publishing.

Total and direct transmission of double-side moth-eyed ZnS and ZnSe substrates are shown in Fig. 5.3. ME structured substrates outperform flat surfaces down to λ = 1.5 μm in total transmission, but only down to λ = 3 μm for direct transmission. The substantial drop in direct transmission in the low wavelength limit (λ = 0.3-3 μm) is attributed to three factors: (i) high-angle forward scattering due to defects in the ME structures, (ii) backscattering due to the same defects, and (iii) diffraction[33]. Based on FDTD simulations, diffraction starts to play a role below 3 μm, and the number of diffracted orders increases with decreasing wavelength as λ approaches the ME structure pitch. This effect is demonstrated more clearly in far-field intensity projections for different wavelengths (Fig. 5.4), where many diffracted orders occur at λ = 0.5 μm, and only the zeroth order (direct transmission) spot remains at λ = 10 μm.

For λ above the diffraction limit, double-sided ME structured substrates showed excellent enhancement in absolute transmission relative to their flat counterparts, peaking at 92% and 88% near λ = 4 μm for ZnS and ZnSe, respectively.

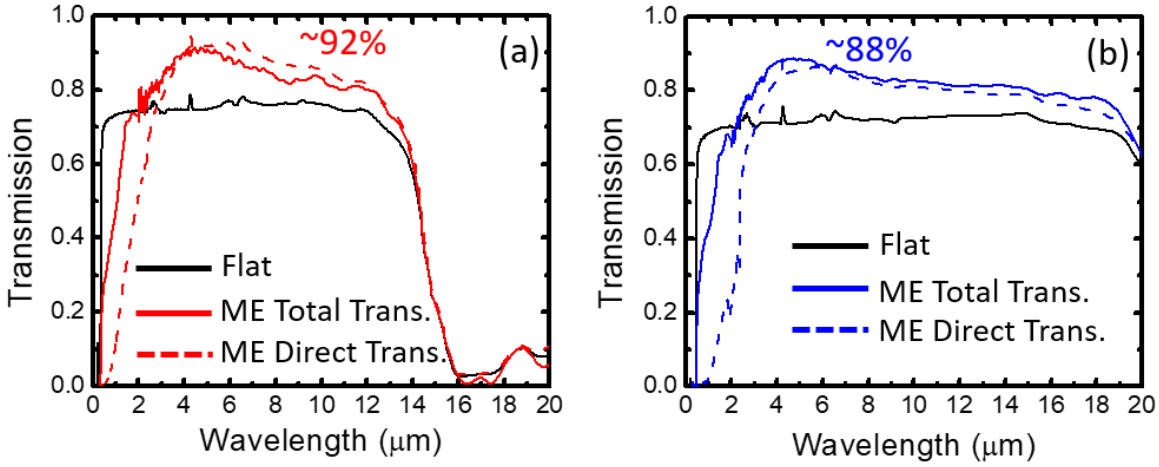

Figure 5.3: Experimentally measured total (solid) and direct (dashed) transmission of 1 mm thick bulk (a) ZnS and (b) ZnSe substrates with double-side ME structuring (color) compared to a flat substrate (black). Reprinted with permission from IOP Publishing.

FDTD polar projections of the far-field transmitted light intensity are shown in Fig. 5.4 on linear and log scales for λ = 0.5, 1, and 10 μm. In panels (a) and (d) when λ is less than the ME feature pitch, many diffraction spots (orders) can be clearly seen, exemplifying the short wavelength fall- off in direct transmission relative to total transmission seen in Fig. 5.3. The expected six-fold symmetry of an HCP lattice transmission pattern is difficult to discern in panels (a) and (b) because of preferential scattering associated with the incoming light being polarized along the short axis of the centered rectangular lattice simulation domain (cf. Fig. 5.2(a)). However,

converting to a log scale reveals a six-fold spot pattern for λ = 0.5 and 1 μm. Overall, these projections demonstrate the importance of forward scattering and diffractive effects when ME features are smaller than or on the order of the wavelength. Moreover, it is serendipitous that the present method, in which grain boundaries and defects may be present between well-organized colloidal crystal 'mosaics',' and the mask is polydisperse, produces quasi-ordered HCP-like structures that tend to wash out diffractive effects. The same is indeed true for the moth, as nature does not make perfectly ordered and monodisperse tissue protuberances on the epicorneal lamina of the eye[34].

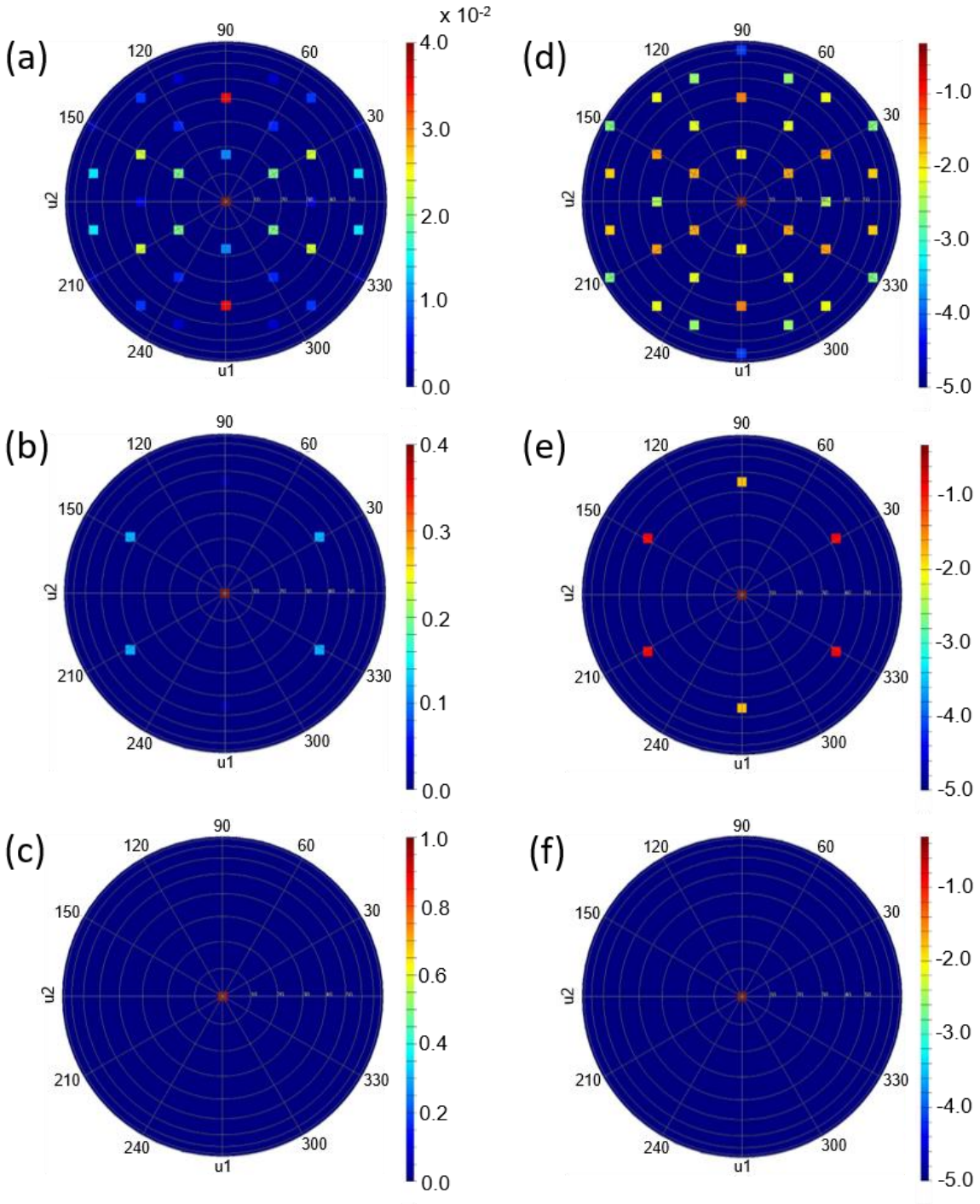

Figure 5.4: Polar projections of far-field intensity of forward scattered light through structures with 690 nm pitch, quantitatively simulated and analyzed as in Figure 5.2(a), and plotted on a linear scale (a,b,c) and a log scale (d,e,f), at λ =0.5 μm (a,d), λ =1 μm (b,e), and λ = 10 μm (c,f). Reprinted with permission from IOP Publishing.

5.5 Summary

This chapter demonstrated a simple and scalable method for fabrication of sub-wavelength scale ME surface structures in ZnS and ZnSe materials. Using nanosphere lithography, mask size reduction, and plasma-based pattern transfer, hexagonally close-packed conical frusta with adjustable geometry could be easily created to suppress surface reflections via the GRIN effect, commonly used by several moth and butterfly species to enhance light transmission at the air-eye tissue interface. Significant transmission enhancement was observed in the near and mid IR, with 23% and 26% single-side transmission improvement, and 92% and 88% absolute double-side transmission for ZnS and ZnSe, respectively. FDTD simulations, which take into account both long wavelength and near-field effects, quantitatively agreed with experimental results, and showed that diffractive losses became very important as ME feature pitch approached the wavelength. The fabrication method and ME structures presented herein can be implemented in virtually any material platform and application area to reduce reflective losses, thereby enhancing efficiency of solid state lighting components, improving transmission through electro-optic/IR optical components, and increasing signal-to-noise ratio and image contrast in IR detectors and imagers. The method described also offers advantages of scalability and relatively low cost.

5.6 References

1. Leftheriotis, G., Yianoulis, P. & Patrikios, D. Deposition and optical properties of optimised ZnS/Ag/ZnS thin films for energy saving applications. *Thin Solid Films* **306**, 92–99 (1997).

2. Kuykendall, T., Ulrich, P., Aloni, S. & Yang, P. Complete composition tunability of InGaN nanowires using a combinatorial approach. *Nat. Mater.* **6**, 951–956 (2007).

3. Shen, Q., Kobayashi, J., Diguna, L. J. & Toyoda, T. Effect of ZnS coating on the photovoltaic properties of CdSe quantum dot-sensitized solar cells. *J. Appl. Phys.* **103**, (2008).

4. Fang, X. *et al.* ZnS nanostructures: From synthesis to applications. *Prog. Mater. Sci.* **56**, 175–287 (2011).

5. Sorokina, I. T. Cr2+-doped II-VI materials for lasers and nonlinear optics. *Opt. Mater. (Amst).* **26**, 395–412 (2004).

6. Page, R. H. *et al.* Cr2+-doped zinc chalcogenides as efficient, widely tunable mid-infrared lasers. *IEEE J. Quantum Electron.* **33**, 609–617 (1997).

7. Jeon, H. *et al.* Blue and green diode lasers in ZnSe-based quantum wells. *Appl. Phys. Lett.* **60**, 2045–2047 (1992).

8. Jeon, H. *et al.* Blue-green injection laser diodes in (Zn,Cd)Se/ZnSe quantum wells. *Appl. Phys. Lett.* **59**, 3619–3621 (1991).

9. Eason, D. B. *et al.* High-brightness blue and green light-emitting diodes. *Appl. Phys. Lett.* **66**, 115–117 (1995).

10. Wagner, G. J. *et al.* Continuous-wave broadly tunable Cr2+:ZnSe laser. *Opt. Lett.* **24**, 19–21 (1999).

11. Rogalski, A. & Chrzanowski, K. Infrared devices and techniques. *Opto-Electronics Rev.* **12**, 111–136 (2002).

12. Harris, D. C. Durable 3–5 μm transmitting infrared window materials. *Infrared Phys. Technol.* **39**, 185–201 (1998).

13. Connolly, J., DiBenedetto, B. & Donadio, R. Specifications Of Raytran Material. in *Proc. SPIE* (ed. Fischer, R. E.) **0181**, 141–144 (International Society for Optics and Photonics, 1979).

14. Debenham, M. Refractive indices of zinc sulfide in the 0.405–13-μm wavelength

range. *Appl. Opt.* **23**, 2238–2239 (1984).

15. Querry, M. R. *Optical Constants of Minerals and Other Materials from the Millimeter to the Ultraviolet*. *Chemical Research, Development, & Engineering Center* (1987).

16. Marple, D. T. F. Refractive index of ZnSe, ZnTe, and CdTe. *J. Appl. Phys.* **35**, 539–542 (1964).

17. Zhang, G., Guo, L. J., Liu, Z. & Zheng, X. Application of diamond-like carbon film as protection and antireflection coatings of ZnS elements. *Opt. Eng.* **33**, 1330–1333 (1994).

18. Sankur, H. & Southwell, W. H. Broadband gradient-index antireflection coating for ZnSe. *Appl. Opt.* **23**, 2770–2773 (1984).

19. Pan, Y., Hang, L., Wu, Z. & Yin, Y. Design and fabrication of ultra broadband infrared antireflection hard coatings on ZnSe in the range from 2 to 16 um. *Infrared Phys. Technol.* **52**, 193–195 (2009).

20. Zhang, G. F., Guo, L. J., Liu, Z. T., Xiu, X. K. & Zheng, X. Studies on diamondlike carbon films for antireflection coatings of infrared optical materials. *J. Appl. Phys.* **76**, 705–707 (1994).

21. Raut, H. K., Ganesh, V. A., Nair, A. S. & Ramakrishna, S. Anti-reflective coatings: A critical, in-depth review. *Energy Environ. Sci.* **4**, 3779–3804 (2011).

22. Kaminski, P. M., Lisco, F. & Walls, J. M. Multilayer Broadband Anti-Reflective Coatings for Bulk Heterojunction Polymer Solar Cells. *IEEE J. Photovoltaics* **4**, 452–456 (2014).

23. McDaniel, S. *et al.* Cr:ZnSe laser incorporating anti-reflection microstructures exhibiting low-loss, damage-resistant lasing at near quantum limit efficiency. *Opt. Mater. Express* **4**, 2225 (2014).

24. Hobbs, D. S. & MacLeod, B. D. Design, fabrication, and measured performance of anti-reflecting surface textures in infrared transmitting materials. in *Proceedings of SPIE* **5786**, 349–364 (2005).

25. Huang, Y.-F. *et al.* Improved broadband and quasi-omnidirectional anti-reflection properties with biomimetic silicon nanostructures. *Nat. Nanotechnol.* **2**, 770–774 (2007).

26. Chattopadhyay, S. *et al.* Anti-reflecting and photonic nanostructures. *Mater. Sci. Eng. R* **69**, 1–35 (2010).

27. Wilson, S. J. & Hutley, M. C. The Optical Properties of 'Moth Eye' Antireflection Surfaces. *Opt. Acta Int. J. Opt.* **29**, 993–1009 (1982).

28. Gonzalez, F. L. & Gordon, M. J. Bio-inspired, sub-wavelength surface structures for ultra-broadband, omni-directional anti-reflection in the mid and far IR. *Opt. Express* **22**, 12808 (2014).

29. Lora Gonzalez, F., Chan, L., Berry, A., Morse, D. E. & Gordon, M. J. Simple colloidal lithography method to fabricate large-area moth-eye antireflective structures on Si, Ge, and GaAs for IR applications. *J. Vac. Sci. Technol. B* **32**, 051213 (2014).

30. Chan, L. *et al.* Fabrication and optical behavior of graded-index, moth-eye antireflective structures in CdTe. *J. Vac. Sci. Technol. B* **35**, 011201 (2017).

31. Lumerical Solutions Inc. FDTD Solutions. http://www.lumerical.com/tcad-products/fdtd/ (2017).

32. Debenham, M. Refractive indices of zinc sulfide in the 0.405–13-μm wavelength range. *Appl. Opt.* **23**, 2238–2239 (1984).

33. Gonzalez, F. L., Morse, D. E. & Gordon, M. J. Importance of diffuse scattering phenomena in moth-eye arrays for broadband infrared applications. *Opt. Lett.* **39**, 13–16 (2014).

34. Gemne, G. Ontogenesis of Corneal Surface Ultrastructure in Nocturnal Lepidoptera. *Philosophical Transactions of the Royal Society B* **262**, 343–363 (1971).

Chapter 6

Enhanced light extraction from free-standing InGaN/GaN light emitters using bio-inspired backside surface structuring

Adapted from the *Optics Express* Article:

Pynn, C.D., Chan, L., Lora Gonzalez, F., Berry, A., Hwang, D., Wu, H., Margalith, T., Morse, D.E., DenBaars, S.P., and Gordon, M.J., *Opt. Express*. **27**, 15778 (2017).

6.1 Chapter overview

Light extraction from InGaN/GaN-based multiple-quantum-well (MQW) light emitters is enhanced using a simple, scalable, and reproducible method to create hexagonally close-packed conical nano- and micro-scale features on the backside outcoupling surface of the substrate. Colloidal lithography via Langmuir-Blodgett dip-coating and plasma etching produced features with aspect ratios of 3:1 using silica masks (d = 170–2530 nm) and Cl_2/N_2-based plasma etching on devices grown on semipolar GaN substrates. InGaN/GaN MQW structures were optically pumped at 266 nm and light extraction enhancement was quantified using angle-resolved photoluminescence. A 4.8-fold overall enhancement in light extraction (9-fold at normal incidence) relative to a flat outcoupling surface was achieved using a feature pitch of 2530 nm. This performance is on par with current photoelectrochemical (PEC) nitrogen-face roughening methods, which positions the technique as a strong alternative for backside structuring of c-plane devices. Also, because colloidal lithography functions independently of GaN crystal orientation, it is applicable to semipolar and nonpolar GaN devices, for which PEC roughening is ineffective. Light scattering behavior from surface structures similar to those produced experimentally was characterized using finite-difference time-domain (FDTD) simulations. FDTD results were input as surface optical properties for ray tracing calculations to study the influence of surface structuring on light extraction efficiency. Using this approach, light extraction

enhancement which agreed reasonably well with experimental results, was calculated.

6.2 Introduction

III-nitride based light-emitting diodes (LEDs) have become a widely adopted technology for lighting and displays due to their ever-increasing luminosity and efficiency. Current R&D is focused on micro-LED devices for near-eye and mobile operation[1,2], and on improving the quality of longer wavelength (green, amber, red) emission[3,4]. Towards these goals, homoepitaxy on free-standing GaN substrates has emerged as a promising technique with potential to radically accelerate progress in the field[5]. Moving away from foreign substrates (sapphire, silicon carbide, silicon) eliminates large lattice mismatch at the substrate growth interface, improving crystal quality, and expands the design space of LEDs by enabling novel device designs and packaging schemes[6,7]. Moreover, growth on nonpolar or semipolar substrates can reduce the quantum-confined Stark effect[8] and efficiency droop[9,10], as well as enable direct polarized light emission[11–13]. Adopting this technology, however, requires reconsideration of light extraction strategies currently employed in today's LEDs.

Light extraction, largely controlled by Fresnel losses[14], is a major determinant of the overall efficiency of an LED. Large index contrast between the GaN device (n ~ 2.5) and its surroundings (air or silicone encapsulant) results in a narrow escape cone, with critical angles from 24° (air) to 38° (silicone) from normal, above which, the

majority of light is trapped by total internal reflection (TIR). Conventional sapphire-based GaN/InGaN LEDs solve the extraction problem using patterned sapphire substrates. Thin-film devices, where the substrate has been removed, typically outcouple through the nitrogen face (backside) of the device, which can be patterned using the well-known photoelectrochemical (PEC) wet etch technique[15], or by other lithographic means. An alternative approach is to pattern the gallium face (topside) of the device with graded-index (GRIN) nanopillar-, moth eye-, or photonic band gap (PBG)-like structures using optical, nanosphere, or nanoimprint lithography and subsequent etching[16–22]. For example, Choi *et al.* reported a two-fold enhancement in photoluminescence (PL) compared to a flat surface by exploiting GRIN effects and strong coupling of guided modes generated by thin-film TIR (Fig. 6.1(a)) with the nanostructured interface[18], and Matioli *et al.* reported an extraction efficiency of 94% by outcoupling through an embedded air-gap photonic crystal[21]. Although effective for photoexcited devices, topside patterning is not technologically feasible for electrically pumped LEDs because (i) a topside contact cannot easily be applied to a nano- or micro-scale patterned surface; (ii) applying a remote p-contact far away from the patterned area leads to current spreading problems[16]; (iii) etching patterns into, or close to, the active InGaN/GaN multiple-quantum-well (MQW) layer induces non-radiative defects that decrease light output[23]; and (iv) the pattern must be very shallow (i.e., the p-GaN layer above the MQWs is usually < 300 nm), limiting the aspect ratio of

GRIN features—and the types of light-matter interactions—that can be manipulated without etching into the active layer.

For homoepitaxially grown devices (i.e., when the native substrate is retained), the utility of topside patterning is further diminished by weak coupling of guided modes—now delocalized across hundreds of microns into the substrate—with the structured interface (Fig. 6.1(b)). These devices must therefore rely on surface roughening and chip shaping to randomize light trajectories and break the TIR condition[7]. While PEC etching is a candidate for structuring these devices, it suffers from reproducibility issues[24], pattern geometry cannot be freely optimized, and it is known to attack essential fabrication components such as metal contacts, backside reflecting layers, and mounting wax. Furthermore, PEC roughening is highly selective to the nitrogen-polar c-plane and does not work with semipolar and nonpolar device orientations[25,26]. Other backside surface roughening techniques, involving contact lithography plus dry etching[27], have been proposed for semipolar LEDs, but these methods introduce significant additional process complexity and cost, as well as reproducibility and scaling issues.

In this chapter, we demonstrate high efficiency light extraction (4.8-fold total enhancement and up to 9-fold at normal incidence, relative to a flat surface) from InGaN/GaN MQW structures grown on semipolar GaN substrates with moth eye-like backside surface structuring produced by a facile and scalable Langmuir-Blodgett (LB) colloidal lithography process. The resulting PL enhancement is comparable to that

obtained in polar GaN devices roughened by state-of-the-art PEC etching, and understanding of the light extraction mechanism is supported by mixed-level optical simulations. We optimize this enhancement through systematic performance analysis of structuring across multiple length scales, including the graded-index, near-field, and refraction-limited regimes, made possible by modifying the backside outcoupling interface of the device. Because of its simplicity, range of optical control, and wide substrate compatibility, the colloidal lithography technique is a viable alternative to existing commercial processes and a future pathway for enhanced extraction engineering in free-standing polar, nonpolar, and semipolar III-nitride LEDs.

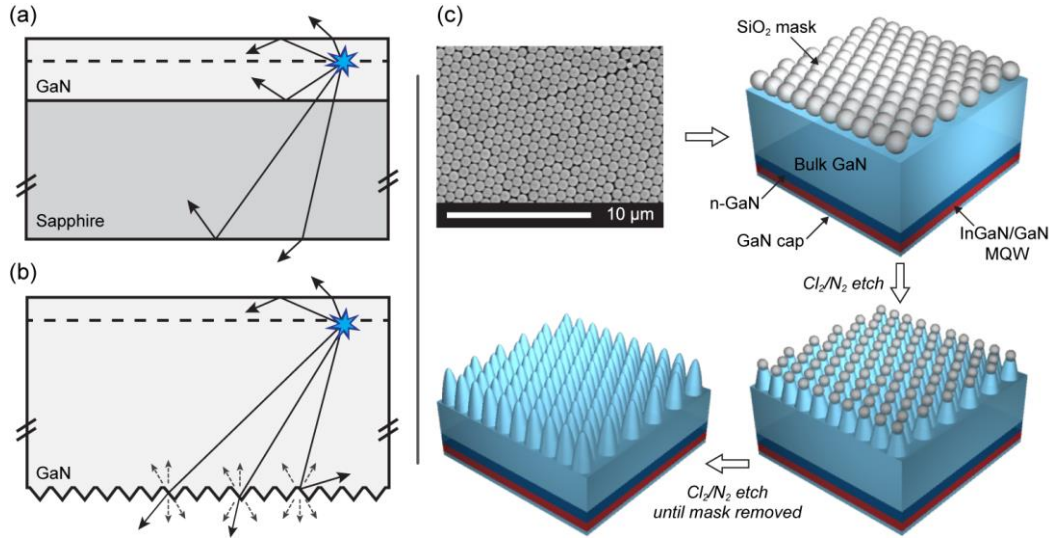

Figure 6.1: Schematic view of light rays propagating through (a) a thin-film sapphire/GaN LED and (b) a backside micro-structured free-standing GaN/GaN LED. In (a), thin-film TIR creates guided modes strongly coupled to the device topside. In (b), TIR modes are delocalized throughout the bulk chip, and backside outcoupling causes forward and reverse specular and diffuse (dashed) scattering. (c) SEM image of silica colloidal crystal mask and process flow to create moth eye-like features on the backside outcoupling surface of the LED chip. Reprinted with permission from OSA Publishing.

6.3 Experimental methods

GaN/InGaN samples were homoepitaxially grown by atmospheric pressure metal organic chemical vapor deposition (MOCVD) on free-standing semipolar $(20\bar{2}1)$ and *c*-plane GaN substrates (Mitsubishi Chemical Company (MCC) and Sciocs Company Limited, respectively). Epitaxial structures consisted of a 1 μm n-type GaN:Si layer, an undoped InGaN/GaN five-period MQW active region, and a 30 nm undoped GaN capping layer. The back surface of each sample was polished using 3 μm polycrystalline diamond slurry to an optically smooth finish.

Silica colloids (d = 170, 310, 960, 2530 nm; Bangs Laboratories, synthesized using a modified, semi-batch Stöber process) were functionalized with allyltrimethoxysilane (ATMS, Sigma-Aldrich, >98%) in acidic ethanol, cured overnight in a vacuum oven (343 K, 8 h), and redispersed in 1:3 ethanol:chloroform. The colloidal mask was then deposited on the polished back surface of the sample by a Langmuir-Blodgett dip-coating process described elsewhere[28], leaving behind a hexagonally close-packed monolayer of silica spheres (Fig. 6.1(c)). The masked samples were then dry etched in an inductively coupled plasma reactive ion etcher (ICP-RIE, Panasonic E640) using Cl_2/N_2 (22.5/7.5 sccm) with 500 W ICP power and 300 W bias at 0.2 Pa, with the colloidal layer acting as a hard mask. The duration of the dry etch was scaled with the diameter of the silica colloids such that etching proceeded until the masks were fully removed; vertical GaN structures with angled sidewalls resulted due to shrinking of the mask during Cl_2/N_2 etching (Fig. 6.1(c)). For comparison, *c*-plane samples were also grown

and polished to the same specification as previously described, then roughened using a PEC wet etch. Samples were immersed in 2.2 M KOH and illuminated using a mercury arc lamp (750 W) for 15 minutes.

Angle-resolved, far-field PL spectra were collected at room temperature two times for each sample: first, with an optically smooth backside, and second, with a roughened backside. A 266 nm Q-switched Nd:YAG pulsed laser (1 mm spot size) was used to optically excite the quantum wells (through the GaN capping layer) at 8° incidence from the sample normal as the sample was rotated (azimuthally) about its normal at 3 Hz. Since the excitation source energy was well above the bandgap of GaN, pump light was fully absorbed in the first pass through the sample, eliminating any pump light recycling effects due to reflection. PL emission was collected at various angles (θ) from 0° to 90° in 2° increments with a 1 mm core optical fiber mounted to an optical goniometer system; light from the fiber was then directed to a UV-Vis spectrometer (Ocean Optics USB2000+) to record a full PL spectrum at each angle. The spectral intensity (I) of each angular (θ) scan was integrated from λ = 375–550 nm for each of the structured and unstructured (or polished) cases. An angle-resolved enhancement factor *EF(θ)* was calculated for each sample by comparing the structured $I_s(\theta)$ and unstructured $I_p(\theta)$ (polished) integrated intensities: $EF(\theta) = I_s(\theta) / I_p(\theta)$.

6.4 Experimental results and discussion

SEM images of the plasma-etched surface structures in GaN are presented in Figs. 6.2(a)–(c). The sidewall angle of conical features was controlled primarily by the etch selectivity of GaN to SiO_2. As the hard mask was etched, more of the underlying GaN substrate was exposed and subjected to the dry etch, creating a semi-periodic, two-dimensional array of hexagonally close-packed conical structures with aspect ratios of ~3:1. The chosen etch chemistry gave an etch selectivity of 6:1 GaN:SiO_2 and a sidewall angle of approximately 75°. To emphasize the topography that was obtained, the images in Figs. 6.2(a)–(c) were recorded from areas of limited structured surface coverage near the edge of each sample. Effectively the entire sample showed good surface coverage and pattern uniformity. Defects in the pattern were predominantly grain boundaries between rotated colloidal crystal 'mosaics', which are in fact beneficial for light extraction, as they act as additional scattering sites to aid in breaking the TIR condition.

Figure 6.2(d) shows PEC wet etching results on the nitrogen face of a *c*-plane GaN sample. The crystallographic pyramids formed were bounded by stable $\{10\bar{1}\bar{1}\}$ facets of the GaN crystal, having a sidewall angle of ~45° and a base diameter from 2–5 μm[29]. In general, the reproducibility of this etch technique could not be well controlled. Various surface pre-treatments were level before an acceptable amount of surface coverage and feature uniformity could be achieved, but subsequent trials using identical conditions often yielded a range of pyramid sizes and coverage.

Furthermore, while the surface coverage of pyramids using PEC was acceptable, it could not match the 100% coverage achieved with colloidal lithography.

Representative angle-resolved, integrated PL data (d = 170 nm, 2530 nm) for the polished and structured InGaN/GaN samples are given in Fig. 6.3(a), with the extraction enhancement factor for each surface structure given in Fig. 6.3(b). The extraction enhancement for samples patterned by colloidal lithography improved as the feature pitch increased from 170 nm to 2530 nm. This trend is explained by considering the prevailing scattering physics for each case. For an unstructured interface, the majority of light incident beyond the escape cone ($\theta > \theta_{crit}$) is specularly reflected back into the chip. This creates guided modes that are eventually absorbed by high-index material. For a structured interface, scattering mechanisms emerge that disrupt these guided modes, break TIR, and therefore improve the extraction efficiency of the device.

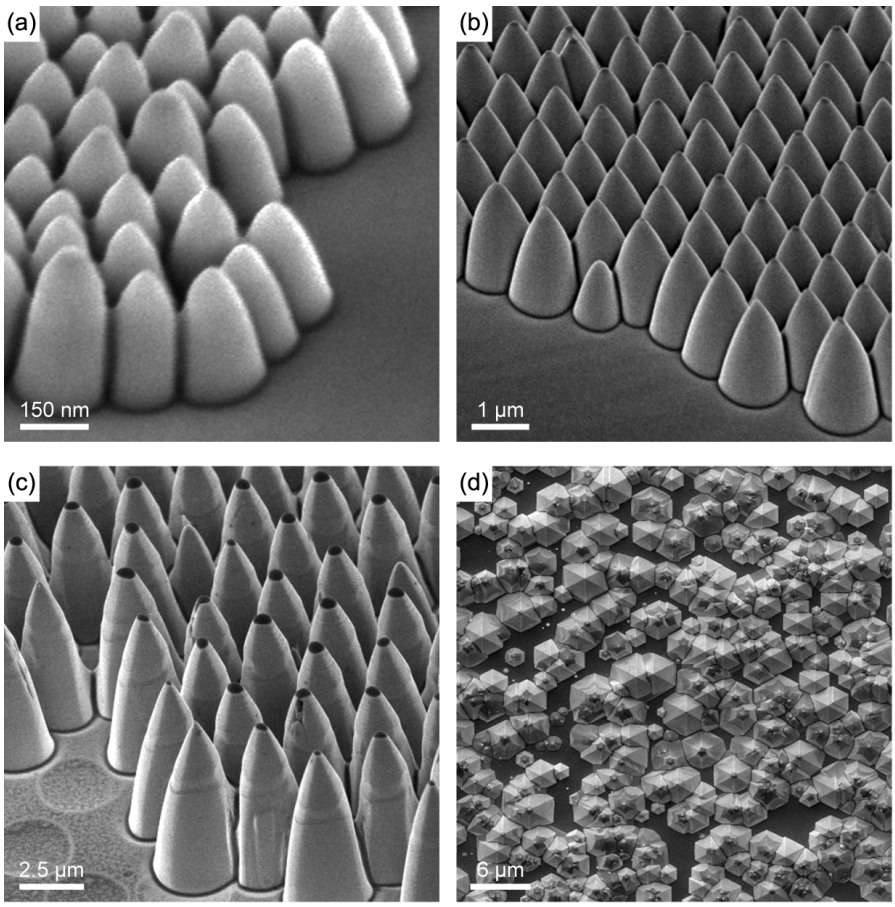

Figure 6.2: (a-c) SEM images of moth eye-like surface structures in GaN realized using colloidal lithography via Langmuir-Blodgett dip-coating and plasma dry etching; initial silica mask sizes were (a) 170 nm, (b) 960 nm, and (c) 2530 nm. (d) SEM image of nitrogen-face wet etching of c-plane GaN using photoelectrochemical (PEC) etching with KOH. Reprinted with permission from OSA Publishing.

Comparison of the structured far-field PL for d = 170 and 2530 nm masks with an ideal Lambertian diffuser (Fig 6.3(a)) indicates that the scattering strength of the interface depends strongly on the interface geometry. For structures where $d / \lambda >> 1$, specular and diffuse scattering occur, significantly improving extraction of light outside the escape cone. Diffractive effects from the two-dimensional, semi-periodic surface grating also emerge at this length scale, although this enhancement is

secondary. For $d / \lambda \sim 1$, the scattering strength of the interface decreases and diffractive effects are eliminated, thereby decreasing the transmission of incident light beyond the escape cone. For $d / \lambda << 1$, the scattering strength approaches that of a planar interface, and Fresnel optics dominate. While specular reflections for TIR are largely conserved, diffuse scattering processes enhance extraction relative to the unstructured case. Additionally, in this long-wavelength limit, the surface structuring creates a graded index (GRIN) of refraction (i.e., the moth eye effect[30]), which greatly reduces Fresnel loss at the interface. Because TIR is preserved by the absence of scattering phenomenon, the GRIN interface is only effective at increasing transmission of guided modes incident within the escape cone. Surface structuring at this length scale, in general, has limited utility for isotropic emitters such as nitride LEDs.

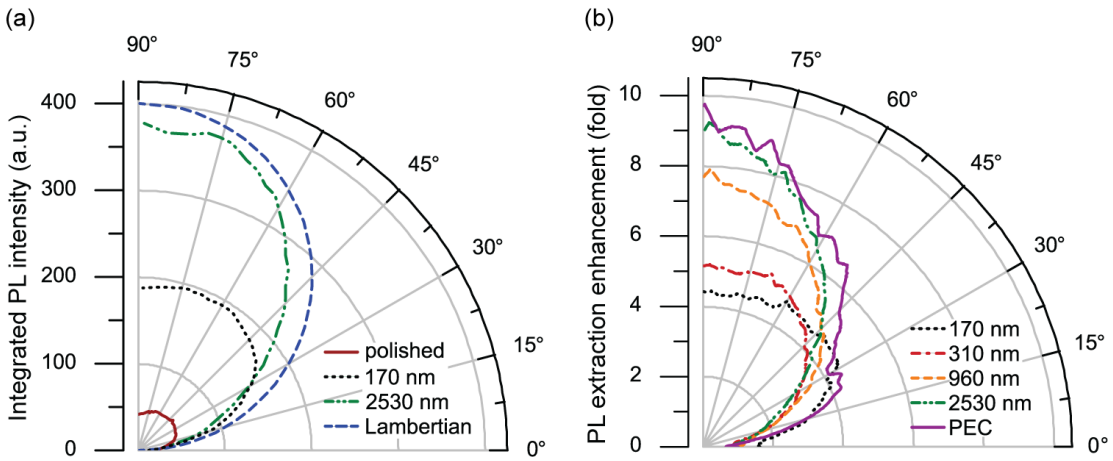

Figure 6.3: (a) Polar plot of integrated (λ = 375-550 nm) total PL emission from five-period InGaN/GaN multiple-quantum well (MQW) structures on GaN substrates roughened using 170 nm and 2530 nm silica colloids. Integrated PL emission for a polished reference surface and for an ideal Lambertian diffuser are also shown for comparison. (b) Polar plot of enhancement in PL extraction from MQW devices with roughened GaN-air interfaces, normalized by the emission from a flat GaN device surface. MQWs were excited using 266 nm light at 8° incidence from normal, and curve annotations represent the initial silica colloid size (d = 170, 310, 960, 2530 nm) used as the etch mask. Reprinted with permission from OSA Publishing.

The PEC etched sample had the highest overall extraction enhancement of all structures explored, although the largest colloidal structuring (d = 2530 nm) exhibited near-comparable performance. The effectiveness of these largest features relative to smaller ones underscores the advantage of backside over topside roughening for electrically pumped devices. Patterns in the refractive limit (d >> λ) are possible only on the backside of the device, where there is freedom to form microscale features without compromising electrical and optical performance. In contrast, the topside outcoupling surface is limited laterally by the requirement to form a large-area *p*-contact and vertically by epitaxial proximity of the active layers to the chip surface.

Additionally, the trend in how size affects performance further demonstrates the ineffectiveness of evanescent coupling techniques—such as those commonly implemented on the topside of thin-film LEDs—for non-thin-film LEDs, since guided modes overlap weakly with the outcoupling interface. These observations call for continued exploration of the design space of colloidal structuring, including optimization of sidewall angle through modification of etch parameters and extension to larger silica masks. Further investigation is expected to yield structures that match or exceed the performance of state-of-the-art PEC roughening, the latter being ineffective on semipolar GaN-based devices.

6.5 Mixed-level optical simulations to predict light extraction

Experimental results showed significant light extraction enhancement (~9-fold enhancement at normal and ~5-fold total enhancement for largest features) by roughening the light outcoupling surface of GaN/InGaN light emitters using ME patterning. However, studying and predicting the light extraction from nanostructured LED chips using FDTD alone is difficult over larger device scales. Optical simulations for predicting the influence of surface nanostructures on light extraction efficiency requires fundamental studies of light-matter interactions over multiple length scales. The technique used in this work for modelling light-matter interactions over multiple structure length scales is called “mixed-level” optical simulations[31,32] which combines FDTD to predict of electromagnetic wave interactions

with features on the order of or smaller than the wavelength, with ray tracing which takes a geometric optics approach to track light propagation through structures that are much larger than the wavelength.

The angular profiles of light scattered from nanostructured GaN surfaces as well as reflected and transmitted intensity for different angles of incidence were produced using FDTD simulations with Lumerical[33]. The simulation domain for FDTD calculations consisted of hexagonally close-packed frusta on a slab, where the material for all structures was GaN in an air medium, as shown in the schematic in Figure 6.4(a). The ±z boundaries were perfectly matched (absorbing) layers with Bloch boundaries in the x- and y-directions. Geometric parameters of the simulated ME features were set to reproduce the actual structures as determined by SEM. A monochromatic (λ = 450 nm) plane-wave source with wavevector k swept from the 0-70° (+z direction normal) was set in the GaN slab.

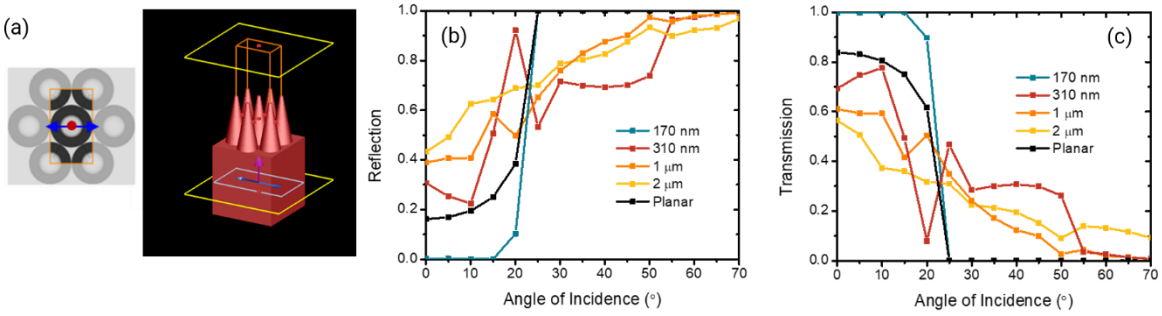

Figure 6.4: (a) Schematic of FDTD simulation set-up, where a plane-wave source is placed in a GaN slab and pointed in the +z direction and the surface nanostructures are modeled as hexagonally close-packed cones. FDTD was used to calculate (b) reflection and (c) transmission for planar GaN and ME structured GaN (d = 170 nm, 310 nm, 1000 nm, and 2530 nm) at λ = 450 nm.

The transmitted and reflected fields were recorded with field monitors above and below the hexagonally close-packed frusta, and angular profiles were evaluated using Lumerical's internal far-field intensity mapping routine. Monte Carlo ray tracing calculations were done in LightTools[34], and consisted of a simple 3D GaN chip, a planar surface source embedded in the chip, where rays were generated and propagated in random directions, and a far-field spherical receiver which fully enclosed the model. Far-field scattering intensity maps generated using FDTD were input to LightTools to define the outcoupling surface optical properties. The extraction efficiency was defined as the ratio of the number of rays collected by the receiver in the outcoupling direction (hemisphere centered over outcoupling surface) to the total number of rays emitted.

The FDTD-calculated reflection and transmission versus angle of incidence in Figure 6.4(b,c) confirm a critical angle ~23° at the GaN-air interface, as shown by the steep increase and decrease of reflection and transmission, respectively, for the planar GaN case, between 20° to 25°. The calculation also reveals that the critical angle is still relevant for the smallest ME structures (d = 170 nm). As mentioned in the previous section, structures where $d / \lambda << 1$ eliminate reflection via the GRIN effect. However, because of the absence of scattering, TIR is preserved and thus the GRIN interface is only effective at improving light extraction within the escape cone.

Far-field scattering intensity maps from Lumerical were input as surface optical properties for subsequent raytracing calculations. Scattering profiles of light reflected

from structures (field monitor in GaN slab below ME structures) with an angle of incidence of 0° and λ = 450, for various sized structures are shown in Figure 6.5. These scattering profiles show that the largest structures resulted in the most scattering of light at λ = 450 nm, as expected. While not shown here, this is true for all angles of incidence. This supports the claim that the largest ME structures resulted in the best experimental light extraction enhancement by improving extraction of light outside the escape cone through randomization of light trajectories from the structured surface, and so, break the TIR condition. Light extraction calculated with raytracing, where FDTD scattering profiles were used to define surface optical properties, are summarized in Table 6.1. The light extraction, total enhancement in 2πsr, and enhancement at normal agree reasonably well with experimental results, which showed better light extraction enhancement with increasing structure size.

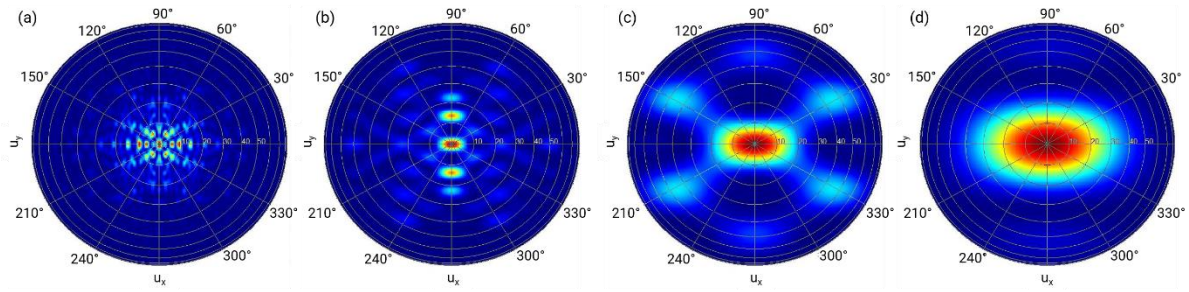

Figure 6.5: Far-field scattering profiles from reflection monitor for structures that have pitch of (a) 2530 nm, (b) 1000 nm, (c) 310 nm, and (d) 170 nm. The degree of scattering increases with increasing structure size.

	Calculated			Experimental	
	Light extraction	**Total enhancement**	**Enhancement at normal**	**Total enhancement**	**Enhancement at normal**
Planar	10.9%	-	-	-	-
2.5 μm	36.9%	3.4x	9.7x	5.0x	9.0x
1 μm	34.6%	3.2x	6.5x	4.8x	7.8x
310 nm	24.1%	2.2x	4.7x	3.8x	5.2x

Table 6.1: Light extraction, total enhancement in 2πsr, and enhancement at normal for planar LEDs and nanostructured LEDs with structure pitch of 2.5 μm, 1 μm, and 310 nm.

6.6 Summary

In this chapter, nanostructuring to improve light extraction from III-nitride light-emitting structures was demonstrated. Using a facile approach for creating nano- and micro-structured backside surfaces enhanced outcoupling by breaking the TIR condition via increased diffuse scattering and diffractive effects, was achieved. Colloidal lithography with Langmuir-Blodgett deposition and plasma etching, provide geometry tunability across multiple length scales and provides high reproducibility and surface coverage. Utilization of the device backside as the primary outcoupling interface presents a technologically feasible approach to fabricate electrically pumped devices, by avoiding the complications presented by topside patterning. An overall PL extraction enhancement of 4.8-fold (angular average), with peak extraction enhancement of 9-fold at normal incidence, was shown using a 2530 nm surface

structure pitch. This improvement was comparable to the enhancement observed using state-of-the-art PEC etching on *c*-plane GaN, a technique that is incompatible with most GaN crystal orientations. Colloidal lithography, therefore, is a simple, tunable alternative to current PEC etching on *c*-plane devices and an enabling backside surface structuring technology for future nonpolar and semipolar free-standing GaN devices. Experimental results were also supported by mixed-level simulations which predicted the light extraction efficiency for different size surface structuring. These simulations used FDTD to calculate far-field scattering profiles from various sizes of nano- and microstructures and Monte-Carlo raytracing to predict the light extraction from an LED chip. The results showed that despite better transmission within the escape cone for 310 nm surface structuring, the largest 2530 nm structures provided the best light extraction enhancement due to enhanced scattering that randomizes light trajectories and breaks the TIR condition.

6.7 References

1. Day, J. *et al.* III-Nitride full-scale high-resolution microdisplays. *Appl. Phys. Lett.* **99**, 031116 (2011).

2. Lingley, A. R. *et al.* A single-pixel wireless contact lens display. *J. Micromechanics Microengineering* **21**, 125014 (2011).

3. Alhassan, A. I. *et al.* High luminous efficacy green light-emitting diodes with AlGaN cap layer. *Opt. Express* **24**, 17868 (2016).

4. Hwang, J. Il, Hashimoto, R., Saito, S. & Nunoue, S. Development of InGaN-based red LED grown on (0001) polar surface. *Appl. Phys. Express* 7, 071003 (2014).

5. Cich, M. J. *et al.* Bulk GaN based violet light-emitting diodes with high efficiency at very high current density. *Appl. Phys. Lett.* **101**, 223509 (2012).

6. Hwang, D. *et al.* Photoelectrochemical liftoff of LEDs grown on freestanding c-plane GaN substrates. *Opt. Express* **24**, 22875–22880 (2016).

7. Hurni, C. A. *et al.* Bulk GaN flip-chip violet light-emitting diodes with optimized efficiency for high-power operation. *Appl. Phys. Lett.* **106**, 031101 (2015).

8. Chichibu, S., Azuhata, T., Sota, T. & Nakamura, S. Spontaneous emission of localized excitons in InGaN single and multiquantum well structures. *Appl. Phys. Lett.* **69**, 4188–4190 (1996).

9. Becerra, D. L. *et al.* High-power low-droop violet semipolar ($30\bar{3}\bar{1}$) InGaN/GaN light-emitting diodes with thick active layer design. *Appl. Phys. Lett.* **105**, 171106 (2014).

10. Oh, S. H. *et al.* Semipolar III–nitride light-emitting diodes with negligible efficiency droop up to ~1 W. *Appl. Phys. Express* **9**, 102102 (2016).

11. Koslow, I. L. *et al.* Performance and polarization effects in (1122) diodes grown on stress relaxed InGaN buffer layers. *Appl. Phys. Lett.* **101**, 121106 (2012).

12. Matioli, E. *et al.* High-brightness polarized light-emitting diodes. *Light Sci. Appl.* **1**, e22 (2012).

13. Kowsz, S. J. *et al.* Demonstration of phosphor-free polarized white light emission from monolithically integrated semipolar InGaN quantum wells. *Appl. Phys. Lett.* **107**, 101104 (2015).

14. David, A. Surface-Roughened Light-Emitting Diodes: An Accurate Model. *J. Disp. Technol.* **9**, 301–316 (2013).

15. Fujii, T. *et al.* Increase in the extraction efficiency of GaN-based light-emitting diodes via surface roughening. *Appl. Phys. Lett.* **84**, 855–857 (2004).

16. Hsieh, M. Y., Wang, C. Y., Chen, L. Y., Ke, M. Y. & Huang, J. J. InGaN-GaN nanorod light emitting arrays fabricated by silica nanomasks. *IEEE J. Quantum Electron.* **44**, 468–472 (2008).

17. Ng, W. N., Leung, C. H., Lai, P. T. & Choi, H. W. Nanostructuring GaN using microsphere lithography. *J. Vac. Sci. Technol. B Microelectron. Nanom. Struct.* **26**, 76–79 (2008).

18. Fu, W. Y., Wong, K. K. Y. & Choi, H. W. Close-packed hemiellipsoid arrays: A

photonic band gap structure patterned by nanosphere lithography. *Appl. Phys. Lett.* **95**, (2009).

19. Ee, Y. K. *et al.* Optimization of light extraction efficiency of III-nitride LEDs with self-assembled colloidal-based microlenses. *IEEE J. Sel. Top. Quantum Electron.* **15**, 1218–1225 (2009).

20. Truong, T. A. *et al.* Light extraction from GaN-based light emitting diode structures with a noninvasive two-dimensional photonic crystal Light extraction from GaN-based light emitting diode structures with a noninvasive two-dimensional photonic crystal. **94**, 023101 (2009).

21. Matioli, E. *et al.* High extraction efficiency light-emitting diodes based on embedded air-gap photonic-crystals. *Appl. Phys. Lett.* **96**, 2008–2011 (2010).

22. Lai, F.-I. & Yang, J.-F. Enhancement of light output power of GaN-based light-emitting diodes with photonic quasi-crystal patterned on p-GaN surface and n-side sidewall roughing. *Nanoscale Res. Lett.* **8**, 244 (2013).

23. Nedy, J. G. *et al.* Low damage dry etch for III-nitride light emitters. *Semicond. Sci. Technol.* **30**, 085019 (2015).

24. Jeong, T. *et al.* Light output improvement of 10 W operated vertical LEDs via surface roughening using a commercialized developer. *J. Mater. Sci. Mater. Electron.* **26**, 3397–3402 (2015).

25. Zhong, H. *et al.* Enhancing the Light Extraction Efficiency of Blue Semipolar ($10\bar{1}\bar{1}$) Nitride-Based Light Emitting Diodes through Surface Patterning. *Jpn. J. Appl. Phys.* **48**, 030201 (2009).

26. Jung, S., Song, K.-R., Lee, S.-N. & Kim, H. Wet chemical etching of semipolar GaN planes to obtain brighter and cost-competitive light emitters. *Adv. Mater.* **25**, 4470–4476 (2013).

27. Zhao, Y. *et al.* 30-mW-Class High-Power and High-Efficiency Blue Semipolar (10\bar1\bar1) InGaN/GaN Light-Emitting Diodes Obtained by Backside Roughening Technique. *Appl. Phys. Express* **3**, 102101 (2010).

28. Lora Gonzalez, F., Chan, L., Berry, A., Morse, D. E. & Gordon, M. J. Simple colloidal lithography method to fabricate large-area moth-eye antireflective structures on Si, Ge, and GaAs for IR applications. *J. Vac. Sci. Technol. B* **32**, 051213 (2014).

29. Gao, Y. *et al.* Roughening Hexagonal Surface Morphology on Laser Lift-Off (LLO) N-Face GaN with Simple Photo-Enhanced Chemical Wet Etching. *Jpn. J. Appl.*

Phys. **43**, L637–L639 (2004).

30. Gonzalez, F. L., Morse, D. E. & Gordon, M. J. Importance of diffuse scattering phenomena in moth-eye arrays for broadband infrared applications. *Opt. Lett.* **39**, 13–16 (2014).

31. Bahl, M. *et al.* Optical simulations of organic light-emitting diodes through a combination of rigorous electromagnetic solvers and Monte Carlo ray-tracing methods. *Proc. SPIE* **9190**, (2014).

32. Bahl, M. *et al.* Mixed-level optical simulations of light-emitting diodes based on a combination of rigorous electromagnetic solvers and Monte Carlo ray-tracing methods. *Opt. Eng.* **54**, 045105 (2015).

33. Lumerical Solutions Inc. FDTD Solutions. http://www.lumerical.com/tcad-products/fdtd/ (2017).

34. Synopsis. LightTools. https://www.synopsys.com/optical-solutions/lightto (2020).

Chapter 7

Fabrication and chemical lift-off of nanoscale III-nitride light emitters

Adapted from the Article:

Chan, L., Karmstrand, T., Shapturenka, P., Chan, A., Hwang, D., Margalith, T., DenBaars, S.P., Gordon, M.J., "Fabrication and chemical lift-off of nanoscale III-nitride light emitters," In Preparation.

7.1 Chapter overview

Nanoscale light emitting diodes (nanoLEDs), with active and sacrificial multi-quantum well (MQW) layers epitaxially grown using metal organic chemical vapor deposition (MOCVD), were fabricated and released into solution using a combination of colloidal lithography and photoelectrochemical (PEC) etching of the sacrificial MQW layer. The PEC etch was optimized to minimize undercut roughness, and thus limit the damage to the active MQW layers, at a KOH etchant concentration of 0.02 M. nanoLEDs were optically characterized using photoluminescence (PL) measurements, which showed disappearance of the sacrificial MQW emission and a 12 nm blue-shift in emission from the active MQW compared to a planar, as-grown LED. The large wavelength shift is thought to be due to strain relaxation in the InGaN layer that would result in less quantum confined Stark effect (QCSE) and an increase in internal quantum efficiency (IQE). X-ray diffraction (XRD) reciprocal space mapping (RSM) was employed to assess strain relaxation due to nanopatterning, and showed ~15% reduction in strain for nanoLEDs with diameter ~500 nm. This work suggests that colloidal lithography, combined with chemical release, is a viable route to produce solution processable, high efficiency nanoscale light emitters.

7.2 Introduction

Flexible, transparent, near-eye, and high density display technologies for next generation mobile and wearable electronics will require efficient micro- and

nanoscale self-emissive pixels, i.e., pixels made up of devices that emit light, rather than color convert a white light emitting back-plane. With the development of III-nitride microscale light emitting diodes (LEDs), or microLEDs[1–3], GaN/InGaN devices have shown promise in these applications due to their high efficiency and luminance. Currently, organic LEDs (OLEDs) are being used or are envisioned for these proposed display technologies due to their low-cost and scalable manufacturing. However, OLEDs suffer from low efficiency and lifetimes[4,5]. Higher efficiency III-nitride LEDs could potentially solve these issues, but scalable fabrication of micron and sub-micron scale GaN/InGaN devices that emit at different wavelengths, and implementing such devices onto display platforms is challenging. Substrate thinning and/or separating individual devices from their rigid growth substrates for subsequent high-throughput printing onto alternate substrates is also required for flexible and transparent display applications.

High density and transparent displays require small pixels (<100 μm for TV monitors, <50 μm for watches and smartphones, <5 μm for augmented reality/virtual reality (AR/VR))[6] for both visual and cost constraints. For instance, large devices are not compatible with near-eye displays and require higher material cost, compared to small devices. Additionally, sub-micron patterning can increase the internal quantum efficiency (IQE) of the device by reducing quantum confined Stark effects (QCSE)[7]. Scalable nanopatterning can relax strain and is thus needed to fabricate sub-micron scale LEDs. Colloidal lithography combined with plasma etching is a potential solution

to scalable, cost-effective, and reproducible nanopatterning[8,9], that has been implemented in the III-nitride material system to nanopattern outcoupling surfaces to enhance light extraction from semipolar InGaN/GaN LEDs[10] and to fabricate nanorod LEDs, where an individual LED is composed of nanorods[11–13]. Researchers have also used colloidal lithography to produce individual, optically-active nanoscale devices, suspended them in solution, and used dielectrophoresis to align them onto metal electrodes for electroluminescence[14,15]. In the latter case, devices were physically removed from the sapphire growth substrate using a diamond blade, a process step that is not necessarily scalable.

Separation of GaN devices from their growth substrates has also been demonstrated using laser lift-off[16–19], selective etching of the growth substrate itself (GaN on Si)[20], or selective etching of a sacrificial material (BN[21,22], CrN[23], ZnO[24–26], Si doped n-GaN[27], InGaN[28]) between the growth substrate and the device. Of these methods, selective etching of a sacrificial layer is of particular interest because it does not depend on the material and etch selectivity of the growth substrate. Furthermore, using InGaN as the sacrificial layer is a simple approach, as conventional LEDs already employ InGaN in multi-quantum well (MQW) light emitting layers. Hwang *et al.* demonstrated chemical lift-off of microLEDs grown on sapphire using photoelectrochemical (PEC) etching of a sacrificial InGaN/GaN MQW[29,30].

In this work, we have developed a fabrication method to produce submicron scale c-plane LEDs (diameter = 500 nm, height = 1.5 μm), or nanoscale LEDs (nanoLEDs),

that combines colloidal lithography with selective PEC undercut etching to separate nanoLEDs from a sapphire growth substrate. PEC etching conditions were optimized for minimal undercut surface roughness to mitigate damage to the active light emitting MQWs. By combining these methods, a wafer-scale, hexagonally close-packed (HCP) array of GaN/InGaN nanoLEDs was fabricated and released into solution for potential high-throughput solution-based assembly. These devices address the aforementioned manufacturing challenges because they satisfy the small pixel dimension requirement, can be separated from their rigid growth substrates, and can potentially be assembled onto display platforms, all using low-cost and scalable methods.

7.3 Experimental methods

GaN/InGaN LEDs (2 μm n-GaN buffer, undoped sacrificial six-period MQWs with 2.5 nm InGaN QWs and 7 nm GaN barriers, 1.5 μm n-GaN layer, undoped active six-period MQWs with 2.5 nm InGaN QWs and 7 nm GaN barriers, and 100 nm p-GaN layer) were epitaxially grown by metal organic chemical vapor deposition (MOCVD) on sapphire. A schematic of the device fabrication procedure and SEM micrographs at various process steps are presented in Figure 7.1. Colloidal lithography was used to define HCP arrays of nanoLEDs. Silica colloids (d = 960 nm) were functionalized with allyltrimethoxysilane (ATMS, Sigma-Aldrich, >98%) in ethanol (pH = 5.5, acetic acid, 10% H_2O, and 10-20 mM ATMS)[31–33]. The colloids were washed in ethanol after

functionalization, cured in a vacuum oven (65°C, 12 hours), and redispersed in 3:1 chloroform:ethanol. The functionalized colloids were then suspended in a Langmuir-Blodgett trough (KSV Nima) on a H_2O subphase and compressed by a barrier. Epitaxial GaN/InGaN device substrates were then dip-coated, leaving behind a HCP monolayer of silica colloids.

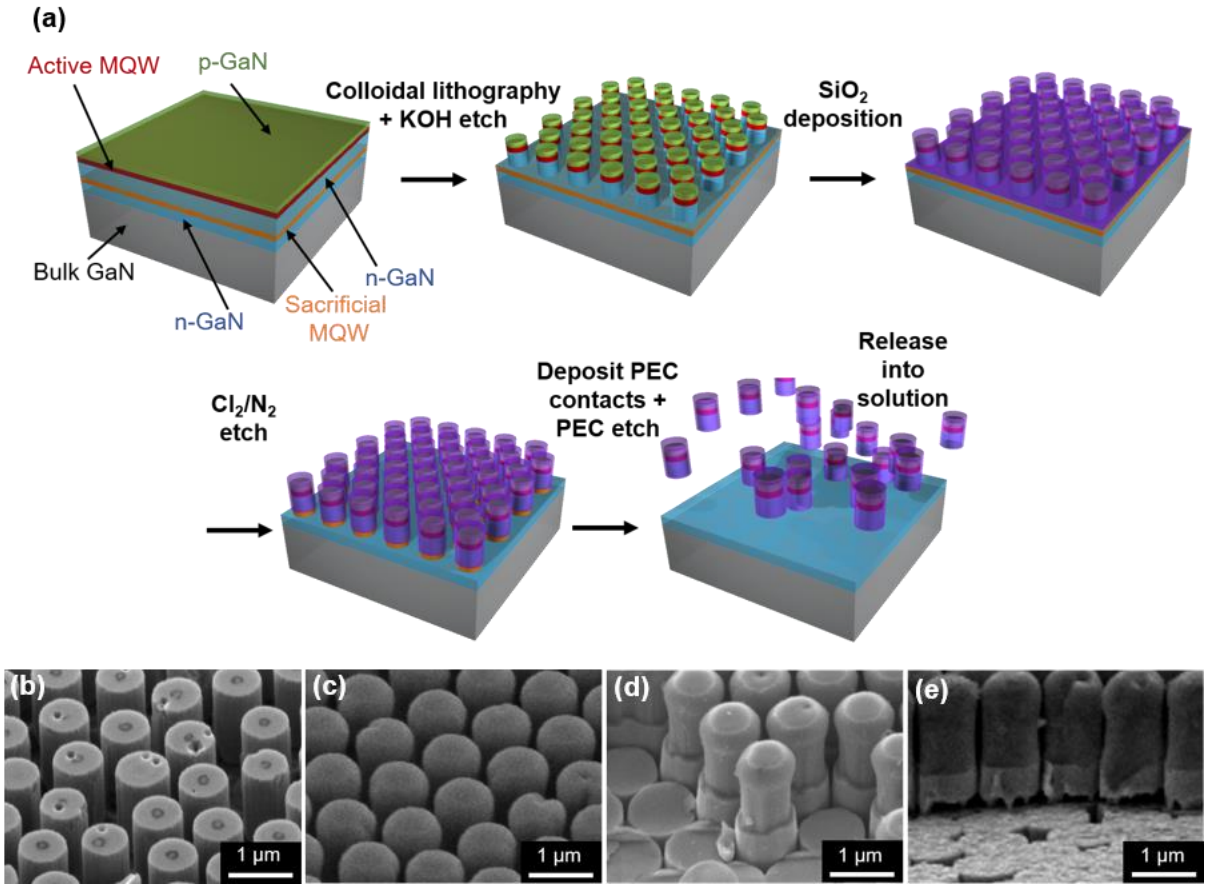

Figure 7.1: (a) Process schematic for c-plane nanoLED fabrication and lift-off using colloidal lithography for patterning and PEC etching of a sacrificial InGaN MQW for release. SEM after (b) colloidal lithography and KOH etch, (c) SiO_2 deposition, (d) Cl_2/N_2 plasma etch to expose sacrificial MQW, and (e) after partial PEC etch for undercut.

After Langmuir-Blodgett deposition of the HCP silica nanosphere mask, the colloids were size reduced using an isotropic inductively coupled plasma reactive ion etch (ICP-RIE) with CF_4/Ar (40:10 sccm), 900 W RF power, no substrate bias, and a pressure of 30 mTorr. HCP conical frusta were etched using ICP-RIE with Cl_2/N_2 (37.5:12.5 sccm), 500 W RF power, 200 W bias power, and a pressure of 9 mTorr. Conditions were adjusted to etch through the p-GaN layer, active MQW, and partially through the n-GaN buffer such that the sacrificial MQW was not exposed. A heated KOH etch was performed after plasma etching to strip plasma damaged material[34], leaving behind cylindrical nanorod structures. An SiO_2 PEC etch mask was then deposited using sputter deposition while spinning the sample to achieve a conformal layer, where the SiO_2 layer was thicker near the top and thinner near the bottom of the nanorods due to the close-packed geometry. The Cl_2/N_2 plasma etch was repeated to etch through the remaining n-GaN buffer and the sacrificial MQW, without etching through the SiO_2 mask at the top of the nanorods. Finally, a PEC contact was deposited in a grid pattern with photolithography (nLOF-2020 resist), e-beam metal deposition of Ti/Au (20/300 nm), and metal lift-off. PEC etching was done in 0.02 M KOH at room temperature (25°C) while stirring under a LED array (λ_{max} = 405 nm, FWHM ~ 15 nm) at constant current (500 mA) to chemically etch the sacrificial MQW and release nanoLEDs into solution. The nanoLEDs were then washed in water 3 times using centrifugation and dried in a vacuum oven. After drying, the SiO_2 mask was stripped with a HF vapor etch.

Photoluminescence (PL) measurements were done using a 405 nm continuous-wave InGaN laser to optically excite the MQWs. The pump source was incident at 45° and the PL was measured normal to the sample surface with a high numerical aperture collector coupled to a UV-vis spectrometer (Ocean Optics USB 2000+) via fiber. X-ray diffraction (XRD) measurements were performed on the as-grown and post-KOH wet etched devices, using monochromated CuKα radiation (λ = 1.5405 Å) on a Panalytical MRD Pro with a 3D Pixcel detector. Reciprocal space maps (RSMs) were generated for symmetric (0002) and asymmetric $(10\bar{1}5)$ and $(11\bar{2}4)$ reflections where 2θ scans were taken at different ω. Lattice constants and the degree of strain relaxation were calculated using a method detailed by Ley *et al.*[7], where the degree of strain relation is defined by the following equation:

$$R = \frac{a_{meas}^{InGaN} - a_{meas}^{GaN}}{a_{ref}^{InGaN}(x) - a_{ref}^{GaN}} \tag{7.1}$$

where R is the degree of strain relaxation, a_{meas}^{InGaN} and a_{meas}^{GaN} are the measured a lattice constants of the InGaN and GaN layers, respectively, $a_{ref}^{InGaN}(x)$ is the expected a lattice constant of fully relaxed InGaN with InN fraction, x, and a_{ref}^{GaN} is the reference a lattice constant of GaN.

7.4 Results and discussion

PL measurements were performed for as-grown GaN/InGaN LEDs using MOCVD, as-etched nanostructures, and after a heated KOH chemical treatment, as shown in

Figure 7.2. The measurements show that the PL disappears for the as-etched structures, likely due to large amounts of surface recombination in the plasma damaged sidewalls, which contain a large amount of defect and trap states, killing performance. However, the heated KOH wet etch is effective in stripping much of the plasma damaged material, recovering luminescence. It has been shown that further reduction of side-wall recombination can be achieved by surface passivation[28–31]. The ~5-fold enhancement in PL for the nanostructured devices compared to the planar as-grown device is likely due to a combination of pump-recycling and increased light extraction efficiency due to the nonplanar geometry. The PL spectra also show a ~10 nm blue shift after nanopatterning, which is thought to be a result of strain relaxation in the light-emitting layers. Strain relaxation can blue shift emission by reducing piezoelectric fields in the MQW which reduces QCSE and pushes the valence band lower and the conduction band higher in energy.

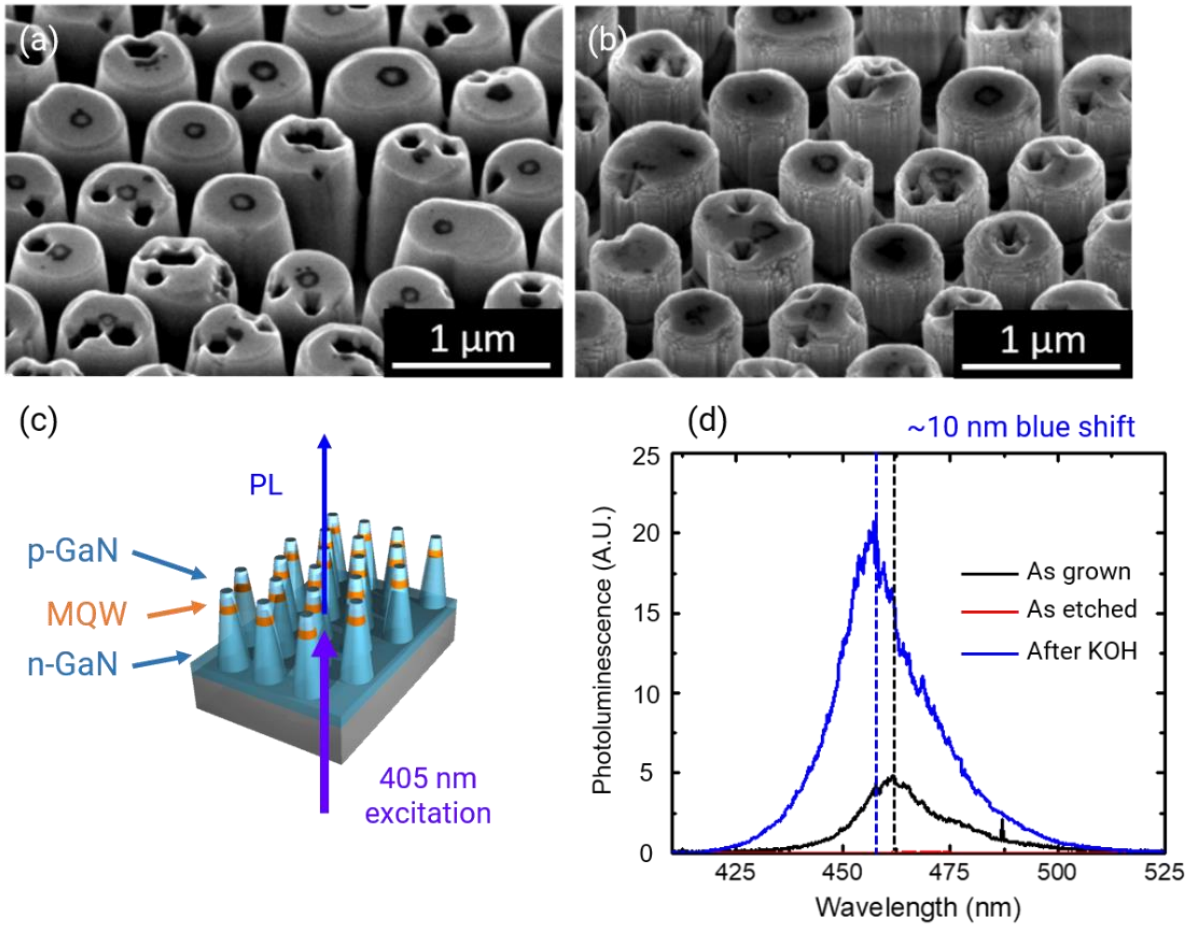

Figure 7.2: (a) SEM images of GaN/InGaN structures after colloid deposition of SiO_2 microspheres (d = 690 nm) and pattern transfer. (b) Structures after a 3 min heated KOH wet etch (~70°C), where etching terminates on the m-plane, resulting in vertical sidewalls. (c) PL measurement schematic where nanorods etched in an LED, consisting of an n-GaN buffer, 5x GaN/InGaN MQW, and p-GaN cap, were pumped with 405 nm laser. (d) Photoluminescence spectra for as-grown GaN/InGaN LEDs via MOCVD, as-etched nanorods in the same LED, and after a heated KOH wet etch treatment to remove plasma damaged sidewall material. The measurements show that the KOH treatment is effective in recovering luminescence from nanoscale devices.

PEC etching was used to remove the buried sacrificial InGaN/GaN MQW layer, in devices grown with both active and sacrificial MQWs, to release individual nanoLEDs from their sapphire growth substrate. However, PEC etching at the exposed N-face of c-plane GaN results in large hexagonal pyramid features with length scales on the

order of the nanoLEDs themselves due to faceting. This roughness is problematic because a significant portion of the nanoLED material volume may be etched out, rendering the device inactive if the active MQW is damaged. To solve this problem, the PEC etch was optimized for minimal interfacial roughness by varying the concentration (0.02 M – 0.5 M) of the KOH etchant. Two types of test structures were fabricated on sapphire substrates; the test stack consisted of 1 μm n-GaN, a sacrificial InGaN MQW, and an n-GaN buffer layer. The first test structure was fabricated using colloidal lithography to produce nanorods (diameter ~ 1 μm), and the second test structure was fabricated using traditional photolithography to produce large mesas (diameter ~ 80 μm). The test structures were used to characterize undercut roughness after PEC etching. SEM images of nanorod test structures after 30 minutes of PEC etching, in Figures 7.3(a,d), show that the roughness dramatically decreased at low KOH concentration (0.02 M). Figures 7.3(b,f) show corresponding optical images of the large mesa test structures after 3 hours of PEC etching, where dark gray regions are unetched and bright regions are etched. Based on these images, low concentration PEC etching also resulted in higher lateral etch rate and uniformity. Two anchor points held the mesas onto the growth substrate such that mesas would not float off into solution after PEC etching the entire sacrificial MQW layer. A polydimethylsiloxane (PDMS) stamp was used to pick up the undercut mesas from the substrate, where anchors were snapped upon pick up, revealing the bottom interface of the mesa features. The bottom interfaces of the mesas were analyzed using SEM and AFM, as

shown in Figures 7.3 (c,d,g,h). The SEM images of the bottom interface of the mesas show roughness reduction when performing PEC etching at low concentration, even for long etch times and large areas. AFM results confirm a substantial reduction in interfacial roughness with a root mean square of ~100 nm and ~30 nm for 0.25 M and 0.02 M KOH etched samples, respectively.

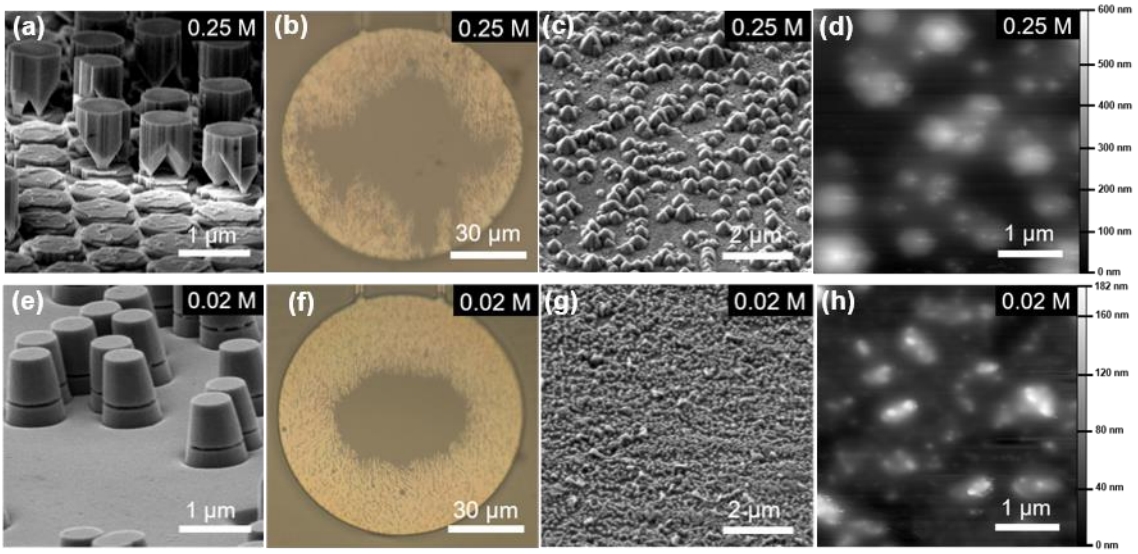

Figure 7.3: (a,e) SEM images of n-GaN/InGaN MQW/n-GaN nanorods after 30 min of PEC undercut etching of the InGaN MQW using 0.25 M and 0.02 M KOH, respectively. (b,f) Bright-field confocal microscope images of microscale n-GaN/InGaN MQW/n-GaN mesas after 3 hours of PEC etching using 0.25 M and 0.02 M KOH. White and grey areas correspond to fully undercut regions and grey areas to unetched regions, respectively. (c,g) SEM images of bottom-side of mesas after PEC etching using 0.25 M and 0.02 M KOH. Mesas were removed from the sapphire substrate using a PDMS stamp after full undercut of the entire sacrificial InGaN MQW. (d,h) AFM scans of the mesa bottom-side after PEC etching using 0.25 M and 0.02 M KOH show RMS roughness of ~100 nm and ~30 nm, respectively.

The reduced roughness is thought to be due to a reduction in the overall etch rate at low etchant concentration, and thus the faceting rate. The improvement in etch rate and uniformity is attributed to the absence of large hexagonal pyramid facet features on the exposed N-face at low concentration, which improves etch rate and uniformity by providing a smooth gap for etchant diffusion. By diffusion through a smooth gap, the etchant can travel farther inward before encountering an obstructing facet feature. Therefore, the optimal PEC etching condition for minimized undercut roughness and maximized etch rate and uniformity is at this low concentration, reaction-limited regime.

Optimized PEC etch conditions were used to undercut nanoLEDs, with diameters of approximately 500 nm, after fabrication. Figure 7.4(a) shows an SEM image of a group of devices after fabrication, undercut, wash, and removal of the residual SiO_2. Devices were drop-cast onto an Si substrate and dried before SEM imaging. Normalized PL measurements of the as-grown device and of the nanoLEDs after separating them from their growth substrate were performed, as shown in Figure 7.4(b). As expected, emission of the sacrificial MQW disappears from the PL spectrum for the released nanoLED sample. There is also a distinct blue-shift in emission of approximately 12 nm from the planar LED to the nanoLEDs. This is likely attributed to reduction of QCSE, as discussed earlier in the section, where compressively strained material can relax laterally, reducing piezoelectric fields in the MQW, which both blue-shifts the emission and increases the internal quantum efficiency[34–37].

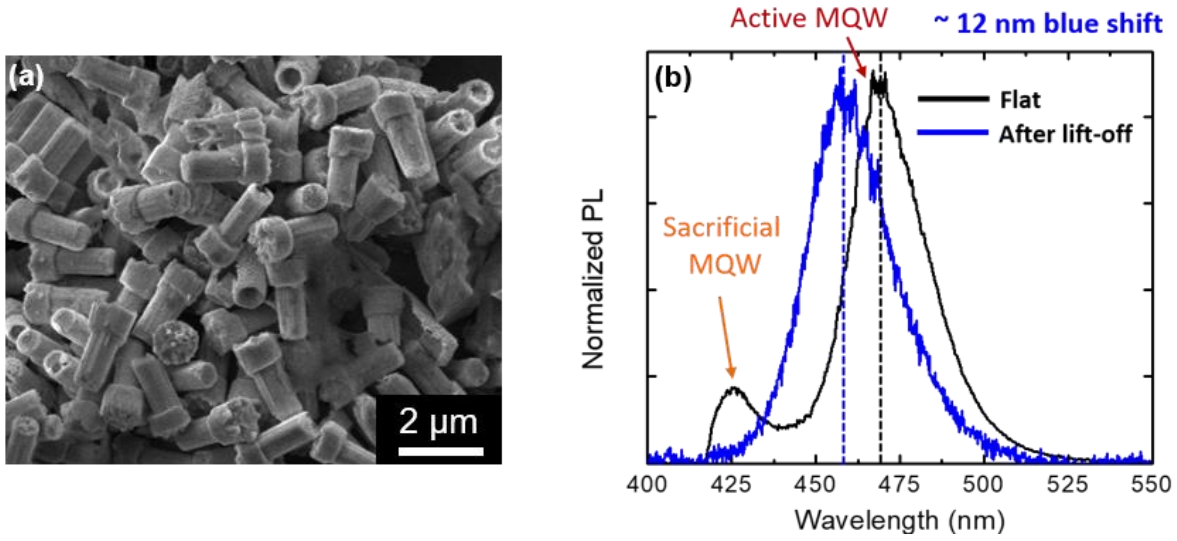

Figure 7.4: (a) SEM image of c-plane GaN nanorods with emitting InGaN/GaN MQW removed from the growth substrate after PEC etching of sacrificial MQW, washing, stripping SiO_2 mask, and drying. (b) Normalized photoluminescence spectra of the as-grown device stack including sacrificial MQW and of nanorods after lift-off as shown in (a).

XRD was used to assess strain states of the nanoLEDs, where RSMs of the symmetric (0002) and asymmetric $(10\bar{1}5)$ and $(11\bar{2}4)$ reflections were generated for the planar as-grown devices and the nanoLEDs after the KOH wet etch, as shown in Figure 7.5. GaN and InGaN peak locations were estimated from RSMs and high resolution ω-2θ scans were performed to determine peak locations with higher accuracy. The high-resolution ω-2θ scans and tabulated peak locations are shown in Figure 7.5(g-i) and Table 7.1, respectively. The In composition (x, $In_xGa_{1-x}N$) was determined to be ~0.136, calculated using the high resolution ω-2θ scan of the symmetric (0002) reflection for the planar, fully coherently strained LED. The ω-2θ scans for the $(10\bar{1}5)$ and $(11\bar{2}4)$ reflections reveal two InGaN layer peaks after nanopatterning, which are attributed

to the two sets of MQWs. The lack of two visible InGaN peaks in the planar case is likely due to poor penetration to deeper sacrificial MQWs, or attenuation of the x-rays in the planar n-GaN buffer, active MQWs, and p-GaN cap, where material in these top layers is partially removed during nanopatterning. Lattice parameters were calculated using a method detailed by Ley *et al.*[7] where specific peak locations were determined from the high resolution ω-2θ scans. The lattice parameters calculated for planar devices were a_{planar}^{GaN} = 3.186 Å , c_{planar}^{GaN} = 5.188 Å, a_{planar}^{InGaN} = 3.181 Å, c_{planar}^{InGaN} = 5.298 Å and for nanostructured devices were a_{nano}^{GaN} = 3.190 Å, c_{nano}^{GaN} = 5.187 Å, a_{nano}^{InGaN} = 3.195, c_{nano}^{InGaN} = 5.266 Å, resulting in a degree of strain relaxation of ~15%, calculated using Equation 7.1.

Reflection		**(0002)**		**(10$\bar{1}$5)**		**(11$\bar{2}$4)**	
		ω°	**2θ°**	**ω°**	**2θ°**	**ω°**	**2θ°**
Planar	**GaN**	17.2773	34.5553	32.0956	104.9547	10.8683	99.9876
	InGaN	16.8869	33.8074	31.1823	103.5109	10.0638	98.9931
Nano	**GaN**	17.2799	34.5543	31.9209	104.9566	10.7213	99.9819
	InGaN	16.9014	33.7972	30.8050	103.1162	9.8574	98.9524

Table 7.1: GaN and InGaN peak positions extracted from high-resolution ω-2θ scans for symmetric (0002) and asymmetric (10$\bar{1}$5) and (11$\bar{2}$4) reflections.

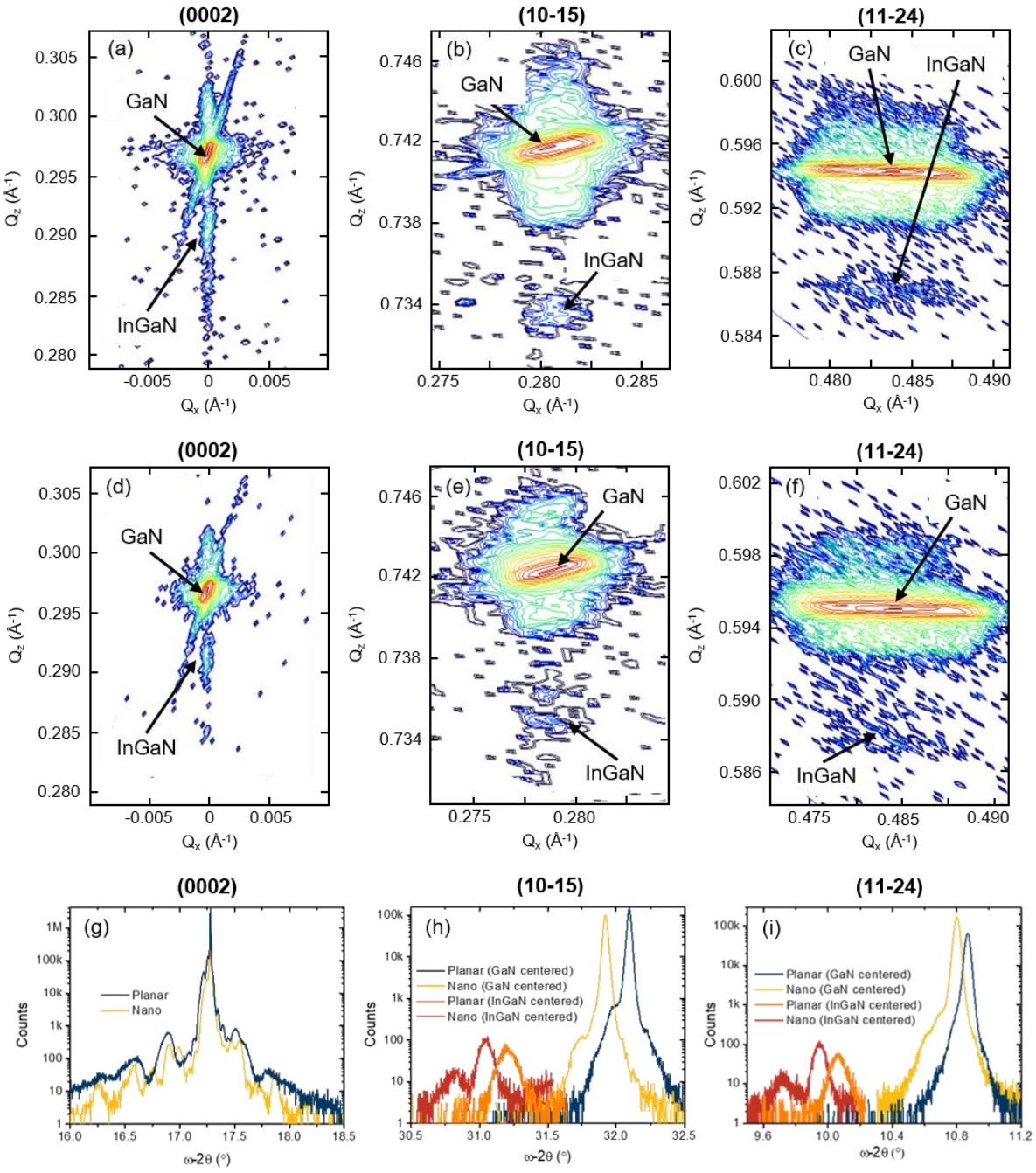

Figure 7.5: RSMs of the symmetric (0002) and asymmetric ($10\bar{1}5$) and ($11\bar{2}4$) reflections for (a-c) planar and (d-f) nanopatterned LEDs, where RSMs were generated by taking 2θ at different ω. High-resolution ω-2θ scans of the (g) symmetric (0002) and asymmetric (h) ($10\bar{1}5$) and (i) ($11\bar{2}4$) reflections for planar and nanopatterned LEDs.

7.5 Summary

The nanoLEDs presented in this chapter are promising for future applications in next generation display technologies. Optically active nanoscale devices were fabricated and separated from their rigid growth substrate using easy and scalable methods, namely colloidal lithography and PEC etching. Here, colloidal lithography with plasma etching was used to define device geometries and PEC etching was used to selectively etch a sacrificial InGaN MQW to release devices into solution. PEC etch parameters were optimized for minimal faceting on the exposed N-face of c-plane GaN, which was achieved at low concentration (~0.02 M KOH), allowing for wafer-scale release of nanoLEDs without damaging active, light emitting layers. After release into solution, nanoLEDs had a 12 nm blueshift in PL compared to the planar case due to strain relaxation, as confirmed by XRD, and reduced QCSE. The fabrication method presented herein is a viable approach for scalable fabrication and lift-off of highly efficient self-emissive LEDs for next generation displays in emerging mobile and wearable electronics.

7.6 References

1. Day, J. *et al.* III-Nitride full-scale high-resolution microdisplays. *Appl. Phys. Lett.* **99**, (2011).

2. Hwang, D., Mughal, A., Pynn, C. D., Nakamura, S. & DenBaars, S. P. Sustained high external quantum efficiency in ultrasmall blue III-nitride micro-LEDs. *Appl. Phys. Express* **10**, (2017).

3. Olivier, F. *et al.* Influence of size-reduction on the performances of GaN-based

micro-LEDs for display application. *J. Lumin.* **191**, 112–116 (2017).

4. Kim, S. Y. *et al.* Organic light-emitting diodes with 30% external quantum efficiency based on a horizontally oriented emitter. *Adv. Funct. Mater.* **23**, 3896–3900 (2013).

5. Sasabe, H. *et al.* High-efficiency blue and white organic light-emitting devices incorporating a blue iridium carbene complex. *Adv. Mater.* **22**, 5003–5007 (2010).

6. N-tech Research. *MicroLED Market Opportunities: 2018-2027*. (2018).

7. Ley, R. *et al.* Strain relaxation of InGaN/GaN multi-quantum well light emitters via nanopatterning. *Opt. Express* **27**, 30081–30089 (2019).

8. Kim, F., Kwan, S., Akana, J. & Yang, P. Langmuir−Blodgett Nanorod Assembly. *J. Am. Chem. Soc.* **123**, 4360–4361 (2001).

9. Burmeister, F. *et al.* From Mesoscopic to Nanoscopic Surface Strutures: Lithography with Colloid Monolayers. *Adv. Mater.* **10**, 495–497 (1998).

10. Pynn, C. D. *et al.* Enhanced light extraction from free-standing InGaN/GaN light emitters using bio-inspired backside surface structuring. *Opt. Express* **25**, 15778 (2017).

11. Ke, M. Y. *et al.* Application of nanosphere lithography to LED surface texturing and to the fabrication of nanorod LED arrays. *IEEE J. Sel. Top. Quantum Electron.* **15**, 1242–1249 (2009).

12. Chen, L.-Y. *et al.* High performance InGaN/GaN nanorod light emitting diode arrays fabricated by nanosphere lithography and chemical mechanical polishing processes. *Opt. Express* **18**, 7664–7669 (2010).

13. Park, H., Baik, K. H., Kim, J., Ren, F. & Pearton, S. J. A facile method for highly uniform GaN-based nanorod light-emitting diodes with InGaN/GaN multi-quantum-wells. *Opt. Express* **21**, 12908–13 (2013).

14. Eo, Y. J. *et al.* Enhanced DC-Operated Electroluminescence of Forwardly Aligned p/MQW/n InGaN Nanorod LEDs via DC Offset-AC Dielectrophoresis. *ACS Appl. Mater. Interfaces* **9**, 37912–37920 (2017).

15. Park, H. K. *et al.* Horizontally assembled green InGaN nanorod LEDs: scalable polarized surface emitting LEDs using electric-field assisted assembly. *Sci. Rep.* **6**, 28312 (2016).

16. Chu, C. F. *et al.* Study of GaN light-emitting diodes fabricated by laser lift-off

technique. *J. Appl. Phys.* **95**, 3916–3922 (2004).

17. Lee, S. H., Park, S. Y. & Lee, K. J. Laser lift-off of GaN thin film and its application to the flexible light emitting diodes. *Proc. SPIE* **8460**, 1–6 (2012).

18. Ueda, T., Ishida, M. & Yuri, M. Separation of thin GaN from sapphire by laser lift-off technique. *Jpn. J. Appl. Phys.* **50**, 1–6 (2011).

19. Wong, W. S. *et al.* Fabrication of thin-film InGaN light-emitting diode membranes by laser lift-off. *Appl. Phys. Lett.* **75**, 1360–1362 (1999).

20. Kim, H. -s. *et al.* Unusual strategies for using indium gallium nitride grown on silicon (111) for solid-state lighting. *Proc. Natl. Acad. Sci.* **108**, 10072–10077 (2011).

21. Kobayashi, Y., Kumakura, K., Akasaka, T. & Makimoto, T. Layered boron nitride as a release layer for mechanical transfer of GaN-based devices. *Nature* **484**, 223–227 (2012).

22. Makimoto, T., Kumakura, K., Kobayashi, Y., Akasaka, T. & Yamamoto, H. A vertical InGaN/GaN light-emitting diode fabricated on a flexible substrate by a mechanical transfer method using BN. *Appl. Phys. Express* **5**, (2012).

23. Ha, J. S. *et al.* The fabrication of vertical light-emitting diodes using chemical lift-off process. *IEEE Photonics Technol. Lett.* **20**, 175–177 (2008).

24. Rogers, D. J. *et al.* Use of ZnO thin films as sacrificial templates for metal organic vapor phase epitaxy and chemical lift-off of GaN. *Appl. Phys. Lett.* **91**, (2007).

25. Chung, K., Lee, C.-H. & Yi, G.-C. Transferable GaN Layers Grown on ZnO-Coated Graphene Layers for Optoelectronic Devices. *Science (80-.).* **330**, 655–657 (2010).

26. Liu, H. F., Liu, W. & Chua, S. J. Epitaxial growth and chemical lift-off of GaInN/GaN heterostructures on c- and r-sapphire substrates employing ZnO sacrificial templates. *J. Vac. Sci. Technol. A Vacuum, Surfaces, Film.* **28**, 590 (2010).

27. Park, J., Song, K. M., Jeon, S. R., Baek, J. H. & Ryu, S. W. Doping selective lateral electrochemical etching of GaN for chemical lift-off. *Appl. Phys. Lett.* **94**, 221907 (2009).

28. Hwang, D. *et al.* Photoelectrochemical liftoff of LEDs grown on freestanding c-plane GaN substrates. *Opt. Express* **24**, 22875–22880 (2016).

29. Stonas, A. R. *et al.* Backside-illuminated photoelectrochemical etching for the fabrication of deeply undercut GaN structures. *Appl. Phys. Lett.* **77**, 2610–2612

(2000).

30. Stonas, A. R., Margalith, T., DenBaars, S. P., Coldren, L. A. & Hu, E. L. Development of selective lateral photoelectrochemical etching of InGaN/GaN for lift-off applications. *Appl. Phys. Lett.* **78**, 1945–1947 (2001).

31. Lora Gonzalez, F., Chan, L., Berry, A., Morse, D. E. & Gordon, M. J. Simple colloidal lithography method to fabricate large-area moth-eye antireflective structures on Si, Ge, and GaAs for IR applications. *J. Vac. Sci. Technol. B* **32**, 051213 (2014).

32. Chan, L. *et al.* Fabrication and optical behavior of graded-index, moth-eye antireflective structures in CdTe. *J. Vac. Sci. Technol. B* **35**, 011201 (2017).

33. Chan, L., Decuir Jr, E. A., Fu, R., Morse, D. E. & Gordon, M. J. Biomimetic nanostructures in ZnS and ZnSe provide broadband anti-reflectivity. *J. Opt.* **19**, 114007 (2017).

34. Li, Q. *et al.* Optical performance of top-down fabricated InGaN/GaN nanorod light emitting diode arrays. *Opt. Express* **19**, 25528 (2011).

35. Chen, H.-S. *et al.* Strain relaxation and quantum confinement in InGaN/GaN nanoposts. *Nanotechnology* **17**, 1454–1458 (2006).

36. Ryou, J.-H. *et al.* Control of Quantum-Confinement Stark Effect in InGaN-Based Quantum Wells. *IEEE J. Sel. Top. Quantum Electron.* **15**, 1080–1091 (2009).

37. Chichibu, S. F. *et al.* Effective band gap inhomogeneity and piezoelectric field in InGaN/GaN multiquantum well structures. *Appl. Phys. Lett.* **73**, 2006–2008 (1998).

Chapter 8

Solution processable semipolar green and blue III-nitride light emitters

Adapted from the Article (to be submitted):

Chan, L., Shapturenka, P., Pynn, C.D., Margalith, T., DenBaars, S.P., Gordon, M.J., "Solution Processable Green, and Blue III-Nitride Light Emitters Grown on Free-Standing GaN," In Preparation.

8.1 Introduction

Next-generation full-color displays, for near-eye and mobile applications, require self-emissive micro- or nanoscale red, green, and blue pixels. C-plane III-nitride blue-emitting microLEDs have been studied extensively for these applications, and the previous chapter discussed in detail a scalable fabrication and lift-off approach for c-plane nanoLEDs[1–6]. However, realizing efficient green and red emitting c-plane LEDs remain a challenge due to the high In composition requirements for long-wavelength emission which result in high material strain. Excess strain is problematic because it can cause increased defect density, piezoelectric fields, and morphological breakdown in the form of v-pits. The AlGaInP material system has long been employed for red-emitting LEDs, but the efficiency of these devices drops dramatically with device size, due to the surface recombination velocity and long minority carrier diffusion length of the material system, making them incompatible for micro- to nanoscale device applications[7–9]. On the other hand, III-nitride LEDs grown on semipolar orientations (Figure 8.1(a)) provide an alternative for long-wavelength emission. GaN/InGaN LEDs grown on semipolar have reduced polarization-induced internal fields (Figure 8.1(b))[10,11], increased optical polarization[12–14], and improved surface morphology[15–17], where the main strain relaxation mechanism is basal plane slip, manifesting in misfit dislocations (MDs) as opposed to v-pit formation. Figure 8.1(c) depicts v-defects formed in c-plane GaN/InGaN LEDS, where large and small v-defects originate in MQWs that are ~1.5 μm and 100 nm from the top surface, respectively. MDs are shown in CL

images in Figure 8.1(d). While MDs are nonradiative centers, they do not cause morphological breakdown, and so efficient devices can still be fabricated on material with MDs. Semipolar micro- and nanoLEDs are therefore promising for aforementioned red and green emitting pixels in displays, and long-wavelength emission has already been demonstrated in devices grown on semipolar orientations[18–23]. A fabrication and lift-off process must therefore be developed for micro- and nanoscale semipolar devices for production and assembly of next-generation displays. In this chapter, a scalable fabrication approach for producing nanoscale semipolar blue, green, and red emitting LEDs is presented. Large-area selective PEC etching of sacrificial MQWs was developed to separate devices from the rigid growth substrate and colloidal lithography was adapted to produce nanoLEDs.

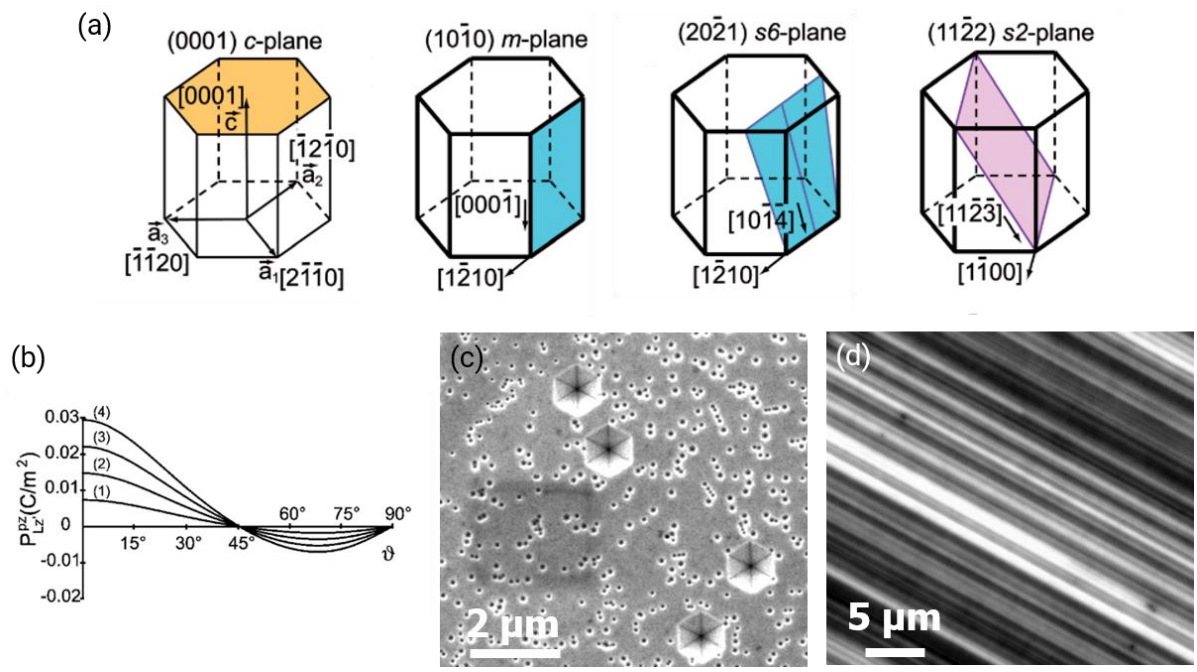

Figure 8.1: (a) Crystallographic planes in wurtzite III-nitride system for c-plane (0001), m-plane (10$\bar{1}$0), and semipolar planes (20$\bar{2}$1) and (11$\bar{2}$2)[24]. (b) Dependence of piezoelectric polarization on semipolar plane orientation ϑ ($\vartheta_{\text{c-plane}}$ = 0°, $\vartheta_{\text{m-plane}}$ = 90°, $\vartheta_{(20\text{-}21)}$ = 75° , $\vartheta_{(11\text{-}22)}$ = 54°) of $In_xGa_{1-x}N$ grown on GaN for composition x = 0.05 (1), 0.1 (2), 0.15 (3), and 0.02 (4)[10]. (c) SEM image of v-defects in c-plane GaN/InGaN LEDs and (d) CL image of misfit dislocations (dark lines) in InGaN buffer grown on bulk semipolar (11$\bar{2}$2) GaN substrate. Panel (a) reprinted from [24] and panel (b) reprinted from [10] with permission from AIP Publishing.

8.2 Experimental methods

GaN/InGaN LEDs with sacrificial MQWs were homoepitaxially grown via MOCVD on free-standing (20$\bar{2}$1) GaN substrates (Mitsubishi Chemical Company). Epitaxial structures consisted of a 2 µm n-GaN buffer, an unintentionally doped (UID) InGaN/GaN six-period MQW sacrificial region, 1.5 µm n-GaN layer, UID InGaN/GaN six-period MQW active region, and 100 nm p-GaN layer. The In composition for the sacrificial InGaN layers was ~10% and the In composition for blue-emitting and green-

emitting active regions was ~15% and ~25%, respectively. A schematic of the device fabrication procedure is presented in Figure 8.2. First, a Ti/Au (20/300 nm) square grid pattern (20 μm bars with 200 μm pitch) was deposited on the back-side of the bulk GaN substrate using standard photolithography and metal lift-off, to act as an electrode for PEC etching. The PEC contact was designed such that the bars were close enough for electron transport, but sparse enough so as to not block or absorb a significant amount of the photoexcitation source.

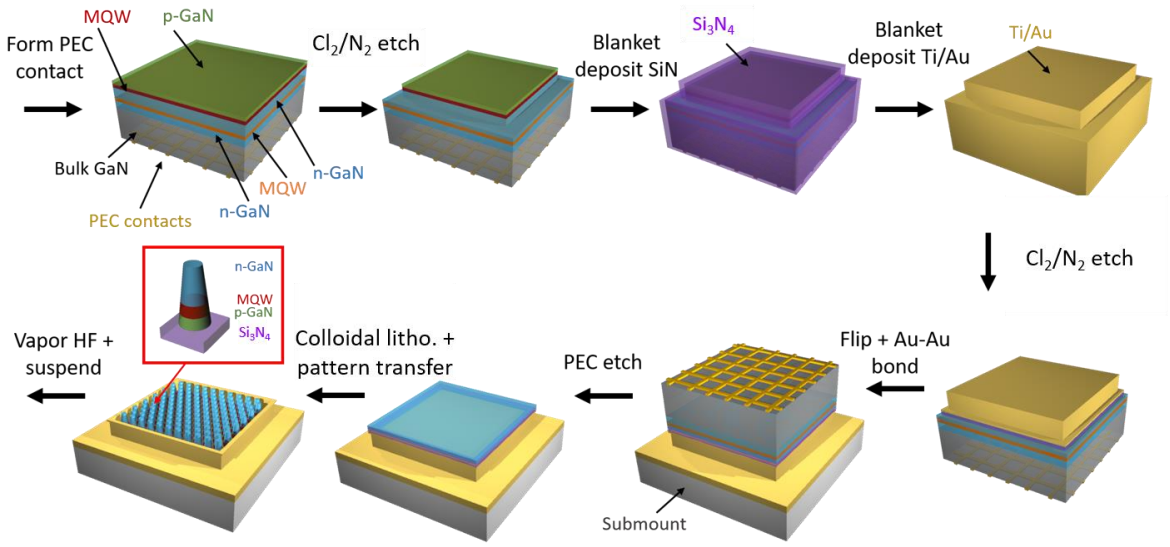

Figure 8.2: Process schematic for fabrication of semipolar nanoLEDs. LEDs with a sacrificial MQW were grown on freestanding semipolar GaN substrates. A PEC contact grid was deposited on the substrate backside. A Cl_2/N_2 etch was performed to define a mm-scale mesa. Si_3N_4 was deposited using sputter and Ti/Au was deposited using e-beam. A second mesa etch was done to expose sacrificial MQWs and the whole substrate was flipped and Au-Au thermocompression bonded onto a submount. PEC etching was done to remove the growth substrate and colloidal lithography was used to define nanoLEDs. The final devices were removed from the substrate by HF vapor etching the underlying Si_3N_4.

A large-area mesa pattern was defined on the device side using photolithography and a mesa etch was done using ICP-RIE with Cl_2/N_2 etch gases (37.5/12.5 sccm), 500 W RF power, 200 W bias power, and a pressure of 9 mTorr. The etch was done until achieving a depth of approximately 1 μm, in the n-GaN buffer between the active and sacrificial MQWs. A 300 nm thick film of Si_3N_4 was blanket deposited using a sputter system and a 20/300 nm layer of Ti/Au was deposited using e-beam. The Si_3N_4 acts as a wet etch mask to protect the active MQW during later PEC etching. A second photolithography step was done to define a second, larger mesa centered over the first mesa, and the same ICP-RIE etch was done to etch past and expose the sacrificial MQWs. The full structure was flipped onto a Ti/Au coated sapphire sub-mount and Au-Au thermocompression bonding was done at 300°C for 2 hours. PEC etching was done in 0.05 M KOH at room temperature (25°C) while stirring, under an LED array (λ_{max} = 405 nm, FWHM ~ 15 nm) at constant current (500 mA), to chemically etch the sacrificial MQW layer and remove the bulk GaN substrate. The GaN-air surface after PEC etching is very smooth, as no faceting occurs due to the lack of an exposed N-face for the $(20\bar{2}1)$) orientation, and colloidal deposition on this surface can easily be performed, as shown in Figure 8.3. Silica colloids (d = 2530 nm) were deposited using the Langmuir-Blodgett method; mask size reduction etching was done using an isotropic CF_4/Ar ICP-RIE etch with 900 W RF power, no bias, and a pressure of 15 mTorr; pattern transfer was done using the same Cl_2/N_2-based ICP-RIE etch used for the mesa etches. The hexagonally packed nanoLEDs were then separated from the

substrate using an HF vapor etch to remove the underlying Si_3N_4 and suspended in water by sonication. nLEDs in solution were drop-cast on an Si substrate and dried for subsequent SEM imaging.

Photoluminescence (PL) measurements were done using a 405 nm continuous-wave InGaN laser to optically excite the MQWs. The pump source was incident at 45° and the PL was measured normal to the sample surface with a high numerical aperture collector coupled to a UV-vis spectrometer (Ocean Optics USB 2000+) via fiber. Cathodoluminescence (CL) measurements were done in an FEI Inspect field-emission SEM using a Gatan MonoCL4 measurement system.

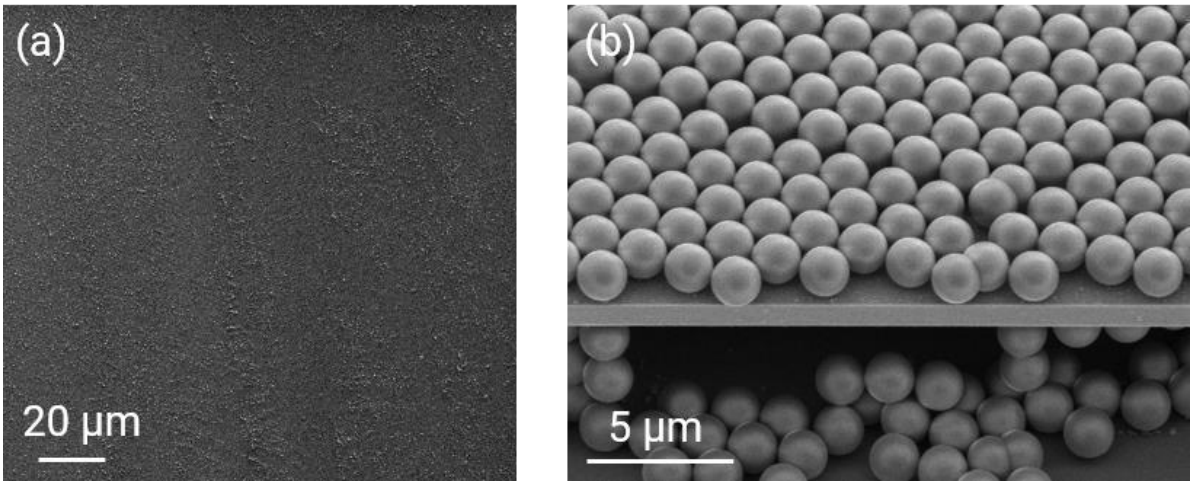

Figure 8.3: (a) SEM of exposed n-GaN surface remaining on the submount after removal of growth substrate using PEC etching. The surface is smooth, and faceting does not occur due to lack of exposed N-face. (b) SEM image of colloids after Langmuir-Blodgett deposition on LED surface shown in (a). Conformal and uniform coating was achieved.

8.3 Results and discussion

The large-area PEC etch for selective removal of the sacrificial MQW layer for growth substrate lift-off was done for both blue-emitting and green-emitting LEDs. Normalized PL measurements for as-grown and post-PEC lift-off, presented in Figure 8.4, show both active and sacrificial MQW emission for the as grown devices. The sacrificial MQW peak disappears after PEC etching while strong emission from the active MQWs remain. Yellow emission (λ_{max} ~ 550 nm) is also seen in the PL of the as-grown devices (only the tail is shown in Figure 8.4(a)), but disappears after PEC lift-off, suggesting that the defect emission originates in the bulk GaN substrate.

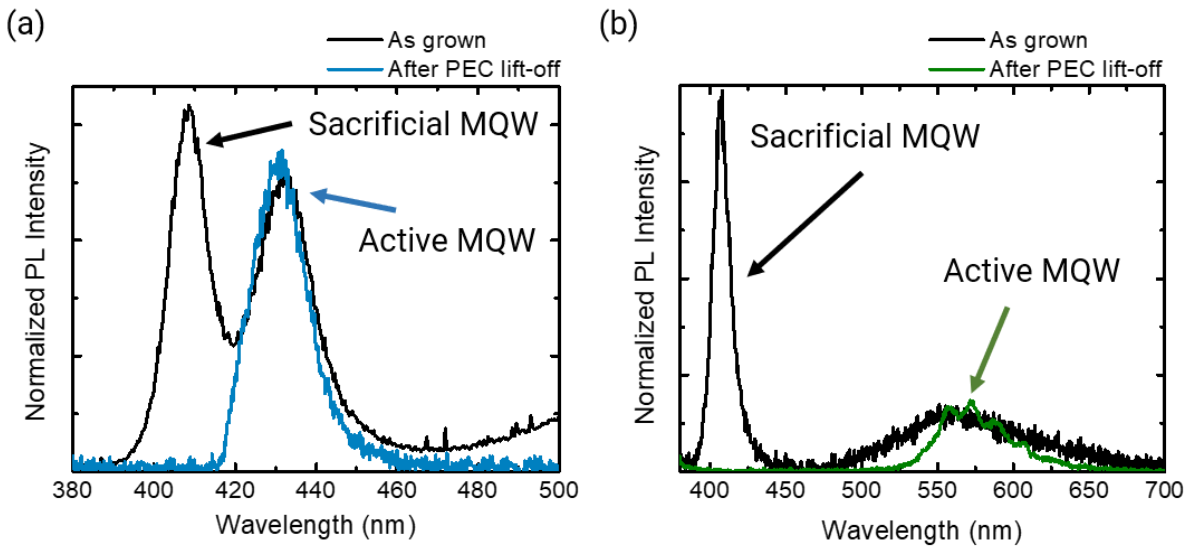

Figure 8.4: Normalized photoluminescence measurements of the as-grown (black) devices, where emission from both sacrificial and active MQWs are present, and after PEC lift-off (colored), where only active MQW emission remains for (a) blue-emitting (λ_{max} = 430 nm) devices and (b) green-emitting (λ_{max} = 560 nm) devices.

Figure 8.5(a) depicts SEM images of blue-emitting nanoLEDs after colloidal lithography and plasma etching on Si_3N_4 and Figure 8.5(b) shows images after removal from the submount by HF vapor etching the underlying Si_3N_4, sonicating in water. NanoLEDs were drop-cast and dried on an Si substrate prior to SEM imaging. Top-down monochromatic CL images (Fig. 8.5(c,d)) using a beam voltage of 5 kV of the structures depicted in Figure 8.5(a), show strong GaN emission at λ = 365 nm and InGaN MQW emission at λ = 430 nm. The emission from the MQWs appear ring-like due to attenuation of the electron beam in the thick ~1.5 μm n-GaN layer; because the nanoLED has frustum-like geometry with angled sidewalls, the electron beam only reaches the MQWs near the sidewalls. Monte-Carlo simulations of the electron beam trajectory through GaN/InGaN were done using Casino[25], as shown in Figure 8.5(e). With a beam voltage of 5 kV, the primary electrons only reach a depth of approximately 150 nm. The CL images show that after fabrication, the nanoLEDs are still optically active.

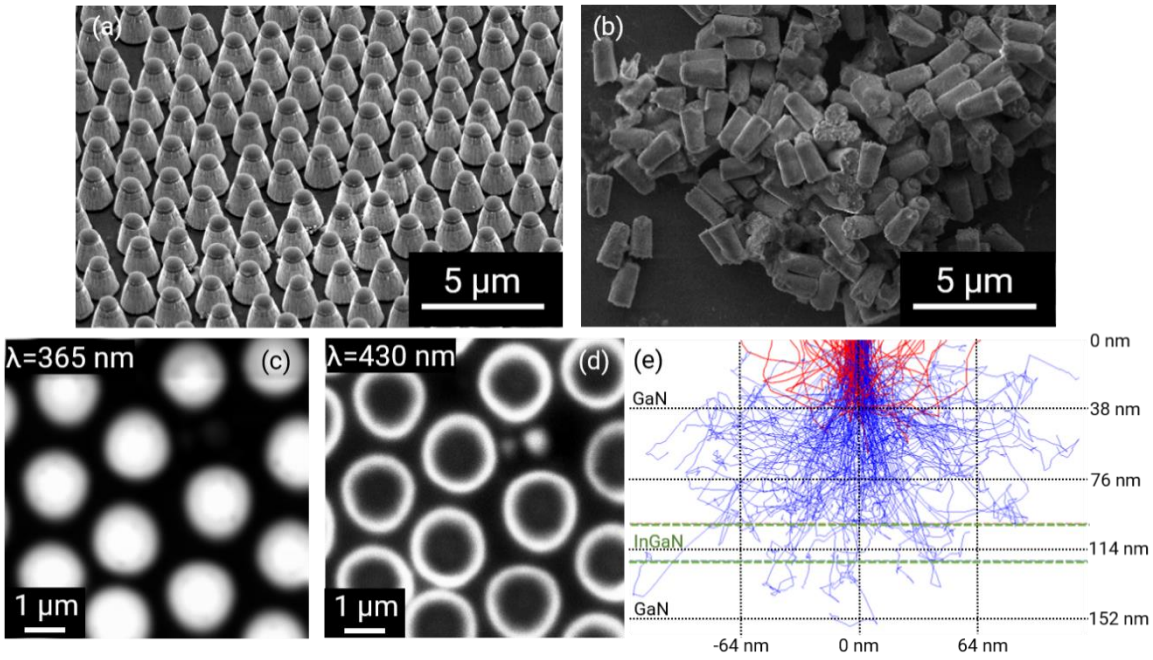

Figure 8.5: SEM images of (a) nanoLEDs fabricated with colloidal lithography and plasma etching on the submount. The material directly underneath the nanoLEDs is Si_3N_4. (b) SEM images of nanoscale LEDs after HF vapor etching the Si_3N_4 and deposition on an Si wafer. Monochromatic CL images of the nanoLEDs, taken with a beam voltage of 5 keV, at (c) λ = 365 nm and (d) λ = 430 nm show strong emission from the n-GaN and InGaN/GaN MQWs, respectively. The emission from the MQW appears as a ring due to attenuation of the electron beam through the thick (~1.5 μm) n-GaN on top. (e) Monte Carlo simulation of 5 keV electron beam trajectory through a material stack of 100 nm GaN and 20 nm InGaN on a GaN substrate where blue lines represent electrons that terminated in the material and red lines represent backscattered electrons. The penetration depth reaches approximately 150 nm.

8.4 Summary

A scalable fabrication approach for semipolar nanoLEDs was developed, which relies on forming a mm-scale mesa, Au-Au thermocompression bonding to a sub-mount, large-area PEC etching, and colloidal lithography. Blue and green-emitting nanoLEDs were fabricated using this approach, where PL and CL measurements were used to

characterize the light emission properties of the devices. Monte Carlo simulations were employed to predict electron beam interactions with the material and to understand patterns shown in CL images. The approach presented here is a promising route to fabricate and suspend red, green, and blue-emitting semipolar GaN/InGaN nanoLEDs in solution for subsequent high-throughput assembly of next-generation full-color displays.

8.5 References

1. Wong, M. S. *et al.* High efficiency of III-nitride micro-light-emitting diodes by sidewall passivation using atomic layer deposition. *Opt. Express* **26**, 21324 (2018).

2. Wong, M. S. *et al.* Size-independent peak efficiency of III-nitride micro-light-emitting-diodes using chemical treatment and sidewall passivation. *Appl. Phys. Express* **12**, (2019).

3. Templier, F. *et al.* High-resolution active-matrix 10-um pixel-pitch GaN LED microdisplays for augmented reality applications. in *Proceedings of SPIE* (2018). doi:10.1117/12.2294527

4. Olivier, F. *et al.* Influence of size-reduction on the performances of GaN-based micro-LEDs for display application. *J. Lumin.* **191**, 112–116 (2017).

5. Day, J. *et al.* III-Nitride full-scale high-resolution microdisplays. *Appl. Phys. Lett.* **99**, 031116 (2011).

6. Hwang, D., Mughal, A., Pynn, C. D., Nakamura, S. & DenBaars, S. P. Sustained high external quantum efficiency in ultrasmall blue III-nitride micro-LEDs. *Appl. Phys. Express* **10**, (2017).

7. Wong, M. S. *et al.* Improved performance of AlGaInP red micro-light-emitting diodes with sidewall treatments. *Opt. Express* **28**, 5787–5793 (2020).

8. Hwang, J. Il, Hashimoto, R., Saito, S. & Nunoue, S. Development of InGaN-based red LED grown on (0001) polar surface. *Appl. Phys. Express* **7**, 071003 (2014).

9. Horng, R. H., Chien, H. Y., Tarntair, F. G. & Wuu, D. S. Fabrication and Study on Red Light Micro-LED Displays. *IEEE J. Electron Devices Soc.* **6**, 1064–1069 (2018).

10. Romanov, A. E., Baker, T. J., Nakamura, S. & Speck, J. S. Strain-induced polarization in wurtzite III-nitride semipolar layers. *J. Appl. Phys.* **100**, 1–10 (2006).

11. Park, S.-H. & Ahn, D. Depolarization effects in (1122) -oriented InGaN/GaN quantum well structures. *Appl. Phys. Lett.* **90**, (2007).

12. Zhao, Y. *et al.* Optical polarization characteristics of semipolar ($30\bar{3}1$) and ($30\bar{3}\bar{1}$) InGaN/GaN light-emitting diodes. *Opt. Express* **21**, A53 (2013).

13. Zhao, Y. *et al.* High optical polarization ratio from semipolar (2021) blue-green InGaN/GaN light-emitting diodes. *Appl. Phys. Lett.* **99**, (2011).

14. Fellows, N., Sato, H., Masui, H., DenBaars, S. P. & Nakamura, S. Increased polarization ratio on semipolar (11$\bar{2}$2) InGaN/GaN light-emitting diodes with increasing indium composition. *Jpn. J. Appl. Phys.* **47**, 7854–7856 (2008).

15. Wernicke, T. *et al.* Surface morphology of homoepitaxial GaN grown on non- and semipolar GaN substrates. *Phys. Status Solidi Basic Res.* **248**, 574–577 (2011).

16. Browne, D. A., Young, E. C., Lang, J. R., Hurni, C. A. & Speck, J. S. Indium and impurity incorporation in InGaN films on polar, nonpolar, and semipolar GaN orientations grown by ammonia molecular beam epitaxy. *J. Vac. Sci. Technol. A* **30**, (2012).

17. Baker, T. J. *et al.* Characterization of planar semipolar gallium nitride films on spinel substrates. *Jpn. J. Appl. Phys.* **44**, 920–922 (2005).

18. Funato, M. *et al.* Blue, green, and amber InGaN/GaN light-emitting diodes on semipolar {1122} GaN bulk substrates. *Jpn. J. Appl. Phys.* **45**, L659–L662 (2006).

19. Pynn, C. D. *et al.* Green semipolar III-nitride light-emitting diodes grown by limited area epitaxy. *Appl. Phys. Lett.* **109**, 41107 (2016).

20. Kowsz, S. J. *et al.* Demonstration of phosphor-free polarized white light emission from monolithically integrated semipolar InGaN quantum wells. *Appl. Phys. Lett.* **107**, 101104 (2015).

21. Feezell, D. F., Schmidt, M. C., DenBaars, S. P. & Nakamura, S. Development of nonpolar and semipolar InGaN/GaN visible light-emitting diodes. *MRS Bull.* **34**, 318–323 (2009).

22. Zhao, Y. *et al.* Green semipolar (2021) InGaN light-emitting diodes with small wavelength shift and narrow spectral linewidth. *Appl. Phys. Express* **6**, (2013).

23. Li, H. *et al.* Study of efficient semipolar (11-22) InGaN green micro-light-emitting diodes on high-quality (11-22) GaN/sapphire template. *Opt. Express* **2**7, (2019).

24. Romanov, A. E. *et al.* Basal plane misfit dislocations and stress relaxation in III-nitride semipolar heteroepitaxy. *J. Appl. Phys.* **109**, 103522 (2011).

25. Gauvin, R. Casino. https://www.gel.usherbrooke.ca/casino/ (2000).

Chapter 9

Conclusion and Outlook

9.1 Chapter overview

This thesis has focused on the development and application of a scalable, colloid-based nanopatterning method to engineer light-matter interactions and enable novel nanoscale devices. As presented in this work, surface structures made using colloidal nanopatterning have been implemented for anti-reflection coatings that work via the GRIN effect in IR-relevant materials to improve the performance of detectors and optics. They have also been implemented on the outcoupling surfaces of LEDs to improve light extraction efficiency (9x at normal and 5x total for the best performing nanostructured surfaces). The method has also been adapted to fabricate novel III-nitride nanoscale LEDs for applications as pixels in next-generation displays. While these applications of the colloidal nanopatterning approach have demonstrated the robustness and versatility of the method, many exciting directions exist involving fluidic assembly of nanoLEDs, 2-D strain-relaxed InGaN buffers for long-wavelength emitting LEDs, and electrically addressable nanorod LED arrays using large-area flexible, conductive stamps.

9.2 Langmuir-Blodgett assembly of nanoLEDs

Chapters 7 and 8 presented two methods to fabricate nanoscale c-plane and semipolar III-nitride light emitters for applications in next-generation displays based on wafer-scale nanopatterning and chemical undercut to release devices into solution. The next challenge for implementation of nanoLEDs in display applications is device assembly.

Previous work has use pick-and-place approaches to assemble red, green, and blue LEDs onto alternate transparent and flexible substrates. A photograph of red, green, and blue microLEDs printed on flexible plastic using transfer printing is shown in Figure 9.1(a). The transfer printing technique, first developed and widely implemented by the Rogers group[1,2], has been used to print arrays of various devices such as solar cells[3–5], LEDs[6–8], integrated circuits[9,10], sensors[11], etc. onto alternate, flexible substrates. However, this approach is not compatible with devices made using colloid-based nanopatterning because it requires on-wafer order, i.e., devices must be fabricated in well-ordered arrays. Colloidal lithography only provides short range order, as shown in Figure 9.1(b). Furthermore, transfer printing is slow, as multiple printing steps must be done for each color emitter on an individual display, so it is impractical for large display applications, such as televisions and monitors.

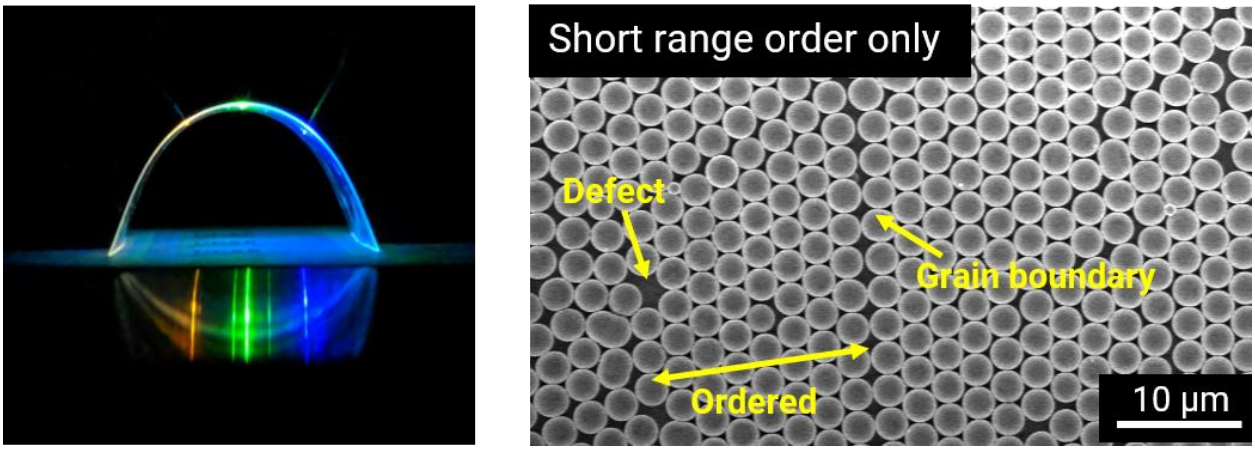

Figure 9.1: (a) Photograph of red, green, and blue microLEDs printed on flexible acrylic using transfer printing and electrically pumped using 3 sets of 2-point probes. (b) SEM image of colloid mask on GaN, showing well-ordered areas separated by defects and grain boundaries.

An alternative, high-throughput assembly approach must be developed. Recently, researchers have shown promising results for fluidic assembly of III-nitride nano- and microscale LEDs. For instance, Eo *et al.* and Park *et al.* have developed an orientation-controlled alignment process of nanoLEDs by applying electric fields across interdigitated metal electrodes[12,13]. Chow *et al.* developed an electrostatic assembly and transfer method to print microscale Si and GaN chips in ordered arrays (<1 μm and <1° precision)[14].

A new approach for fluidic assembly that leverages the Langmuir-Blodgett (LB) deposition technique already used extensively in this work, is presented in this section. The proposed assembly method would involve chemically functionalizing one end of the nanoLEDs. This could involve depositing an Au contact on just one end and performing a thiol functionalization to render it hydrophobic. Once the functionalization and lift-off into solution are performed, the functionalized colloidal devices can potentially be pinned at an air-water or oil-water interface in an LB trough, as depicted in Figure 9.2. Deposition of the devices can then be done by via LB dip-coating onto a solid substrate.

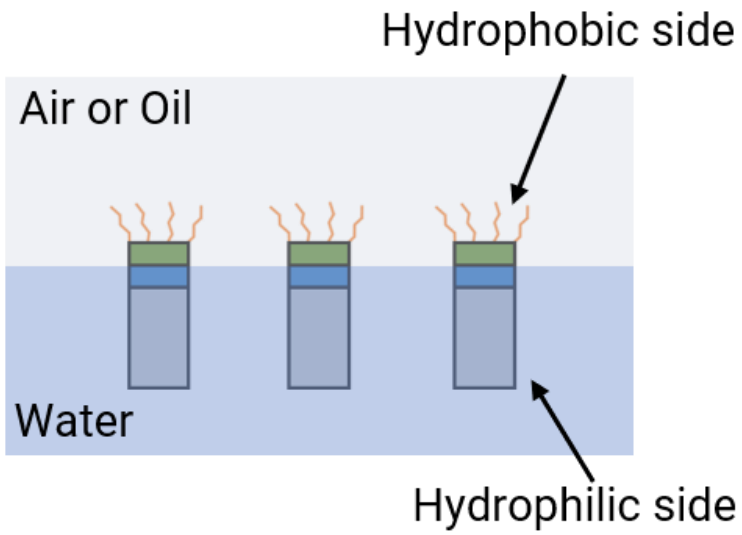

Figure 9.2: Schematic of selectively functionalized nanoLEDs suspended at an air-water or oil-water interface. Green, blue, and grey sections of the nanoLEDs represent the *p*-GaN, MQWs, and *n*-GaN, respectively. The nanoLEDs could then be deposited on a solid substrate via Langmuir-Blodgett dip-coating.

9.3 2D Strain-relaxed InGaN buffers

As mentioned in Chapter 7, long-wavelength emission in the III-nitride material system requires high In composition, but is limited by strain issues. The excess strain leads to increased defect density and morphological breakdown due to strain relaxation mechanisms (v-pits in c-plane). One way to reduce the strain energy is to grow material gradually from the GaN substrate to material that more closely resembles the final light-emitting layer, i.e., growth of low In composition material, followed by material with increasing In composition. A simple approach is to grow a partially, or one-dimensionally, in-plane strain-relaxed InGaN buffer on semipolar GaN, and then achieve full two-dimensional relaxation via nanopatterning. These

substrates can then be used for subsequent high In content QW regrowth. In the following preliminary experiments, nanopatterning was done using colloidal lithography and plasma etching.

Thick InGaN buffers (~300 nm thick) with ~8% In were grown on freestanding semipolar ($11\bar{2}2$) GaN substrates via MOCVD. Colloidal lithography and plasma etching, detailed in previous chapters, was used to produce nanostructures with 500 nm pitch and 500 nm height, as shown in Figure 9.3. QWs were regrown on these structures consisting of a thin UID GaN layer, a 3-period GaN/InGaN QW structure, and a thin UID GaN cap.

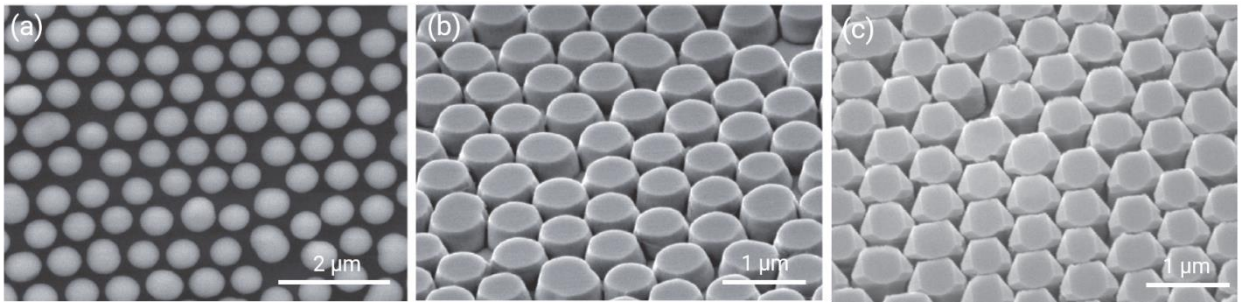

Figure 9.3: SEM images of (a) size reduced SiO_2 colloids on a 1-D relaxed InGaN buffer, (b) after Cl_2/N_2 ICP-RIE etch ~500 nm deep into the relaxed InGaN buffer, and (c) after regrowth.

Full 2-D strain-relaxation must be confirmed before regrowth. RSMs were generated using XRD for these structures, before and after regrowth, but because of low signal and resolution, layer peaks could not be resolved. An alternative high-resolution XRD method, developed by Frentrup *et al.*[15], was employed to calculate

lattice parameters for the semipolar GaN and InGaN layers. Briefly, the method involves deriving the lattice parameters by performing a least squares fit to the following expression using at least four high-resolution ω-2θ scans:

$$\frac{1}{d_{hkl}^2} = \frac{4}{3}\frac{h^2+k^2+hk}{a^2} + \frac{8h^2+8k^2+20hk}{3\sqrt{3}a^2}\delta_\gamma + \frac{4(hl+kl)}{ac}\delta_\alpha + \frac{l^2}{c^2} \quad (9.1)$$

where d_{hkl} is the interplanar spacing, δ_α and δ_γ are the change in angles lattice angles α and γ, respectively, and a and c are the in-plane and out-of-plane lattice parameters, respectively. The approach was used to derive the interplanar spacing and lattice parameters for a GaN $(11\bar{2}2)$ bulk substrate (Table 9.1).

(hkil)	θ°	Δθ°	d_{hkl} (Å)
-1 2 -1 -2	34.5508	0.0102	1.3582
0 0 0 2	17.2871	0.0065	2.5922
0 0 0 4	36.4598	0.0076	1.2962
0 1 -1 0	16.1980	0.0050	2.7614
1 1 -2 0	28.8869	0.0218	1.5945
1 1 -2 2	34.5490	0.0078	1.3583
2 -1 -1 0	28.8783	0.0347	1.5950

Table 9.1: θ, Δθ, and d_{hkl} for various on- and off-axis reflections (hkil) from high-resolution ω-2θ scans of semipolar $(11\bar{2}2)$ GaN.

The calculated lattice parameters for GaN were a = 3.1888 Å, c = 5.1850 Å, δ_α = -4.0421e-04°, and δ_γ = -7.8763e-04°, which are in excellent agreement with the expected values of a = 3.1896 Å, c = 5.1855 Å. Similar measurements were done on an as-grown 1-D relaxed InGaN buffer (275 nm thick, 8% In) on (11$\bar{2}$2) semipolar GaN, and measurement results are summarized in Table 9.2.

(hkil)	θ°	Δθ°	d_{hkl} (Å)
-1 1 0 1	18.3988	0.0054	2.4405
0 0 0 2	17.1801	0.0141	2.6079
0 0 0 4	36.2116	0.0197	1.3039
0 1 -1 0	16.1802	0.0338	2.7643
1 -1 0 1	18.3993	0.0053	2.4405
1 0 -1 0	16.1809	0.0069	2.7641
1 1 -2 0	28.6089	0.0360	1.6087
1 1 -2 2	34.1760	0.0336	1.3713

Table 9.2: θ, Δθ, and d_{hkl} for various on- and off-axis reflections (hkil) from high-resolution ω-2θ scans of a relaxed InGaN buffer (275 nm thick, 8% In) grown on semipolar (11$\bar{2}$2) GaN.

The calculated lattice parameters for the relaxed InGaN buffer were a = 3.1904 Å, c = 5.2160 Å, δ_α = -6.9e-03°, δ_γ = 2.4e-03°, which are also in excellent agreement with the expected values, which are a = 3.2136 Å, c = 5.2210 Å, calculated using Vegard's Law. Once the lattice parameters are known, the degree of strain relaxation can be

determined using Equation 7.1 (Chapter 7). The high-resolution XRD approach discussed in this section can be used to asses strain states for relaxed InGaN buffers before and after nanopatterning, to verify full relaxation. Once the strain states are known, regrowth of long-wavelength emitting QWs can be done.

9.3 Electrically addressable nanorod LEDs using polymer contact

Nanorod LEDs are promising for applications in solid-state lighting and displays due to their increased efficiency and directionality compared to their planar counterparts. As discussed previously (Chapters 3 and 7), nanopatterning LEDs can improve IQE by providing strain relaxation, which reduces piezoelectric fields in the material, reducing QCSE. Nanopatterning can also improve the EQE by enhancing the light extraction efficiency, as discussed in Chapter 6. Recent results also show that nanorod LEDs have more directional emission compared to planar LEDs. Angle-resolved PL measurements showed that nanorod LEDs with structure pitch of 310 nm and 690 nm provided increased emission intensity and directionality (Figure 9.4). However, fabrication of electrically addressable arrays of nanorod LEDs is complicated by the difficulty of depositing a conformal p-contact on a nonplanar surface. A typical process involves: (1) fabrication of the nanorods using a nanopatterning approach, (2) passivation of each nanorod with a dielectric material for electrical insulation, (3) planarization of the dielectric, (4) defining an opening in the dielectric for subsequent metallization, and (5) deposition of p- and n-contacts. Furthermore, these processing

steps are nontrivial and process optimization of each must be done. A simple approach for electrically addressing an array of nanorod LEDs is proposed in this section, which involves using a flexible polydimethylsiloxane (PDMS) stamp coated with a transparent, conductive polymer that functions as a large-area p-contact. Poly(3,4-ethylenedioxythiophene) polystyrene sulfonate (PEDOT:PSS) is a promising material for this application because it has been shown to be transparent, conductive, and stretchable[16–18]. A schematic of the envisioned device is shown in Figure 9.5.

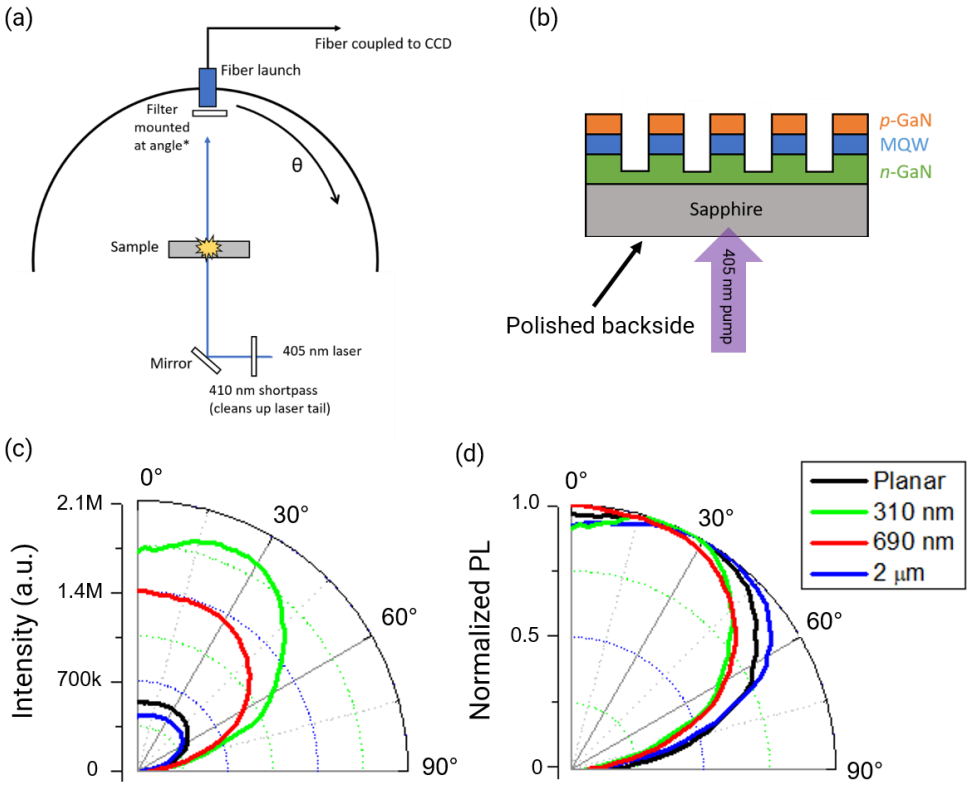

Figure 9.4: (a) Schematic of angle-resolve PL measurement set-up. (b) Schematic of nanorod LED with polished backside and backside pumping using 405 nm laser. (c) Angle-resolve PL intensity of planar and nanorod LEDs with different nanostructure diameter (aspect ratio ~2:1). (d) Normalized angle-resolved PL of planar and nanorod LEDs.

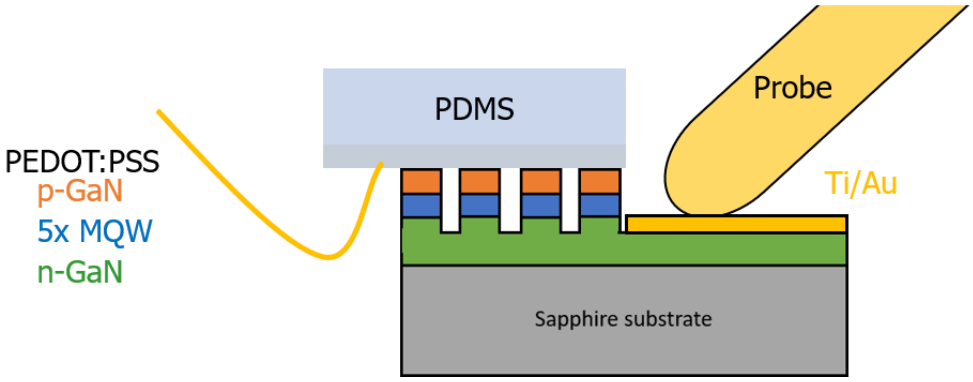

Figure 9.5: Schematic of proposed electrically injected nanorod LED using a flexible large-area PDMS stamp coated with a transparent, conductive polymer (PEDOT:PSS).

Preliminary work in developing a flexible PDMS stamp coated with PEDOT:PSS for contacting a planar LED has been done. First, PDMS was prepared by mixing and degassing a PDMS prepolymer (Dow Corning Sylgard 184, with a base to cross-linker ratio of 10:1 by mass). Curing was done at room temperature for 12 hours and 65°C for 1 hour. The PEDOT:PSS solution (Clevios PH 1000) was mixed with DMSO (5% by weight) to promote conductivity. A nonionic fluorosurfactant (Capstone FS-31) was added to promote adhesion of PEDOT:PSS to PDMS. PDMS pieces (~1 mm thick) were treated with UV/O_3 for 20 min to further promote adhesion and PEDOT:PSS was spin-coated (500 rpm for 5 s, 2000 rpm for 60 s) onto UV/O_3 treated PDMS pieces. The films were placed on a hot plate for 10 min at 150°C. A copper wire was adhered to the edge of the PDMS stamp on the PEDOT:PSS side using Ag paste.

The PEDOT:PSS films were electrically characterized using I-V measurements. Ag paste contacts were placed approximately 5 mm apart on the PEDOT:PSS films. As shown in Figure 9.6(a), the concentration of the fluorosurfactant, from 0.01% to 1.0%

by volume, did not significantly affect the bulk resistance (~80 Ω). Furthermore, PEDOT:PSS films on PDMS showed significantly lower resistance (~150 Ω) than Ni/Au (5 nm/10 nm) on PDMS (~1000 Ω). This is thought to be due to the brittleness of the Ni/Au, which can cause microcracks as the PDMS flexes. Because of the stretchability of PEDOT:PSS, the resistance does not increase significantly even after bending and stretching the film. UV-vis spectroscopy was used to optically characterize the PEDOT:PSS film, which showed transmission >90% for λ = 300 – 700 nm, as shown in Figure 9.6(b). Figure 9.6(c) shows a photograph of a planar LED being electrically injected using a probe on the n-side and the final PEDOT:PSS/PDMS stamp on the p-side.

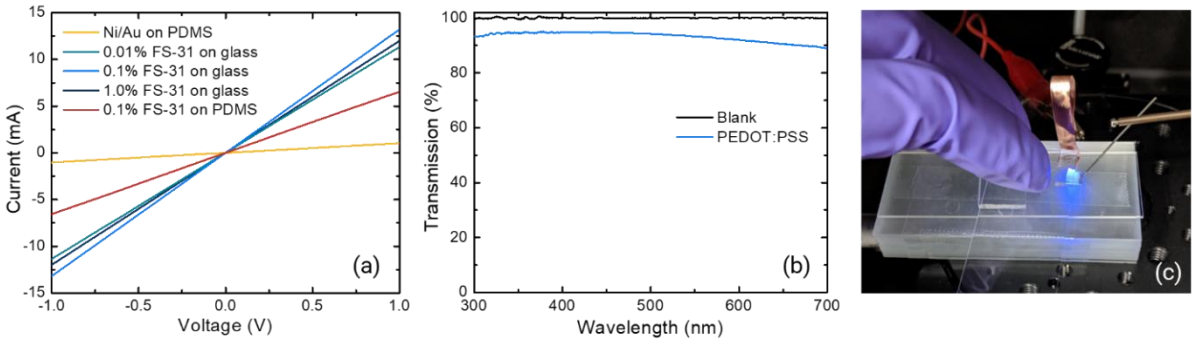

Figure 9.6: (a) I-V measurement of 5 nm/10 nm Ni/Au deposited via e-beam deposition on PDMS, 0.01%, 0.1%, and 1.0% by weight FS-31 fluorosurfactant spin-coated on glass, and 0.1% FS-31 fluorosurfactant spin-coated on PDMS. (b) Transmission measured using UV-vis spectroscopy of PEDOT:PSS spin-coated on glass. (c) Photograph of LED being electrically injected where a probe was used to contact the n-contact and PEDOT:PSS on PDMS was used to contact the p-contact.

9.4 References

1. Ahn, J.-H. *et al.* Heterogeneous three-dimensional electronics by use of printed semiconductor nanomaterials. *Science (80-.).* **314**, 1754–7 (2006).

2. Meitl, M. A. *et al.* Transfer printing by kinetic control of adhesion to an elastomeric stamp. *Nat. Mater.* **5**, 33–38 (2006).

3. Lee, S. M. *et al.* Printable nanostructured silicon solar cells for high-performance, large-area flexible photovoltaics. *ACS Nano* **8**, 10507–10516 (2014).

4. Yoon, J. *et al.* GaAs photovoltaics and optoelectronics using releasable multilayer epitaxial assemblies. *Nature* **465**, 329–333 (2010).

5. Chan, L. *et al.* Broadband antireflection and absorption enhancement of ultrathin silicon solar microcells enabled with density-graded surface nanostructures. *Appl. Phys. Lett.* **104**, 1–6 (2014).

6. Kim, H. -s. *et al.* Unusual strategies for using indium gallium nitride grown on silicon (111) for solid-state lighting. *Proc. Natl. Acad. Sci.* **108**, 10072–10077 (2011).

7. Kim, T. Il *et al.* High-efficiency, microscale GaN light-emitting diodes and their thermal properties on unusual substrates. *Small* **8**, 1643–1649 (2012).

8. Park, S. Il *et al.* Printed assemblies of inorganic light-emitting diodes for deformable and semitransparent displays. *Science (80-.).* **325**, 977–981 (2009).

9. Bachilo, S. M. *et al.* Structure-assigned optical spectra of single-walled carbon nanotubes. *Science (80-.).* **298**, 2361–2366 (2002).

10. Kang, S. J. *et al.* High-performance electronics using dense, perfectly aligned arrays of single-walled carbon nanotubes. *Nat. Nanotechnol.* **2**, 230–236 (2007).

11. Kim, D. H. *et al.* Epidermal electronics. *Science (80-.).* **333**, 838–843 (2011).

12. Eo, Y. J. *et al.* Enhanced DC-Operated Electroluminescence of Forwardly Aligned p/MQW/n InGaN Nanorod LEDs via DC Offset-AC Dielectrophoresis. *ACS Appl. Mater. Interfaces* **9**, 37912–37920 (2017).

13. Park, H. K. *et al.* Horizontally assembled green InGaN nanorod LEDs: scalable polarized surface emitting LEDs using electric-field assisted assembly. *Sci. Rep.* **6**, 28312 (2016).

14. Chow, E. M. *et al.* Xerographic MicroAssembly Printer for LEDs and Beyond. *SID*

Symp. Dig. Tech. Pap. **50**, 349–352 (2019).

15. Frentrup, M. *et al.* Determination of lattice parameters, strain state and composition in semipolar III-nitrides using high resolution X-ray diffraction. *J. Appl. Phys.* **114**, (2013).

16. Vosgueritchian, M., Lipomi, D. J. & Bao, Z. Highly conductive and transparent PEDOT:PSS films with a fluorosurfactant for stretchable and flexible transparent electrodes. *Adv. Funct. Mater.* **22**, 421–428 (2012).

17. Lipomi, D. J. *et al.* Electronic properties of transparent conductive films of PEDOT:PSS on stretchable substrates. *Chem. Mater.* **24**, 373–382 (2012).

18. Crispin, X. *et al.* The Origin of the High Conductivity of Poly(3,4-ethylenedioxythiophene)-Poly(styrenesulfonate) (PEDOT-PSS) Plastic Electrodes. *Chem. Mater.* **18**, 4354–4360 (2006).